THERMAL AND ELECTRICAL TRANSPORT STUDY OF ONE DIMENSIONAL NANOMATERIALS

A Dissertation

by

LIANG YIN

Submitted to the Office of Graduate Studies of
Texas A&M University
in partial fulfillment of the requirements for the degree of

DOCTOR OF PHILOSOPHY

Chair of Committee,	Choongho Yu
Committee Members,	Donald G. Naugle
	David Staack
	Xinghang Zhang
Head of Department,	Andreas A. Polycarpou

August 2013

Major Subject: Mechanical Engineering

Copyright 2013 Liang Yin

ABSTRACT

This dissertation presents experimental and computational study of thermal and electrical transport in one-dimensional nanostructures. Synthesizing materials into one-dimensional nanowire has been proved very effective for suppressing the phonon contribution due to scattering at the wire boundaries. Three one-dimensional nanostructured thermoelectric candidates - SiGe nanowires, $SrTiO_3$ nanowires, and ZnO nanowires – were presented and discussed in this dissertation.

SiGe nanowires are successfully synthesized on a cleaned n-type (100) Si substrate coated with gold thin film as a catalytic metal, via the vapor-liquid-solid (VLS) growth method. The thermoelectric properties of SiGe nanowires with different diameter, Ge concentration, and phosphorus doping concentration were measured using a MEMS micro-device consisting of two suspended silicon nitride membranes in the temperature range of 60 K ~450 K. The experimental results were obtained by "simultaneously" measuring thermal conductivity, electrical conductivity, and thermopower. The *ZT* improvement is attributed to remarkable thermal conductivity reductions, which are thought to derive from the effective scattering of a broad range of phonons by alloying Si with Ge as well as by limiting phonon transport within the nanowire diameters.

An improved model based on Boltzmann transport equation with relaxation time approximation was introduced for estimating thermoelectric properties of phosphorus heavily doped SiGe nanowires from 300 to 1200 K. All the electron and phonon

scatterings were comprehensively discussed and utilized to develop the new model for estimating electrical conductivity, thermopower, and thermal conductivity of SiGe nanowires.

As thermoelectric materials, oxide nanowires have great advantages comparing to other semiconductors. Two nanostructured materials, $SrTiO_3$ nanotubes and ZnO nanowires, are introduced and successfully synthesized by simple methods. Thermal conductivity of ZnO nanowires with different diameter were characterized from 60 K to 450 K.

In order to measure thermoelectric properties of one-dimensional nanostructures at temperature up to 800 K, a new temperature vacuum system was carefully designed and built from scratch. The thermal conductivity of ZnO nanowires with different diameters at high temperature were measured from 300 K to 800 K.

DEDICATION

To my parents and my wife

ACKNOWLEDGEMENTS

I would like to express my deepest appreciation to my dissertation supervisor, Professor Choongho Yu, for his encouragement, guidance and persistent support during the whole work with this dissertation. Without his inspiration and mentoring this dissertation would not have been possible.

I would also like to thank my committee members, Professor Donald G. Naugle, Professor David Staack, Professor Xinghang Zhang for their invaluable comments and guidance throughout this research.

In addition, I thank all my colleagues at the Texas A&M University, especially appreciate the help and encourage from my lab mates, Yunki Gwak, Vinay Narayanunni, Marion Okoth, Ytontack Ryu, Kyungwho Choi, Xiong Pu, Abdullah S Tazebay, Hong Wang in the Nano-Energy Lab.

I give special thanks the financial support from the US National Science Foundation (0854467), the US Air Force Office of Scientific Research (FA9550-09-1-0609), and the Pioneer Research Center Program through the National Research Foundation of Korea (2011-0001645) funded by the Ministry of Education, Science and Technology (MEST).

Finally, I would like to thank my parents for their endless love and encourage and my wife for her love, encourage and belief in me.

NOMENCLATURE

d	diameter of nanowire [m];
D_A	number density of atoms [1/m^3];
D_C	number density of clusters [1/m^3];
E	deformation potential [J];
E_g^*	reduced band gap.
F_η	Fermi integral with η index;
h	Planck constant [6.626068×10^{-34} m^{2}kg/s];
i	subscript to indicate longitudinal (L) or transverse (T);
j	subscript to indicate electron (e) or hole (h);
k	total thermal conductivity [W/m-K];
k_B	Boltzmann constant [1.3806503×10^{-23} m^{2}kg/s^2-K];
k_e	electronic thermal conductivity [W/m-K];
k_l	lattice thermal conductivity [W/m-K];
k_L	thermal conductivity from longitudinal phonons [W/m-K];
k_T	thermal conductivity from transverse phonons [W/m-K];
L	Lorenz number [2.44×10^{-8} WΩ/K^2];
m^*	effective mass of electrons [kg];
M	average mass of an atom [kg];
M_{Si}	mass of a silicone atom [kg];
M_{Ge}	mass of a germanium atom [kg];

n	carrier density [1/m^3];
N_i	ionized impurity concentrations [1/m^3];
N_n	non-ionized impurity concentrations [1/m^3];
q	electron elementary charge [1.602×10^{-19} C];
R_C	radius of cluster [m];
S	thermopower [V/K];
S_e	thermopower due to electrons [V/K];
S_h	thermopower due to holes [V/K];
T	absolute temperature [K];
v_i	acoustic phonon speed of SiGe [m/s];
V	volume per atom [m^3];
x	reduced energy of phonons;
y	Ge atomic concentration;
θ_i	Debye temperature [K];
α	phonon surface specularity parameter;
β	reduced carrier energy at the speed of sound;
χ	permittivity [A^{2}s^4/kg-m^3];
ε	reduced energy of electrons or holes;
γ_i	Grüneisen parameters;
μ^*	reduced chemical potential;
ρ	mass density [kg/m^3];
σ	total electrical conductivity [S/m];

σ_e	electrical conductivity due to electrons [S/m];
σ_h	electrical conductivity due to holes [S/m];
τ_j	combined total electron relaxation time [s];
τ_{jA}	relaxation time due to acoustic phonon scattering [s];
τ_{jI}	relaxation time due to ionized impurity scattering [s];
τ_{jN}	relaxation time due to non-ionized impurity scattering [s];
τ_p	combined total phonon relaxation time [s];
$\tau_{pB,i}$	phonon relaxation time for boundary phonon scattering [s];
$\tau_{pE,i}$	phonon relaxation time for electron phonon scattering [s];
$\tau_{pI,i}$	phonon relaxation time for impurity phonon scattering [s];
$\tau_{pN,i}$	phonon relaxation time for normal phonon scattering [s];
$\tau_{pU,i}$	phonon relaxation time for Umklapp phonon scattering [s];
ω_C	adjusted cut-off phonon frequency [Hz];
ω_D	Debye phonon frequency [Hz].

TABLE OF CONTENTS

Page

ABSTRACT ii

DEDICATION iv

ACKNOWLEDGEMENTS v

NOMENCLATURE....vi

TABLE OF CONTENTS ix

LIST OF FIGURES....xi

LIST OF TABLES xv

CHAPTER I INTRODUCTION 1

1.1 Thermoelectric effect 1
1.2 Thermoelectric figure-of-merit 4
1.3 One-dimensional nanostructures as thermoelectric materials....6
1.3.1 SiGe nanowires 9
1.3.2 $SrTiO_3$ nanowires....9
1.3.3 ZnO nanowires....10
1.4 Thermoelectric properties measurement method for single nanowire....11

CHAPTER II THERMOELECTRIC PROPERTIES MEASUREMENT OF SIGE NANOWIRES....18

2.1 Synthesis of SiGe nanowires....18
2.2 Sample preparation....20
2.2.1 Micro-device fabrication....20
2.2.2 Assemble nanowire with micro-device....21
2.3 Experimental setup....23
2.4 Error analysis 25
2.5 Thermal conductivities measurement of SiGe nanowires....26
2.6 Simultaneously measurement of thermoelectric properties of highly doped SiGe nanowires 36

CHAPTER III SIMULATION OF THERMOELECTRIC PROPERTIES OF SIGE NANOWIRES....48

3.1 Electrical conductivity and thermopower modeling 48
3.2 Thermal conductivity modeling 53
3.2.1 Phonon thermal conductivity 53
3.2.2 Electric thermal conductivity 56
3.3 Results and discussion 56

CHAPTER IV OXIDE NANOWIRES FOR THERMOELECTRIC APPLICATION ...75

4.1 Synthesis of strontium titanate ($SrTiO_3$) nanotubes 75
4.1.1 Synthesis of TiO_2 nanotubes 75
4.1.2 Strontium incorporation processes 78
4.1.3 Results and discussion 79
4.2 Synthesis of zinc oxide (ZnO) nanowires 84
4.2.1 Synthesis method 84
4.2.2 Properties characterization 88
4.2.3 Results and discussion 92
4.3 Thermal conductivity investigation of ZnO nanowire at low temperature range 98
4.3.1 Sample preparation 98
4.3.2 Results and discussion 99

CHAPTER V THERMAL CONDUCTIVITY INVESTIGATION OF NANOWIRE AT HIGH TEMPERATURE RANGE 102

5.1 High temperature setup development 102
5.1.1 Parameters design 102
5.1.2 Temperature controlled by PID algorithm 109
5.2 Sample preparation 111
5.3 Thermal conductivity measurement of ZnO nanowires at high temperatures ..112

CHAPTER VI CONCLUSION 115

REFERENCES 119

LIST OF FIGURES

Page

Figure 1. The Seebeck effect of typical metals. (a) Temperature gradient between two sided of metal; (b) voltage difference generated due to the diffused electrons. 2

Figure 2. Schematic diagram of a thermoelectric device. (a) Temperature difference generated a voltage based on Seebeck effect. (b)Passing current through the device can generated temperature gradient by Peltier effect. 4

Figure 3. Thermal conductivity of silicon nanowires synthesized by vapor-liquid-solid method (black squares) and electroless etching (red squares). 7

Figure 4. A schematic diagram (a) and SEM image (b) of a micro-device for thermoelectric properties measurements of nanowire. 12

Figure 5. A schematic diagram of thermoelectric properties measurements. 13

Figure 6. Temperature distribution of two membranes on the micro-device by the finite element analysis. 15

Figure 7. A typical SEM image of SiGe nanowire synthesized by VLS method. 19

Figure 8. A TEM (a) and a high-resolution TEM (b) of a $Si_{0.9}Ge_{0.1}$ nanowire grown via the VLS method and a selected area electron diffraction pattern in the inset. The growth direction of the nanowire is [111].. 20

Figure 9. A nanowire is bridged between two suspended membranes. The contacts were improved by using various methods including Ni or Pt depositions as shown in the inset. 22

Figure 10. (a) Micro-device inserted in a 24 pin dual in line package (DIP). Electrical connection between micro-device and DIP was made through aluminum wires. (b) Packaged micro-device loaded into the cryostat. 23

Figure 11. Schematic diagram of the experimental setup for the thermoelectric properties measurement of nanowires. 24

Figure 12. TEM images of Sample 1 (a), 2 (b), 3 (c), 4 (d), 5 (e), 6 (f), and 7 (g) listed in Table 1. The scale bars indicate 20 nm. 28

Figure 13. (a, c) High angle annular dark field (HAADF) STEM images. Energy dispersive spectroscopy (EDS) results for the impurity dot (b) and SiGe nanowire (d). 29

Figure 14. Thermal conductivities of Sample 1-7 and $Si_{0.91}Ge_{0.09}$ with 160 nm in diameter, plotted together with minimum thermal conductivities of $Si_{0.63}Ge_{0.37}$ and $Si_{0.37}Ge_{0.63}$. 32

Figure 15. The thermal conductivities of the SiGe nanowires. The thermal conductivities of the SiGe nanowires listed in Table 2 are plotted with those of the previously reported samples including a 56-nm diameter Si nanowire,[11] a $Si_{0.9}Ge_{0.1}$ bulk,[49] a $Si_{0.6}Ge_{0.4}$ bulk,[49] a $Si_{0.91}Ge_{0.09}$ nanowire,[56] and the calculated summation of electronic (k_e) and minimum ($k_{\min}$) thermal conductivities for the $Si_{0.74}Ge_{0.26}$ nanowire. The inset shows the thermal conductivities at 300 K of the SiGe nanowires that were measured in our study. 39

Figure 16. Simultaneously measured (60-450 K) and theoretically calculated (250-800 K) electrical conductivity, thermopower, and the figure-of-merit (ZT) of the SiGe nanowires. (a) Electrical conductivity, (b) thermopower, and (c) ZT values are plotted for $Si_{0.92}Ge_{0.08}$, $Si_{0.90}Ge_{0.10}$, $Si_{0.74}Ge_{0.26}$, and $Si_{0.73}Ge_{0.27}$ with those of a bulk SiGe RTG[14] as reference values. Calculated results were obtained with two different carrier densities, 9.0×10^{19} (blue-solid line) and 3.3×10^{20} cm^{-3} (red-broken line) for $Si_{0.73}Ge_{0.27}$. 44

Figure 17. Simulated electrical properties of heavily doped SiGe nanowire without considering non-ionized doped phosphorus. 58

Figure 18. A schematic diagram of two materials with just ionized impurities (a) and both ionized and non-ionized impurities (b). 59

Figure 19. Simulated electrical properties of heavily doped SiGe nanowire with considering non-ionized doped phosphorus. 62

Figure 20. Simulation results of thermal conductivities of SiGe nanowires with different Ge concentration along with two SiGe bulk materials in reference.[49] 66

Figure 21. Large improvement of ZT values of SiGe nanowires by removing non-ionized impurities scattering. 71

Figure 22. The calculated ZT value of $Si_{0.73}Ge_{0.27}$ nanowire after removing non-ionized impurity as function of ionized donor density. The two points represent the experimental data of $Si_{0.73}Ge_{0.27}$ nanowire with non-ionized phosphorus density of 3.2×10^{20} cm^{-3}. 73

Figure 23. (a) A cross section of a typical titanium oxide nanotube array by anodizing a titanium foil. Titanium oxide tubes were made from the outer surface to the center, creating a barrier layer that makes one of the tube ends closed. (b) An outer surface of the anodized foil shows circular pores from the tube array. Gentle sonication separated the array into (c) a bundle and (d) an individual titanium oxide nanotube. The electron diffraction in the inset shows amorphous structure...77

Figure 24. Typical XRD scans of nanotube arrays after a strontium incorporation process with 0.1 M $Sr(OH)_2$ at (a) 90 ^oC and (b) 180 ^oC for 2 hours without a fluorine desorbing process. Fluorine residues on the surface of titanium oxides from the anodization and etching processes are easily crystallized into SrF_2. Peaks indicated by * are from $SrTiO_3$. 79

Figure 25. Typical XRD scans of the tube array after a strontium incorporation process with 0.2 M $Sr(OH)_2$ at (a) 90 ^oC and (b) 180 ^oC for 4 hours. Crystallographic directions indicate the presence of crystalline $SrTiO_3$. 80

Figure 26. (a) A strontium titanate tube array synthesized with 0.1 M $Sr(OH)_2$ at 180 ^oC for 12 hours. (b) An individual strontium titanate nanostructure synthesized with 0.1 M $Sr(OH)_2$ at 90 ^oC for 4 hours. (c) A high resolution image of a portion (marked with a square in (b)) indicates crystalline strontium titanates with the axis in [100] direction. (d) An electron diffraction image corresponding to the image in (c). 81

Figure 27. Typical XRD scans of Samples after annealing in an oxygen flow (~20 sccm) at 450 ^oC for 2 hours. Peaks indicated by * are from $SrTiO_3$. 83

Figure 28. Zn foils with $ZnCl_2$ coating after thermal annealing at 410 ^oC for 120 min (a), 700 ^oC for 60 min (b), 850 ^oC for 30 min (c), 700 ^oC for 10 min (f), and 700 ^oC for 30 min (g). Zn foils without $ZnCl_2$ after thermal annealing at 410 ^oC for 120 min (d) and 700 ^oC for 60 min (e). (h) A typical XRD pattern from the sample synthesized by thermal annealing at 700 ^oC for 60 min (synthesis condition 3 in Table 6)..89

Figure 29. (a) A ZnO nanowire synthesized by thermal annealing at 700 ^oC for 60 min (synthesis condition 3 in Table 6). (b) A high resolution TEM image that shows lattice patterns with a SAED in the inset. 91

Figure 30. ZnO nanostructures on a Si wafer coated with $ZnCl_2$ after thermal annealing at 500 ^oC for 5 min (a) near the center with low density ZnO and (b) near the edge with high density ZnO. (c) Unreacted $ZnCl_2$ particles showing a tetragonal structure. (d) A typical XRD pattern of $ZnCl_2$ on a quartz wafer after thermal annealing at 500 ^oC for 5 min. 93

Figure 31. ZnO nanostructures from Zn powders after thermal annealing at (a) 850 ^oC, (b) 800 ^oC, (c) 700 ^oC, and (d) 500 ^oC for 30 min. 95

Figure 32. A typical SEM image of ZnO nanowire bridged on platinum electrodes of micro-device; the inset is a high magnification image of the bridged nanowire. 99

Figure 33. The thermal conductivity of ZnO nanowires with different diameters. The experimentally results are plotted together with previously reported ZnO nanostructured bulk and also ZnO bulk. 101

Figure 34. Two major vacuum chambers were connected together after necessary modification. 104

Figure 35. The original design drawing and final product of the cold finger. 105

Figure 36. The final assembled high temperature thermal vacuum setup for thermoelectric properties measurement of nanostructured materials. 108

Figure 37. The stability of temperature near the micro-device controlled by PID algorithm at 450 K, 600 K, 700 K and 800 K. 110

Figure 38. The thermal conductivity of ZnO nanowires with different diameter from 60 K to 800 K. The thermal conductivity data were obtained from two different thermal vacuum system with the temperature range of 60 K ~ 450 K, and 300 K ~ 800 K, respectively. 113

LIST OF TABLES

Page

Table 1. Si/Ge ratio (total and core), diameter (total and core), length, oxide layer thickness of SiGe nanowires as well as thermal contact enhancement method for measuring thermal conductivity. 27

Table 2. Parameters of simultaneously measured SiGe nanowires. 38

Table 3. Si/Ge ration, doping condition, diameter, ionized and non-ionized impurity concentration of SiGe nanowires. 60

Table 4. Parameters for the simulation of thermoelectric properties of SiGe nanowires. 69

Table 5. Five different $SrTiO_3$ synthesis conditions to verify strontium incorporation into titanium oxides. 82

Table 6. Twelve different synthesis conditions to obtain ZnO nanostructures with Zn foils or Zn powders. $ZnCl_2$ was dissolved in water and spin-coated on the selected foils. 87

Table 7. The parameters of P, I, and D for temperature controller Lakershore 336 from 300 K to 800 K. 111

CHAPTER I

INTRODUCTION

This dissertation consists of experimental and computational investigations of thermoelectric transport behaviors in one-dimensional nanostructures from low temperature to high temperature range. This chapter describes the background and motivation of these researches.

1.1 Thermoelectric effect

The thermoelectric effect, also called Peltier – Seebeck effect, is the phenomenon described the direct conversion between the temperature gradient and the built-in electric field in a conductor or a semiconductor. A thermoelectric device is an application of thermoelectric effect which produces voltage difference between two sides when a temperature gradient is imposed. Conversely instead of generating voltage by external temperature source, passing a current through the thermoelectric device may be used to create a temperature difference.

The Seebeck effect was first discovered by Baltic German physicist Thomas Johann Seebeck in the early 1820's. It was found that a compass magnet would be deflected by a circuit formed by two dissimilar metals, with its junctions placed at different temperature. The magnetic field created by the current loop inside of the circuit was the reason of the deflection. A schematic diagram of the Seebeck effect is shown in Figure 1. A metal rod is heated at one side and cooled at the other end as depicted in

Figure 1a. The charge carriers (electrons) in the hot side are more energetic and slightly higher velocities than those in the cold side. Consequently, electrons start to diffuse from the hot side to the cold side, which exposes the positive ions on the hot side and accumulates the negative electrons on the cold side. Therefore, a voltage difference ΔV is developed between the hot and cold sides as shown in Figure 1b. The Seebeck effect is extensively used in the thermocouple for monitoring the temperature, which uses two different metals with one junction as the reference temperature and the other used to detect the temperature.

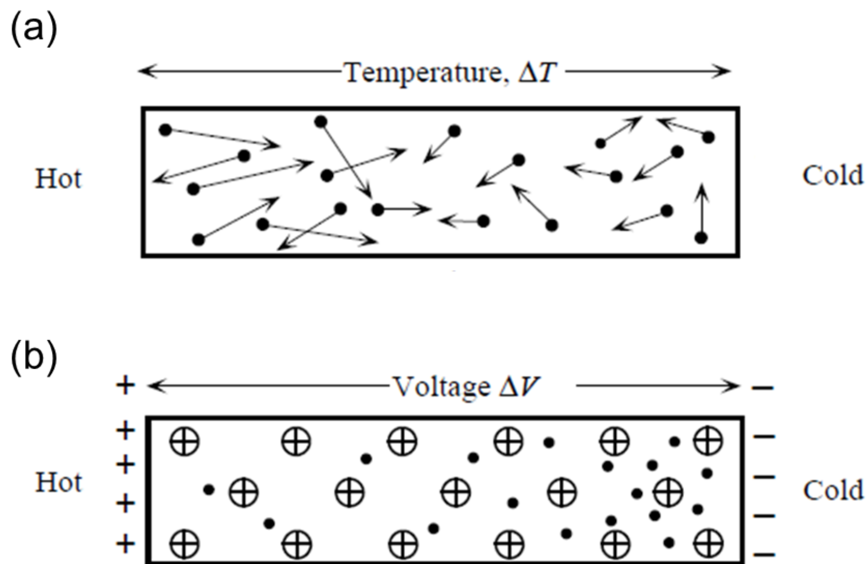

Figure 1. The Seebeck effect of typical metals. (a) Temperature gradient between two sided of metal; (b) voltage difference generated due to the diffused electrons.

The Peltier effect was discovered by French physicist Jean Charles Athanase Peltier in 1834. It creates temperature difference by forcing electron current through a

junction of two different metals. Heating side and cooling side can be exchanged by switching the direction of current. The Peltier effect can be utilized for solid state refrigerator as a replacement of traditional compressed-based cooler. No-moving parts in Peltier cooler are the major benefit of Peltier cooler due to silence and robustness. Peltier cooler is also very effective for electronics cooling with compact form factors.

Thermoelectric devices can utilize Seebeck effect to generate electrical voltage through an external source of heat and also produce temperature difference by Peltier effect. A schematic diagram of typical thermoelectric device is shown in Figure 2. The thermoelectric device consists of two types of semiconductors, one of which is called “n-type” and contains negatively charged carriers – electrons, while the other one is called “p-type” which contains positively charged carriers – holes. These two types’ materials are electrically connected in series. Due to the Seebeck effect, positive charge will build up on the cold side of the p-type material when an external temperature gradient is presented. Similarly, negative charge will produce a negative potential on the cold side of the n-type material. While an electric load is connected to the thermoelectric device across both cold sides, the voltage generated by Seebeck effect will create current to flow through the electric load, as shown in Figure 2a. Instead of electric load, if we connect an external electric potential, both electrons and holes will flow away from the top of the device towards the bottom. During the process the electric carriers will drive the heat from cold side and deposit it on the hot side. As the current flows, the top side of the thermoelectric device will be cooled down, as shown in Figure 2b.

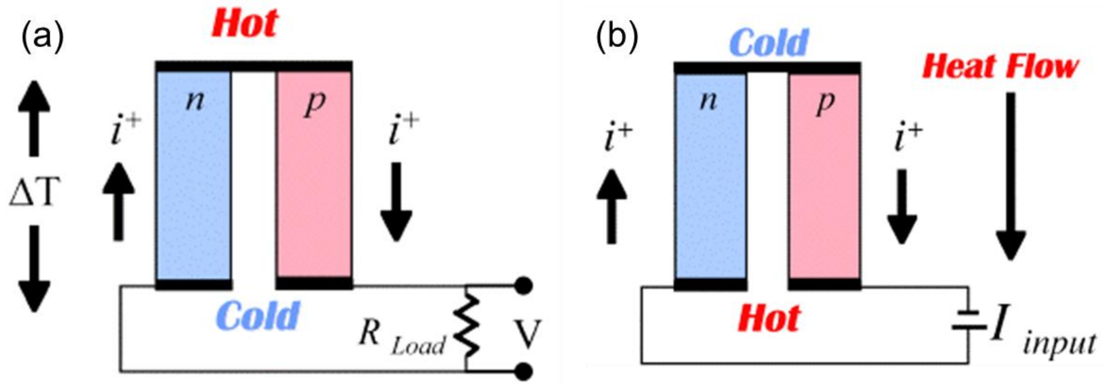

Figure 2. Schematic diagram of a thermoelectric device. (a) Temperature difference generated a voltage based on Seebeck effect. (b)Passing current through the device can generate temperature gradient by Peltier effect.

1.2 Thermoelectric figure-of-merit

The efficiencies of thermoelectric devices are typically described by the dimensionless thermoelectric figure-of-merit (*ZT*), which can be defined as

$$ZT = \frac{S^2 \sigma T}{k_{electron} + k_{phonon}} \tag{1}$$

where, *S* is the thermopower (or the Seebeck coefficient), σ is the electrical conductivity, $k_{electron}$ is the electronic thermal conductivity, k_{phonon} is the lattice thermal conductivity, and *T* is the absolute temperature. In order to achieve the optimum thermoelectric device performance, the thermoelectric material should have high Seebeck coefficient and electrical conductivity, and also must be poor conductor of heat. However, all these thermoelectric properties (*S*, σ, $k_{electron}$, and k_{phonon}) are strongly correlated, which makes the improvement of *ZT* very difficult. For example, an increase of electrical conductivity in bulk materials often decreases the Seebeck coefficient and increases thermal conductivity. It has also been proven difficult to reduce thermal conductivity when

electrical properties are improved or maintained, since the electronic thermal conductivity ($k_{electron}$) is directly connected to electrical conductivity (σ) by Wiedemann-Franz law

$$k_e = \sigma LT \tag{2}$$

where, $L = 2.44 \times 10^{-8}\ \mathrm{W\Omega K^{-2}}$ is the Lorenz number. The best thermoelectric materials at room temperature are the alloys of bismuth telluride and antimony telluride, which were found to have ZT values around unit at the end of 1950s.[1-3] Over the past half century, the upper limit of ZT has been improved very little. In order to be competitive with or comparable to conventional vapor compression refrigerator and power generator, the ZT value of thermoelectric material must be improved to a value larger than 3.[4] Significant research efforts have been attracted to improve their efficiencies. Nevertheless, until now there is still no candidate bulk material can reach this level.

Recent research reports suggest that ZT may be improved by suppressing phonon transport (reducing k_{phonon}) without considerably altering other properties[5-7]. Base on the kinetic theory, the lattice thermal conductivity is expressed as

$$k_{phonon} = \frac{1}{3} C v l \tag{3}$$

where, C is the volumetric heat capacity, v is the group velocity of phonons and l is the mean free path of phonons. While the change of heat capacity and velocity of phonons at high temperature is small, the lattice thermal conductivity can be dramatically reduced by suppressing the phonon mean free path. Since the phonon characteristic lengths in crystalline solids are often much longer than those of electrons, it is possible to confine

phonons rather than electrons, selectively. Particularly in semiconductor materials, the lattice thermal conductivity is dominant due to their smaller electrical conductivity compared to metals, and could be effectively suppressed by reducing phonon's mean free paths. If nanostructured substitutions or gain boundaries are embedded in crystalline, the phonon transport will be limited due to the boundary scattering. The phonon can also be suppressed by lattice imperfections such as alloy atoms and defects. For example, The ZT value of commercially available bulk $(Bi, Sb)_2Te_3$ alloys has been improved from ~1 to ~1.4 by embedding nanostructures in the bulk.[8, 9] When $In_{0.53}Ga_{0.47}As$ contains ErAs nanoparticles, its thermal conductivity was reduced by a factor of 2 lower than the alloy limit.[10]

1.3 One-dimensional nanostructures as thermoelectric materials

The strongly-correlated thermoelectric properties have been a major problem for obtaining high-performance thermoelectric energy conversion. In order to avoid such correlation, one possible approach is suppressing phonon transport by confined nanowire structures. Synthesizing materials into one-dimensional nanowire structures has proved very effective for reducing the lattice thermal conductivity due to scattering phonons at the wire boundaries. For example, comparing with the thermal conductivities of a bulk crystalline Si, the thermal conductivity of Si nanowires has been significantly decreased.[11, 12] Strong diameter dependence of thermal conductivity was reported due to the phonon scattering at the wire boundaries. Figure 3 shows the experiment results of thermal conductivity of silicon nanowires synthesized by two different methods with

different diameters. It has been clearly shown that the thermal conductivity of silicon nanowires is strongly diameter dependent. As the diameter of nanowires decreases, the thermal conductivity of nanowires also decreases. It should be noticed that all the thermal conductivities of silicon nanowires are a least two times smaller than the thermal conductivity of silicon bulk (~140 W/m-K at 300 K). Due to the rough surface and crystalline imperfection, the thermal conductivities of silicon nanowires synthesized by the electroless etching method are smaller than that synthesized by the vapor-liquid-solid method

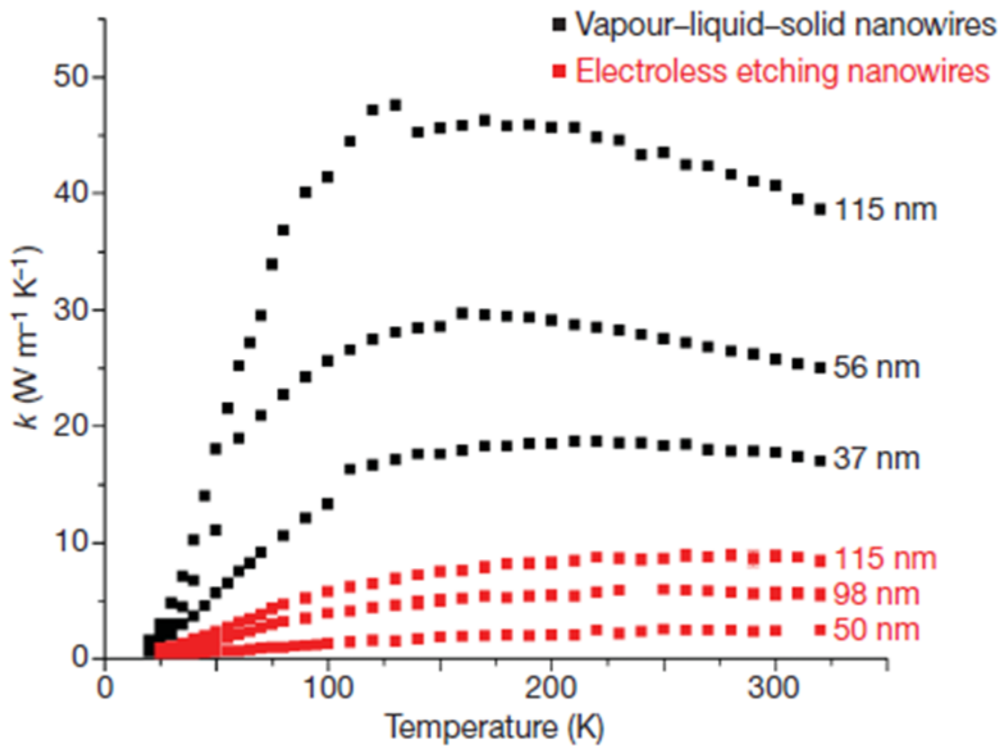

Figure 3. Thermal conductivity of silicon nanowires synthesized by vapor-liquid-solid method (black squares) and electroless etching (red squares).[12]

The small thermal conductivity of one-dimensional silicon nanowires are attributed to the boundary scattering of phonons. Nevertheless, in order to fully suppress phonon heat transport of crystalline solids, synthesizing into nanowires may be in sufficient since the phonon characteristic lengths are broad. The phonons with characteristic lengths (wavelength or mean free path) smaller than the nanowire diameters are most likely to be not affected. In order to scatter these short-length phonons, the diameter of nanowire to a few nanometers or less is required. Since it is impractical to synthesize such small diameter nanowire, these phonons should be scattered by defects or impurities whose sizes are much smaller than the diameters. Synthesizing materials into alloy can contribute to further reduce the thermal conductivity by impurity-phonon scattering.

Although synthesizing into one-dimensional structures could significantly reduce the thermal conductivity and have very promising potential to improve the thermoelectric efficiency, not enough research has been carried out on nanowire structures other than Si nanowires. One reason is because of the difficulty synthesize thermoelectric materials into nanostructures. Moreover, special measurement instruments and technology are also required in order to measure the properties of nanostructures. In this dissertation, three one-dimensional nanostructured thermoelectric candidates - SiGe nanowires, $SrTiO_3$ nanowires, and ZnO nanowires – were produced and studied.

1.3.1 SiGe nanowires

While current commercial thermoelectric alloys contain toxic and expensive elements such as Te and Pb, SiGe alloys could be another non-toxic and low-cost substitute. In particular, SiGe alloys have been used for the radioisotope thermoelectric generator (RTG) in NASA space flights[13, 14]due to their relatively high thermoelectric efficiency (*ZT* = 0.5~0.95) at high temperatures 1073-1173 K. Thermoelectric properties of SiGe have been investigated in various forms including thin films[15], amorphous structures[16], hot-pressed pellets.[17] Recently, n-type SiGe nanostructured bulk samples have been reported with an improved *ZT* of ~1.3 at 900 ^{o}C[14], and p-type SiGe bulk samples with *ZT* ~ 0.95 at 800 ^{o}C.[13] These materials contain nanoscale grain boundaries that scatter phonons and thereby suppress thermal conductivity. When one-dimensional nanostructures are employed, it is expected to further reduce thermal conductivity due to the confined structure (i.e., physical barrier at the nanowire boundary) that may selectively scatters phonons rather than electrons. Further reduction in thermal conductivity can be achieved by alloying Ge with Si, due to additional scattering for phonons whose wavelengths or mean free paths are smaller than wire diameters.

1.3.2 $SrTiO_3$ nanowires

Another promising candidate for high thermoelectric energy conversion efficiency material is strontium titanate. Significant subsequent research effort and debate have been attracted by recent reports regarding extraordinary electrical and thermal transport properties of strontium titanates related to the origin of such extraordinary behaviors.[18-28] For example, the Seebeck coefficient could be increased

without considerably decreasing electrical conductivity by confining electron transport within nano-scale layers.[21] High electron mobility was observed from confined interfaces[22] and thermal conductivity was reduced by introducing nanostructured oxygen vacancies.[29] Various transport related researches have been stimulated by these exciting properties of strontium titanates in addition with wide tunability in electrical and thermal transport properties.[18, 19] Synthesizing strontium titanate into one dimensional nanostructures has a high potential for improving thermoelectric performance, since phonons are often scattered at the boundary of nanowires / nanotubes when the phonons whose characteristic lengths (mean free path and wavelength) are longer than the diameter of nanowires / nanotubes. This often resulted in a large suppression in thermal conductivity and enhanced thermoelectric efficiency.

1.3.3 ZnO nanowires

In the last decade, nanostructured ZnO materials have attracted intensive research due to their great potential for a wide range of electrical and piezoelectric applications. It is a visible light transparent semiconductor which can be made electrically conductive by doping Mn, Al, Ti, Cd, Se, Ga, and N.[30-32] Al doped ZnO seems to be the most promising material for thermoelectric applications. It has been reported with the lowest electrical conductivity (10^{-6} Ωm), which is just one magnitude higher than iron metal (10^{-7} Ωm). The conductivity of Al doped ZnO is believed to change with the concentration of Al. It should be noted that as the Al doping increased the carrier concentration in AZO at first increased rapidly and then abruptly reduced at an Al doping over 11 at %. The mobility of AZO continuously decreased while Al doping

increased from 1.5 to 24.6 at %. It is believed the highest conductivity (lowest resistivity) of AZO occurs when the Al concentration is in the range of 1~3 at%. With a large Seebeck coefficient, the thermoelectric efficiency of ZnO is limited by its high thermal conductivity (~40 W/m.K). Recently Al doped ZnO nanocomposites[33] have shown an enhanced thermoelectric figure of merit ZT ≈ 0.44 at 1000 K as a result of up to a factor of 20 lower thermal conductivity deduction from non-nanostructured ZnO, while retaining bulk like thermopower and electrical conductivity. Hence an even further reduction in thermal conductivity and thus a higher thermoelectric efficiency, due to stronger phonon scattering from size effect and dopant impurities can be expected, when one-dimensional nanostructures are employed with dopants.

1.4 Thermoelectric properties measurement method for single nanowire

Currently nanoscale materials, especially one-dimensional nanomaterials, are being actively studied for thermoelectric application. For instance, the three common one-dimensional (1D) nanostructures (carbon nanotubes[10, 34-36], silicon / silicon germanium alloy nanowires[11, 37, 38], and ZnO nanowire/nanobelts[30, 31]) have been widely studied over the past few years. However, because of the small size of nanowires (diameter smaller than 1 μm), special measurement instruments and technology are required in order to measure the physical properties of single nanowire / nanotube. Particularly for measurement of thermal conductivity, a challenge is the temperature sensing in a micro-scale range. Recently the thermal conductivity of two dimensional nanostructures such as thin films and supper-lattice films has been measured by the 3

omega method.[39, 40] Nevertheless, for nanowire thermal conductivity measurement, the 3 omega method is not valid for a high resistance specimen or for large length-to-diameter-ratio nanowires because the 3 omega voltage is too small to measure with these specimens. One possible solution to these drawbacks is the use of micro-electro-mechanical system (MEMS) sensors. Due to their small size, MEMS devices can handle one-dimensional nanomaterials effectively, and can be batch fabricated in an inexpensive process.

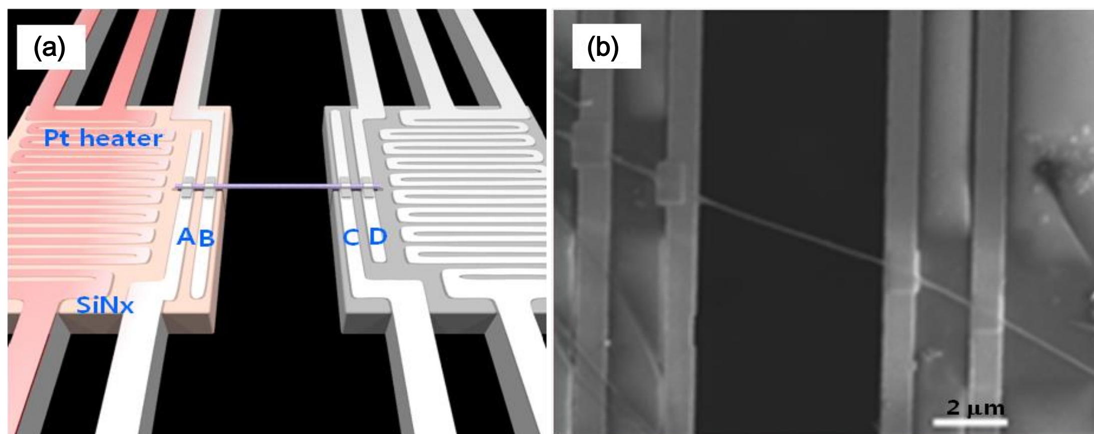

Figure 4. A schematic diagram (a) and SEM image (b) of a micro-device for thermoelectric properties measurements of nanowire.

Figure 4 shows a schematic diagram and a scanning electron micrograph (SEM) of the micro-device used in this project for the thermoelectric properties measurements of nanostructures. The device is a suspended two adjacent low stress silicon nitride (SiN_x) membranes supported by six silicon nitride beams. One platinum resistance thermometer (PRT) coil is designed and patterned on each membrane. Platinum is very

stable and has a linear resistance-temperature relationship over a large temperature range. Through the Pt leads on the long SiN_x beams, the PRT is connected to Pt pads on the Si substrate, allowing four-probe resistance measurements. Two additional Pt electrodes are designed on each membrane (A, B, C, and D lines in Figure 4a) close to each other, providing electrical and thermal contact to the nanowire samples. In order to improve the thermal and electrical contact, platinum or another metal is typically deposited on top of the nanowire sample at the Pt elelctrodes with a focused ion beam (FIB).

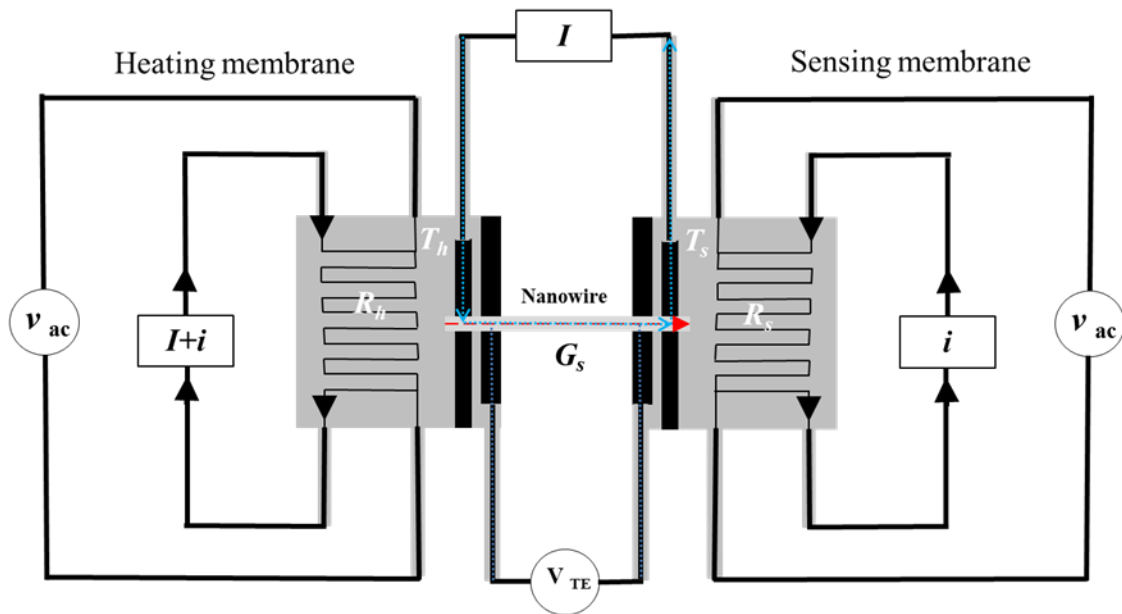

Figure 5. A schematic diagram of thermoelectric properties measurements.

The mechanism of measuring the thermal conductance of nanowire using this micro-device is shown in Figure 5. The two suspended membranes are considered as the

heating membrane and sensing membrane, respectively. AC currents (i) with different frequency are applied to the Pt resistance coils in both membranes and the temperature of membranes can be determined by measure the voltage difference (V_{ac}) between two sides of PRT coils.

$$T_m = \frac{\frac{V_{ac}}{i} - R_0}{R'} + T_0 \tag{4}$$

where, T_m is the absolute temperature on the membrane, subscript m stands for either heating membrane (m=h) or sensing membrane (m=s), R_0 is the resistance of PRT coil at temperature T_0, $R' = dR/dT$ is the ratio of resistance change and temperature change at temperature T_0.

A DC current (I) is also applied to the heating membrane and coupled with the AC current to give the total current ($I + i$). Joule heat is generated in this heating side and increases the temperature of the heating membrane. A certain amount of the joule heat is conducted from the heating side to sensing side through the nanowire, raising the temperature of sensing side to T_s. It was assumed that the temperature of each membrane is uniform on the whole membrane. This assumption can be approved by the fact that the thermal resistance of the long narrow SiN_x beams is much higher than the internal thermal resistance of the small membrane at the temperature of the environment. The finite element analysis results of the temperature on micro-device with a bridged nanowire carried out by A. Moore and L. Shi, also support this assumption as shown in the Figure 6. The temperature on each membrane is nearly isothermal, making it

reasonable to consider the temperature of membrane as the temperature of the nanowire end.

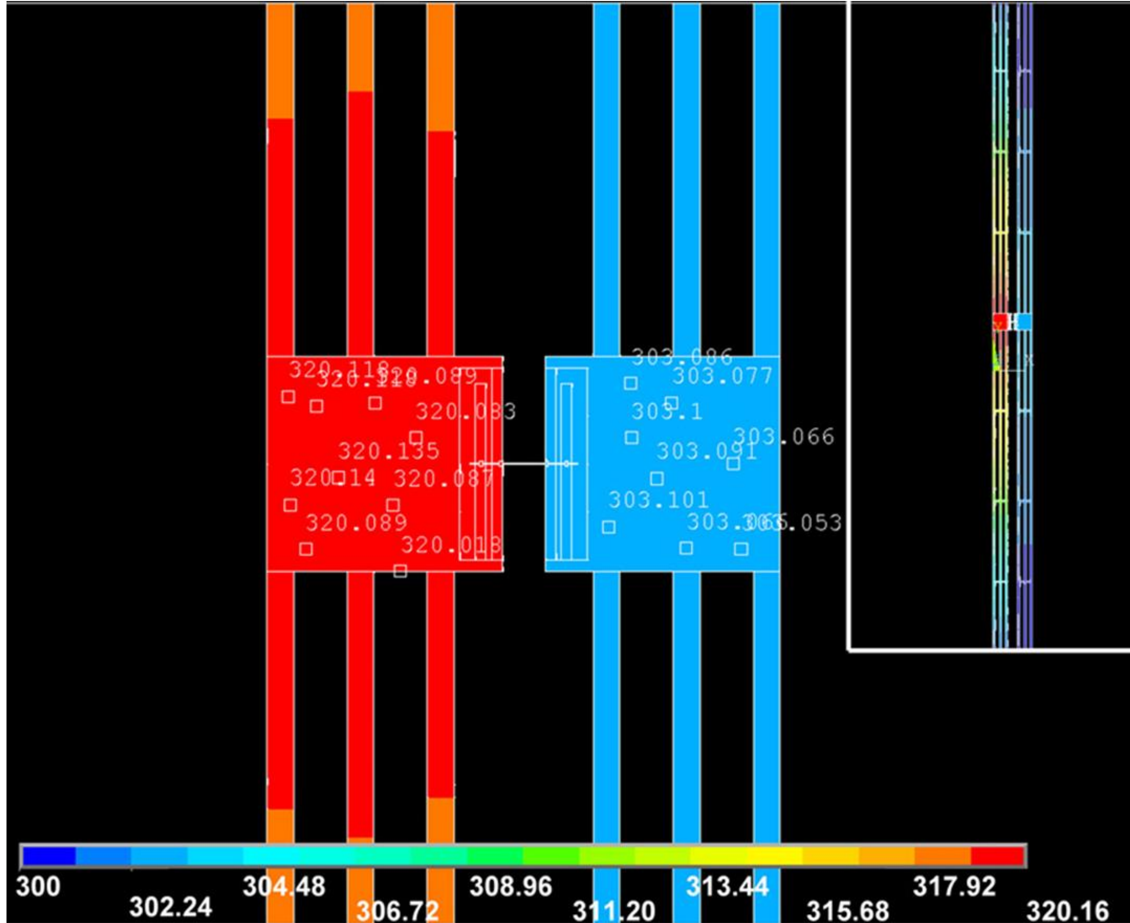

Figure 6. Temperature distribution of two membranes on the micro-device by the finite element analysis.

Moreover, because all the micro-device will be placed in vacuum and because there is only a small temperature difference between the heating and sensing sides, the heat transfer between the two membranes by radiation and air convection is negligible compared to heat conducted through the nanowire. So the thermal conductance of nanowire could be calculated by

$$G = \frac{I^2 (R_h + R_l) T_s}{(\Delta T_h + \Delta T_S)(\Delta T_h - \Delta T_s)} \quad (5)$$

where, G is the thermal conductance of specimen, which consist of the thermal conductance of the nanowire and the contacts between the nanowire and the membranes, I is the DC current passing through the heating membrane, R_h is the resistance of PRT coil on heating membrane, R_l is the resistance of each Pt leads on the SiN_x legs, T_s is the temperature on the sensing membrane, ΔT_h is the temperature change on the heating membrane, ΔT_s is the temperature change on the sensing membrane. Then, the thermal conductivity of the nanowire can be expressed as

$$k = \frac{4GL}{\pi d^2} \quad (6)$$

where, k is the total thermal conductivity of the nanowire, L is the length of the nanowire between two membranes, d is the diameter of the nanowire.

Electrical conductivity could be measured by standard four probes contacts resistance measurement method. The focused ion beam provides good electrical contacts on top of the nanowires, which are bridged on the four Pt legs. Voltage (V) between inner two contacts of nanowire could be recorded while a DC current (I) is flowing through outer two contacts of nanowires. The resistance of nanowire between inner two contacts could be calculated by applying equation $R = V/I$. When temperature gradient is established between two membranes, the thermopower voltage could be recorded with voltage (V_{TE}) between inner two contacts. Then the Seebeck coefficient could be calculated with the thermopower voltage and the temperature difference (ΔT) by the equation

$$S = \frac{V_{TE}}{\Delta T} \quad (7)$$

Finally, the thermoelectric figure-of-merit *ZT* value of the nanowire can be calculated by Eq. (1). If both electrical and thermal contact resistances between nanowire and membranes leads are small, it is possible to measure all three major thermoelectric properties (Seebeck coefficient, electrical conductivity, thermal conductivity) of one single nanowire. The simultaneous measurement is very important for properly addressing the influence on thermoelectric transport behaviors by various parameters including diameters, impurities, and defects.

CHAPTER II

THERMOELECTRIC PROPERTIES MEASUREMENT OF SIGE NANOWIRES

Silicon germanium alloy is one of the most important thermoelectric materials due to its high thermoelectric efficiency at high temperature. It has been fruitfully used as spacecraft and space station applications as the radioisotope thermoelectric generator (RTG). The thermal conductivity of bulk Silicon-Germanium alloy was much smaller than the pure Germanium and the pure Silicon.

In this chapter, SiGe are successfully synthesized into nanowire structure by VLS growth method. Three major thermoelectric properties were simultaneously measured on the same nanowires from 60K to 450K. The thermal conductivity was observed to be around 1.4 W/m-K at 300K, which can be competitive in efficiency compared to those of bulk silicon germanium alloys.

2.1 Synthesis of SiGe nanowires

SiGe nanowires were fabricated on a cleaned n-type (100) Si substrate coated with a 7-nm thick gold thin film as a catalytic metal, via the vapor-liquid-solid (VLS) growth method.[8] After the substrate (1×1 cm^2) was placed in a quartz tube reactor, the substrate was heated up to 400 ^oC. A mixture of H_2-diluted 10 % SiH_4 gas, He-diluted 10 % GeH_4 gas, and H_2-dilution PH_3 gas, as Si, Ge, and n-type dopant source, respectively, was flowed into a tube reactor for 30 min at 10 Torr. Upon heating the substrate, the gold film can be alloyed with Si, forming Au-Si nano-agglomerates that are served as

metallic catalysts for the VLS growth. As SiH_4 and GeH_4 partial pressure is changed, Ge composition of $Si_{1-x}Ge_x$ nanowires can be changed from x~0 to 0.95. Figure 7 shows SEM image of SiGe nanowire synthesized by VLS method. The as-synthesized SiGe nanowires are dense with typical length over ~15 μm.

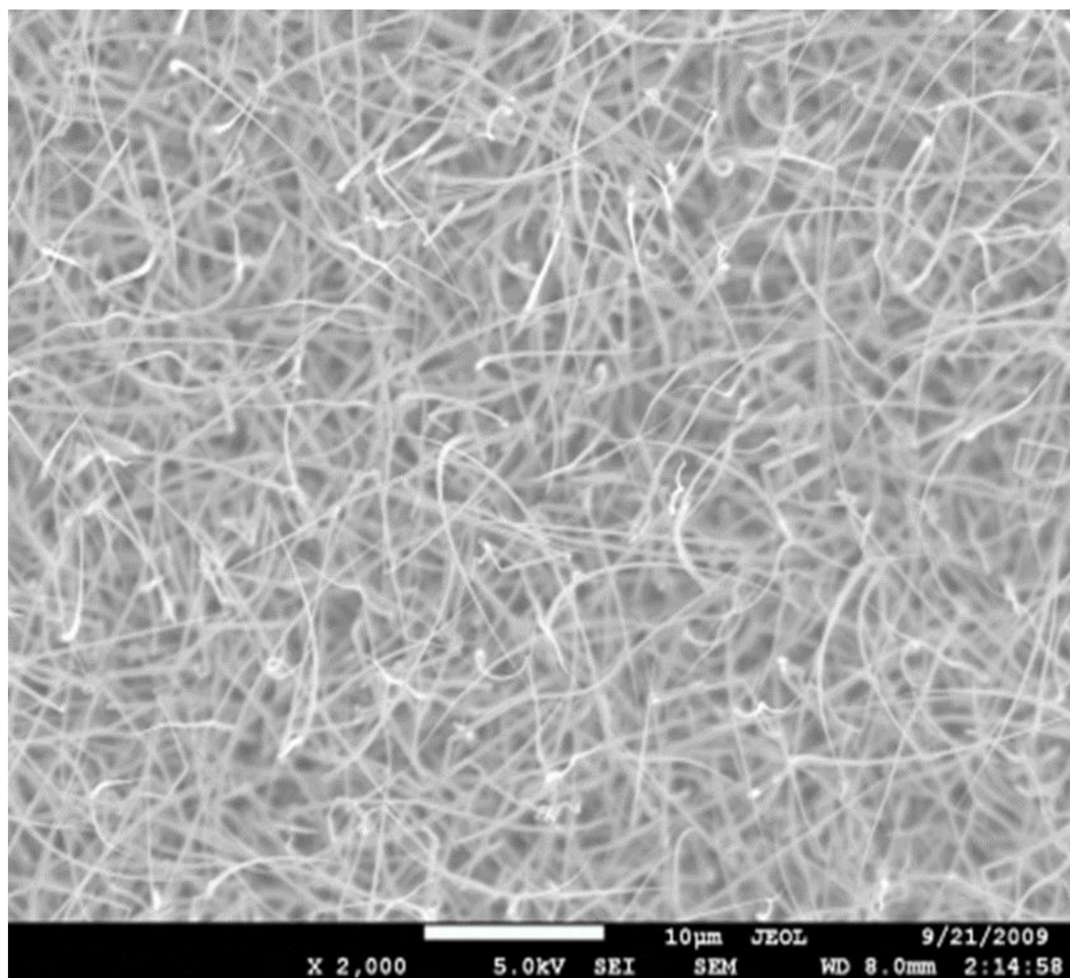

Figure 7. A typical SEM image of SiGe nanowire synthesized by VLS method.

The microstructures of the nanowires in Figure 8 were characterized by FE-Tecnai G2 F20 ST high resolution transmission electron microscope (HR-TEM) equipped with an energy dispersive spectroscopy (EDS) and selective area electron diffraction (SAED). High resolution TEM image and diffraction indicate the synthesized SiGe nanowire is perfect single crystalline and growth direction is [111].

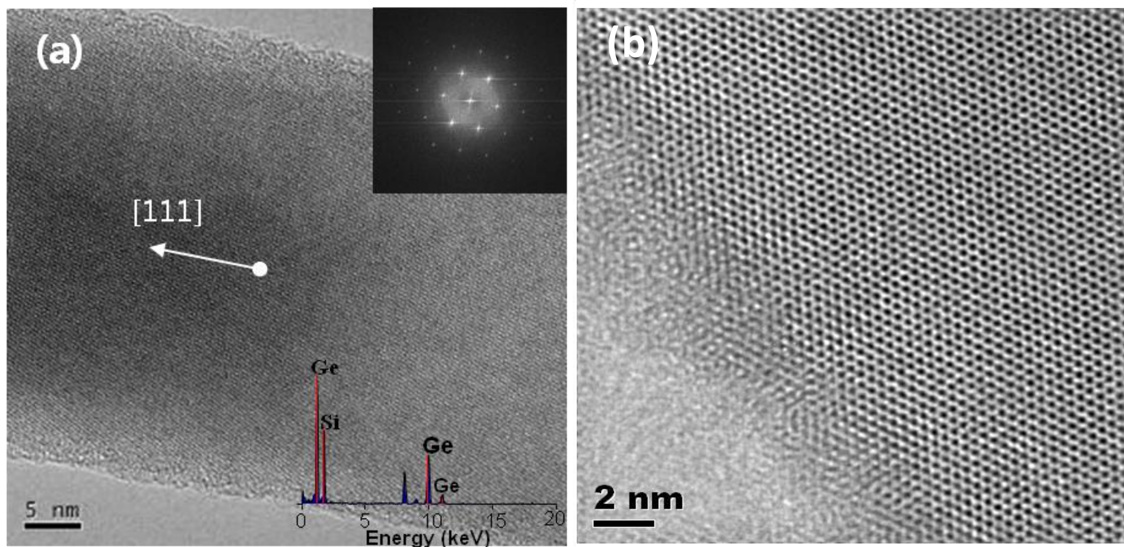

Figure 8. A TEM (a) and a high-resolution TEM (b) of a $Si_{0.9}Ge_{0.1}$ nanowire grown via the VLS method and a selected area electron diffraction pattern in the inset. The growth direction of the nanowire is [111].

2.2 Sample preparation

2.2.1 Micro-device fabrication

The unsuspended micro-devices were fabricated in clean room by Samsung Electric Inc. with projection photolithography. In order to utilize micro-device for the thermoelectric properties measurement, the micro-device should be etched in TMAH

solution to make membranes suspended. The original 4 inch wafer was diced into 15 mm × 15 mm square pieces with 16 micro-devices on each of them. Then, the micro-devices squares were immersed into a mixture solution of 25% TMAH and DI water with the ratio 3:2. The whole solution was keep at 90 ^{o}C for 6 ~ 7 hours and the silicon etching rate was estimated around 80 μm per hour. Once a tiny hole was observed at the center of the micro-device, the etching process should be terminated immediately. Otherwise, the micro-devices will be over-etched and become too thin and fragile to handle, even totally dissolved in the TMAH solution.

2.2.2 Assemble nanowire with micro-device

The wafer with SiGe nanowires grown on were immersed into 5:1 buffered HF solution (J.T.Baker) for 1 min to remove the outer native oxide layer, which prevents good thermally contact between a nanowire and platinum electrode. After the oxide layer was etched away, the wafer was washed thoroughly by DI water. As-synthesized nanowires dispersed in 200 proof ethanol (Koptec) by ultra-sonication for a few seconds. Then, the nanowire suspension was dropped on a micro-device for measuring thermal conductivity of the nanowires. After ethanol was dried, nanowires were often bridged between two suspended membranes of the micro-device, as shown in Figure 9. On the membrane, serpentine Pt lines were patterned to create temperature gradients along the length direction of the nanowires (i.e., heaters) as well as measure temperature (i.e., thermometers). In order to improve thermal contacts between nanowires and platinum electrodes, additional platinum layers were deposited by focused ion beam (FIB) at the contacts between the membranes and nanowires. Annealing bridged nanowire in vacuum

at high temperature can also improve the thermal contacts. Typically, nanowires were annealed in vacuum chamber at 600 ^{o}C with ramping rate 2 ^{o}C/min. Right after the temperature reached 600 ^{o}C, the vacuum chamber was naturally cooled down to room temperature. The vacuum pressure was maintained at approximately 10^{-7} torr through a turbo pump in conjunction with a mechanical pump. Additionally, some of the SiGe nanowires were intentionally annealing in oxygen to make the native oxide layer thicker. The nanowires were placed in 1 inch quartz tube with 10 sccm flow rate oxygen and annealed at 500 ^{o}C with ramping rate 2 ^{o}C/min. When the temperature reached at 500 ^{o}C, the vacuum chamber starts to cool down to room temperature with the same oxygen flow rate.

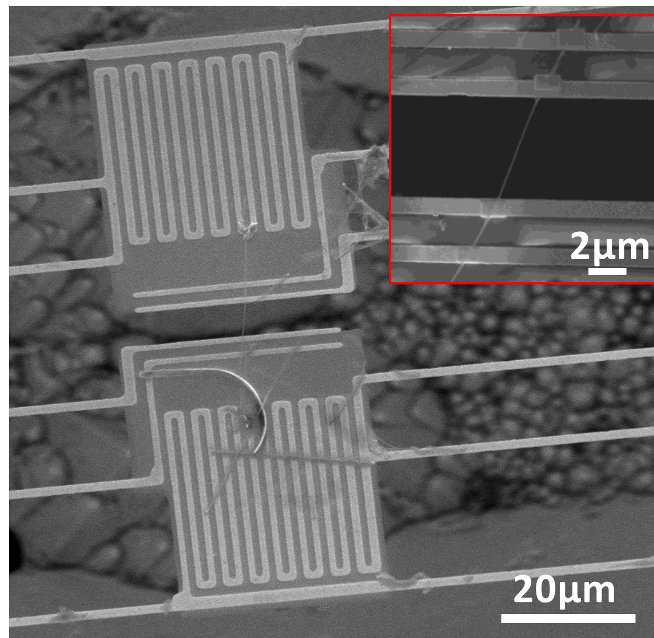

Figure 9. A nanowire is bridged between two suspended membranes. The contacts were improved by using various methods including Ni or Pt depositions as shown in the inset.

After the post-treatment, the micro-device contains bridged nanowire was attached to chip carrier by using silver paint. Then, the Pt pads of the micro device were wire-bonded to the Au pads on the chip carrier with aluminum wires by wire-bonder (Kulicke & Soffa 4500) and transferred into cryostat, as shown in Figure 10.

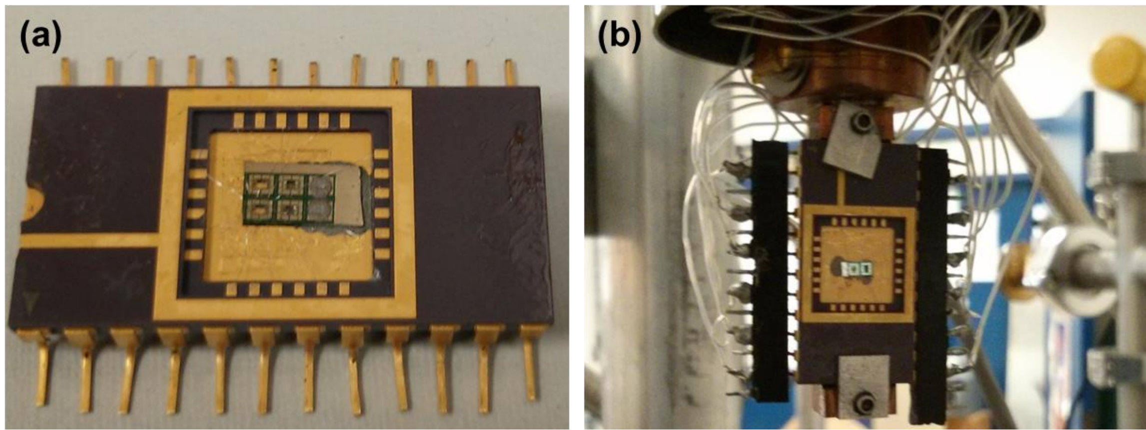

Figure 10. (a) Micro-device inserted in a 24 pin dual in line package (DIP). Electrical connection between micro-device and DIP was made through aluminum wires. (b) Packaged micro-device loaded into the cryostat.

2.3 Experimental setup

Figure 11 shows a schematic diagram of the experimental setup used for the thermoelectric properties measurement of nanowires. The cryostat is directly connected to a mechanical pump, which keeps the pressure in the cryostat lower than 5 mtorr. The compressor cycling helium gas to keeps the temperature in cryostat down by using the principle of the Gifford-McMahon refrigeration cycle. The cryostat was connect to compressor though two gas lines, one of the gas line supplies high pressure helium gas,

while another gas line returns low pressure helium gas from cold head. This pressure drop of helium gas absorbs energy and makes the temperature drop.

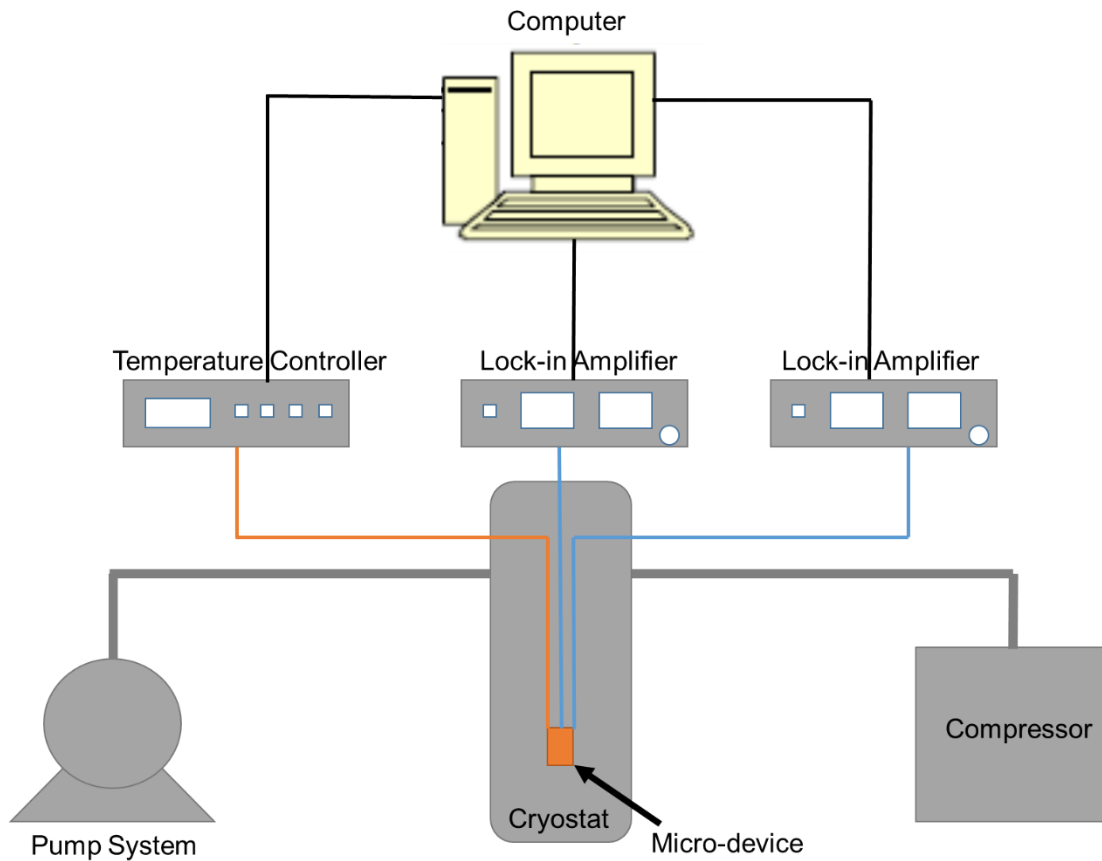

Figure 11. Schematic diagram of the experimental setup for the thermoelectric properties measurement of nanowires.

The chip-carrier with micro-device was attached to the bottom of cryostat system. The micro-device should be isolated from the vibration because of the sensitivity of the measurement in nanoscale. The temperature controller (Lakeshore 330) is connected to the cryostat with a resistance heater embedded at the bottom of the cryostat

near the micro-device. The balance of the cooling power form cryostat and heating power from resistance heater makes steady state temperature condition at the micro-device with 0.1 K accuracy. In this cryostat system, the temperature can be stably controlled at the range 60 K to 450 K. Two lock-in amplifiers (Stanford Research 830) are connected to two membranes on the micro-device through the military socket. The data are collected using a National Instruments data acquisition (DAQ) system. A computer was used to automate the experiment with control of the temperature controller and lock-in amplifiers by Labview.

2.4 Error analysis

The major uncertainties (U) of the measured thermal and electrical conductivities consist of three parts including lengths (L), diameters (D), and multiple measurement values (M), as described in Eq. (8) since k was obtained from measured thermal/electrical conductance values by multiplying geometrical parameters. For thermopower measurement results, the length and diameter were not considered since thermopower does not include any geometrical parameters.

$$\frac{\delta(U)}{U} = \sqrt{\left(\sum \frac{\delta(L)}{L}\right)^2 + \left(4\sum \frac{\delta(R)}{R}\right)^2 + \left(\frac{\delta(M)}{M}\right)^2} \tag{8}$$

The length uncertainty comes from the determination of nanowire lengths since the positions that make thermal/electrical contacts between nanowire and membranes are hard to accurately identify. The width of the electrodes and FIB depositions for contacts are respectively 1~2 μm and 0.5~1 μm. We considered the half of them for each contact

as uncertain lengths. The surface roughness of nanowires was taken from $(R_{max}-R_{min})/2$, where R_{max} and R_{min} are respectively the largest and smallest radius of nanowires. The surface roughness variations, $\delta(D)$ were measured to be 0.2~2 nm. SEM itself has an uncertainty $\delta(L)$ of ~10 nm. The diameter of the sample was measured using a TEM with an uncertainty $\delta(R)$ of 0.5 nm. At each temperature, we measured properties several times to consider measurement errors. We used whole volumes including the oxides to calculate thermal and electrical conductivities. The thermal conductivities are very close to those of only SiGe cores obtained by using a parallel resistor model. It should be noted that geometrical factors are not necessary to obtain ZT as long as all L, S, and k are measured from the exactly same sample.

2.5 Thermal conductivities measurement of SiGe nanowires

The thermal conductivities of SiGe alloy nanowires with different Ge concentrations and diameters were measured at 60-450 K, and the nanowires for the measurements were characterized by electron microscopies. A list of samples for this study is presented in Table 1 with Si:Ge ratio, diameter, oxide thickness, and bridged length between the membranes. Sample 1-4 were undoped or lightly-doped samples, and Sample 5-7 were doped with phosphorous. Sample 1, 5, 6, and 7 were annealed in a vacuumed tube furnace (~10^{-7} Torr) with a ramping rate of 2 ^{o}C/min. When the temperature reached to 600 ^{o}C, the furnace was turned off and naturally cooled. Sample 3 and 4 were annealed in 10 sccm oxygen flow with a ramping rate of 2 ^{o}C/min up to

500 ^{o}C, and subsequently naturally cooled. The natural cooling rate was approximately 10 ^{o}C/min above ~200 ^{o}C and approximately 1 ^{o}C/min below ~200 ^{o}C.[41-43]

Table 1. Si/Ge ratio (total and core), diameter (total and core), length, oxide layer thickness of SiGe nanowires as well as thermal contact enhancement method for measuring thermal conductivity.

Sample #	Si at% Total (Core)	Ge at% Total (Core)	Diameter (nm) Total (Core)	Oxide thickness (nm)	Length (μm)	Contact treatment
1	68 (63)	32 (37)	54.5 (43.5) ±0.4	5.5 ±0.3	4.35	Vac
2	70 (61)	30 (39)	65.6 (52.2) ±0.5	6.7 ±0.3	1.77	FIB
3	69 (51)	31 (49)	75.1 (50.9) ±0.4	12.1 ±0.4	2.42	O_2
4	64 (37)	36 (63)	96 (59.8) ±0.4	18.1 ±0.3	2.26	FIB, O_2
5	93 (92)	7 (8)	74.2 (64.2) ±0.4	5 ±0.3	6.54	FIB, Vac
6	91 (91)	9 (9)	32 (32) ±0.5	0	6.46	FIB, Vac
7	90 (86)	10 (14)	76.5 (59.5) ±0.4	8.5 ±0.3	5.56	FIB, Vac

Figure 12 shows TEM images for Sample 1-7, which are identical samples for thermal conductivity measurements in this study. The dark dots on the surface of the nanowires were identified to be gold that was used as a catalyst for the synthesis. They contain amorphous silicon oxides on their surfaces whose thicknesses vary.

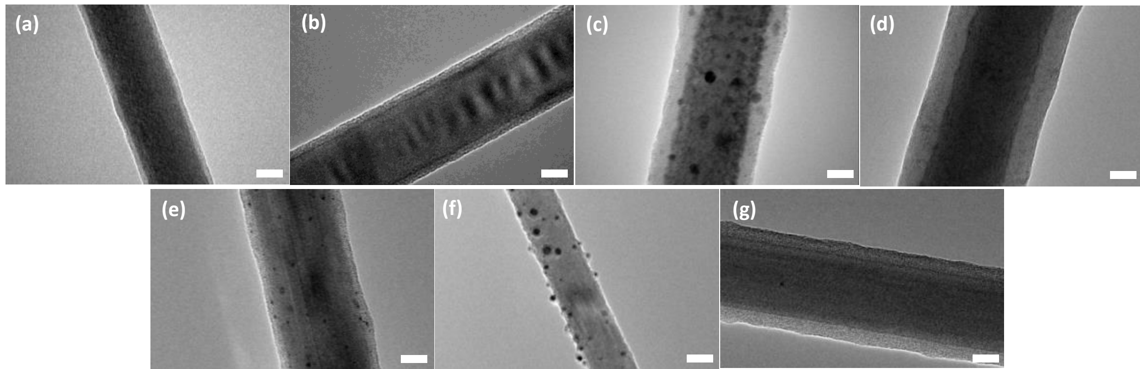

Figure 12. TEM images of Sample 1 (a), 2 (b), 3 (c), 4 (d), 5 (e), 6 (f), and 7 (g) listed in Table 1. The scale bars indicate 20 nm.

It was noticed that dark impurity particle (dots) are located on the surface of the nanowires in some of the TEM images. In Figure 13a and 13c, EDS results show that the dots are Au particles, which were used as catalysts for nanowire synthesis. Figure 13b and 13d show the atomic percentage of phosphorus in the SiGe nanowire is very high.

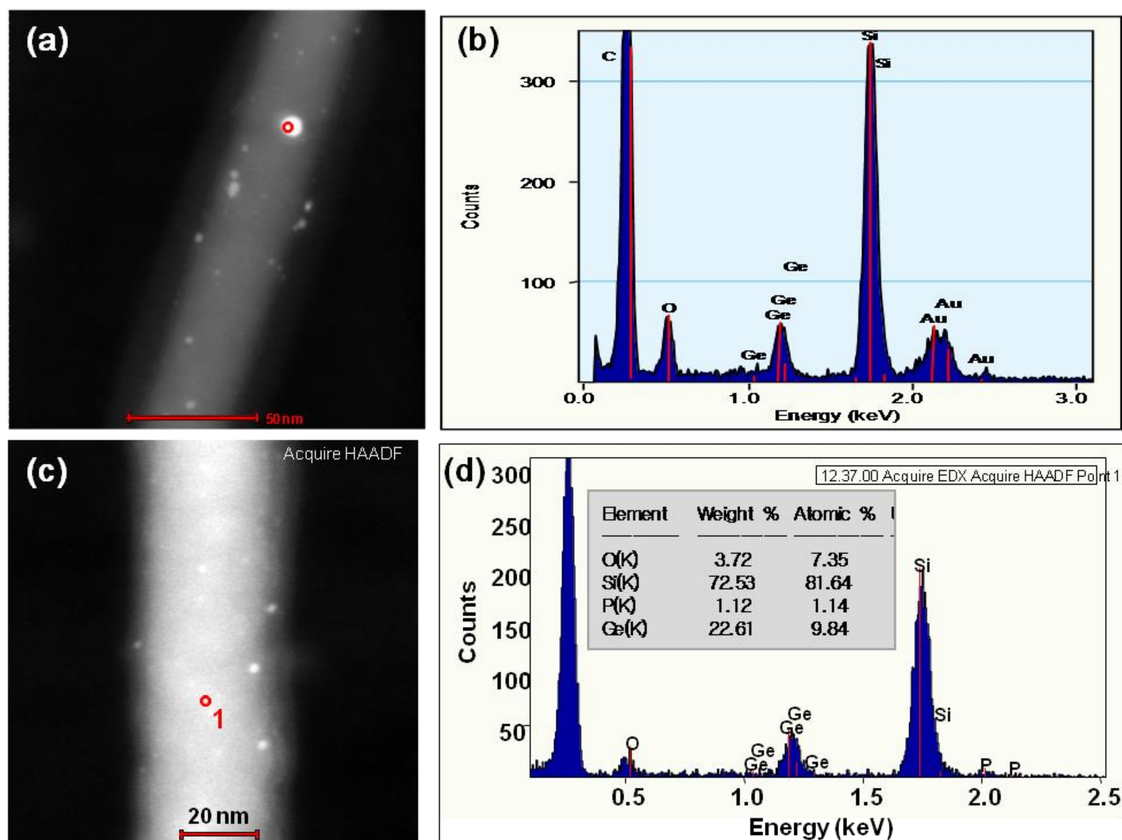

Figure 13. (a, c) High angle annular dark field (HAADF) STEM images. Energy dispersive spectroscopy (EDS) results for the impurity dot (b) and SiGe nanowire (d).

The core consists of SiGe alloy whose at% is different from the result by energy dispersive spectroscopy (EDS) since it includes Si in the silicon oxide layer. Depending on the total diameter of the samples, the contribution of the oxide to thermal conduction is also dissimilar. Therefore, Si:Ge atomic ratios and thermal conductivities for SiGe cores were obtained by using the following method.

Si:Ge atomic ratios for the cores were calculated based on volume and density of the core and shell. The masses of Si ($m_{c\text{-}Si}$) and Ge ($m_{c\text{-}Ge}$) in the core can be described with atomic concentrations of Si (y) and Ge ($1\text{-}y$).

$$m_{\text{c-Si}} + m_{\text{c-Ge}} = [y\rho_{\text{Si}} + (1\text{-}\ y)\ \rho_{\text{Ge}}]\ \text{V}_{\text{core}} \quad (9)$$

$$m_{\text{c-Si}} = \text{AW}_{\text{Si}}yf \text{ and } m_{\text{c-Ge}} = \text{AW}_{\text{Ge}}\ (1\text{-}\ y)\ f \quad (10)$$

where, m_c, f, AW, ρ, and V indicate core mass, multiplying factor, atomic weight, density, and volume of indexed materials, respectively. Then, the atomic ratio (EDS-AR) of Si to Ge from the EDS analysis are respectively described as:

$$\text{EDS-AR(Si:Ge)} = (\text{m}_{\text{c-Si}} + \text{AW}_{\text{Si}} / (\text{AW}_{\text{Si}} + 2\text{AW}_{\text{O}})\ \rho\text{V}) / \text{AW}_{\text{Si}} : (\text{m}_{\text{c-Ge}} / \text{AW}_{\text{Ge}}) \quad (11)$$

The atomic weights of silicon (AW_{Si}), germanium (AW_{Ge}), and oxygen (AW_O) are 28.086, 72.640, and 16.000, respectively. The densities of Si, Ge, and SiO_2 are taken as 2.329 g/cm^3, 5.323 g/cm^3, and 2.200 g/cm^3, respectively.[44-46] The core and shell were considered as two parallel resistors, and the thermal conductivity of the core was calculated by using:

$$k_c = [G_{total}L\text{-}k_sA_s] / A_c \quad (12)$$

where, G_{total}, k_c, k_s, A_c, and A_s represent thermal conductance of the nanowire (including the core and shell) and the thermal conductivity (k) and area (A) of the indexed portion, c (core) or s (shell), respectively.

With 37-63 at% Ge concentrations and 44-60 nm diameters, their thermal conductivities reached the minimum thermal conductivity of SiGe alloys, due to both phonon boundary and alloy scatterings. This is may suggest these parameters result in the smallest achievable thermal conductivity with SiGe. When the nanowire diameter is

close to or less than ~60 nm, it would be more effective to use a higher Ge concentration for further suppressing thermal conductivity rather than reduce diameter.

Thermal conductivity measurements were carried out in a cryostat at 60-450 K. The lower four plots in Figure 14 depict thermal conductivities of Sample 1-4 whose Ge concentrations are relatively high (37-63 at% for the SiGe alloy cores). It appears that phonon transport was strongly deterred by both alloy scattering from the high Ge concentrations and boundary scattering at the surface of the nanowires. At temperatures below ~300 K, the conductivities are extremely low, approaching the minimum thermal conductivity,[47] as shown in Figure 14. This model assumes that vibration of each atom decays at one half the periods. The solid and broken lines respectively indicate the minimum thermal conductivities of SiGe alloys with Ge = 37 and 63 at% by using linear averages for speed of sound and the number density of atoms (values were found in the reference[47]). For instance, speed of sound for Si_yGe_{1-y} is described as $v = y \cdot v_{Si} + (1-y) \cdot v_{Ge}$, where v_{Si} and v_{Ge} are the speed of sound for Si and Ge, respectively. It should be noted that these samples are not intentionally doped, which means electronic contribution to the thermal conductivity is negligible. In other words, this may suggest the smallest thermal conductivity with SiGe can be obtained by confining and scattering phonon transport within approximately 40-50 nm (diameter) and 40-50 at% Ge in Si (alloying).

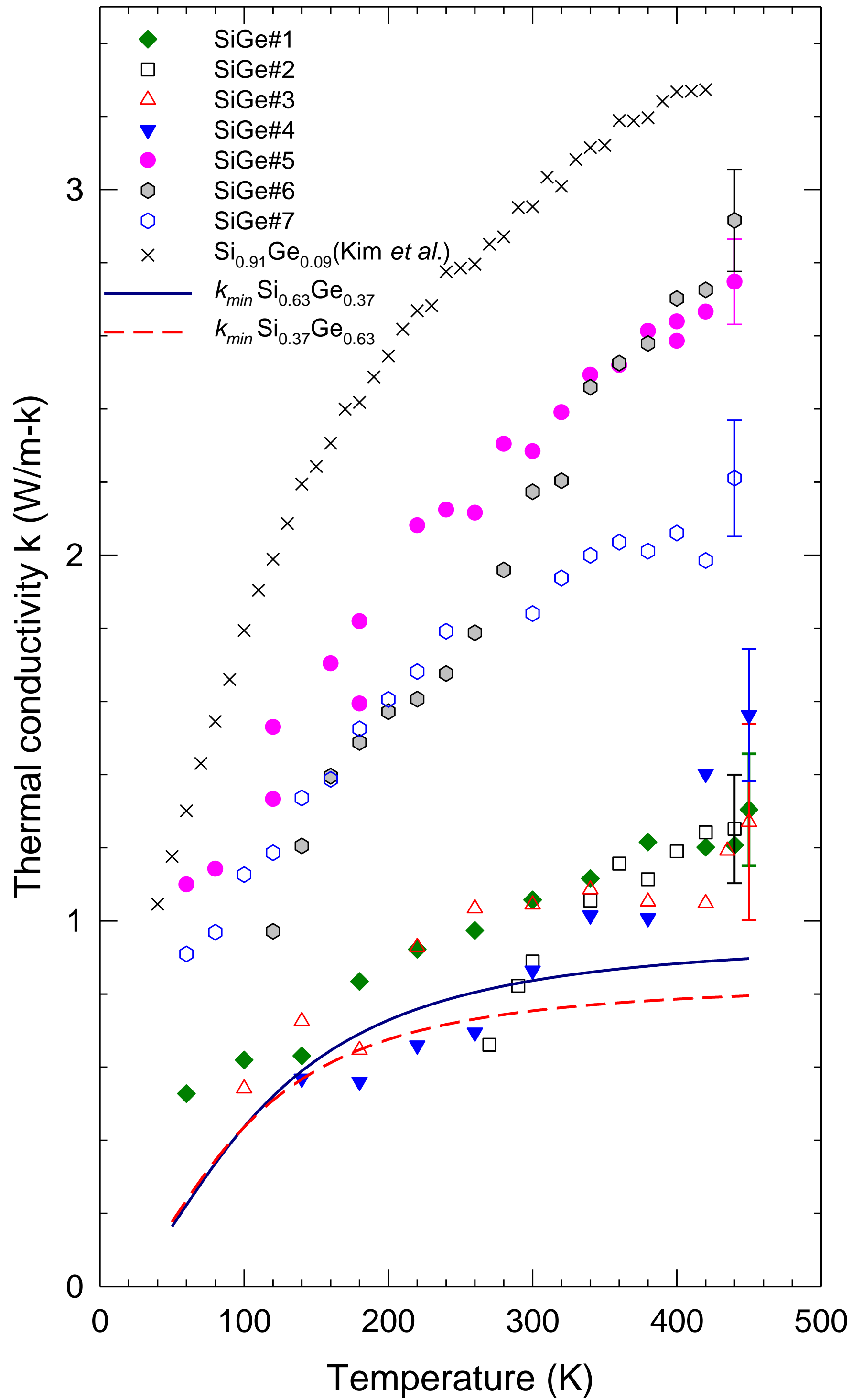

Figure 14. Thermal conductivities of Sample 1-7 and $Si_{0.91}Ge_{0.09}$ with 160 nm in diameter, plotted together with minimum thermal conductivities of $Si_{0.63}Ge_{0.37}$ and $Si_{0.37}Ge_{0.63}$.

Their SiGe core diameters are similar, ranging from 43 to 60 nm, but the bridged nanowire lengths are different. Despite the different lengths, their thermal conductivities are close each other. In particular, Sample 1 has twice longer length than the others, which suggests weak influence of contact resistances between the nanowires and the device membranes on the measurements. The contacts were also treated with different methods (vacuum annealing, FIB, and oxygen annealing), as listed in Table 1. However, we did not observe noticeable dependence of thermal conductivity on the contact treatment methods. We further estimated the contact resistance between the nanowire and membrane. The contact resistance was calculated to be at least one order smaller than the thermal resistance of the nanowire when we assumed the contact width and length are 1 nm and the nanowire diameter, respectively.

Sample 1-4 have silicon oxides of different thickness with similar SiGe core diameters. It was reported that phonons may interfere when oxide layers are present.[48] In our study, however, thermal conductivities for the cores are similar without showing any noticeable interferences from the oxide layer, presumably due to short phonon characteristic lengths from the high Ge concentrations (37-63 at%). It has been found that thermal conductivity of crystalline SiGe alloys rapidly drops as a function of Ge concentration, and then becomes relatively constant with high Ge concentrations.[49, 50] This may imply our calculations with the parallel resistor model are valid. We believe this is related to short mean free paths of phonons in amorphous silicon oxides. One can estimate the mean free paths from $k = (1/3)Cvl$, where k, C, v, and l stand for thermal conductivity, heat capacity, speed of sound, and mean free path length. For amorphous

silicon oxides, l is estimated to be ~1 nm from k = 1.3 W/m-K, $C = 7.26\times10^5$ J/m^3-K, v_t = 3740 m/s, and v_l = 5980 m/s, where v_t and v_l are for transverse and longitudinal phonons. The speed of sound was found from $3/(2v_t^{-1} + v_l^{-1})$.[51]

For Sample 5-7 with low Ge concentrations (8-14 at%), thermal conductivities are higher than those of Sample 1-4 (high Ge concentrations). It should be noted that Sample 5-7 have been doped with phosphorous, but we were not able to measure the electrical properties. This may be attributed to non-Ohmic contacts between the nanowire and membranes. Nevertheless, Sample 5-7 are similar in terms of doping concentrations since they were synthesized with the same conditions. The lower thermal conductivity of Sample 7 than those of the other two samples could be attributed to the relatively higher Ge concentration (14 at%) compared to the others (8 and 9 at%). In general, thermal conductivity dramatically changes when Ge concentration is near 10 at%.[49, 52] In comparison to the $Si_{0.91}Ge_{0.09}$ nanowire whose diameter is 160 nm,[53] the conductivity values for Sample 5-7 are smaller, presumably due to their smaller diameters (32 and 64 nm). This implies that phonons of characteristic lengths (mean free path lengths and wavelengths) longer than ~60 nm still contribute thermal transport in SiGe alloys with 8-9 at% Ge concentrations. These values are slightly higher than those of recently reported doped-SiGe nanowires.[50] We estimated that the doping concentration is $2.5\sim3.3\times10^{20}$ cm^{-3} under the assumption that inactive dopants are non-ionized phosphorus with the concentration of $4.0\sim4.2\times10^{20}$ cm^{-3}, which will be discussed in details in chapter 3.

Although we were not able to measure the electrical properties of sample 5-7, it is still possible to estimate their electrical conductivities by comparing with recently reported doped SiGe nanowires. In our previous paper,[50] all three thermoelectric properties of doped SiGe nanowires have been measured simultaneously. Thermal conductivity contributed by electron and phonon could be determined from $k = k_e + k_p$, and $k_e = \sigma LT$, where k, k_e, k_p, σ, and T stand for total thermal conductivity, electron contributed thermal conductivity, phonon contributed thermal conductivity, electrical conductivity, and absolute temperature. We assume sample 5-7 have the similar phonon contributed thermal conductivity with that of sample $Si_{0.9}Ge_{0.1}$ (45nm) reported in previous paper[50] since they have similar diameter and Ge concentration. Therefore, the electrical conductivities of sample 5-7 at 300K could be estimated as 9.3×10^5 S/m (sample 5), 6.4×10^5 S/m (sample 6), and 1.8×10^5 S/m (sample 7).

The thermal conductivities of our nanowires (approximately 1-2 W/m-K at 300 K) are smaller than those of bulk materials (7.8-8.8 W/m-K for undoped $Si_{0.5}Ge_{0.5}$,[49, 52] 6.1 W/m-K for 1.5×10^{20} cm^{-3} P-doped $Si_{0.9}Ge_{0.1}$ at 300K) and nanostructured bulks (5 W/m-K for P-doped $Si_{0.95}Ge_{0.05}$ at 300K[54]), suggesting that the surface boundary scattering plays a role in suppressing thermal transport. However, it is interesting to see negligible differences between thermal conductivities of the samples whose diameters are 64 nm (Sample 5) and 32 nm (Sample 6). This implies that alloy scattering (i.e., high Ge concentration) is dominant compared to surface boundary scattering when the diameter is close to or smaller than ~60 nm.

In summary, thermal conductivities of SiGe alloy nanowires whose Si:Ge ratio, diameter, and oxide thickness are different in the temperature range from 60 K to 450 K. It was found that thermal conductivity of SiGe alloys was significantly decreased when the alloy was formed into nanowires with Si:Ge atomic ratios close to unity. The large reduction in thermal conductivity is from phonon scattering due to both alloying and surface boundaries. The measured values approached to the minimum thermal conductivity by confining and scattering phonon transport within approximately 40-50 nm (diameter) and 40-50 at% Ge in Si (alloying). Since the electronic contribution to the thermal conductivity is negligible, this may suggest they are the smallest achievable thermal conductivity with SiGe. When the nanowire diameter is close to or less than ~60 nm, it is more effective to use a higher Ge concentration to further suppress thermal conductivity rather than use nanowires with smaller diameters. This suggests that it is not necessary to reduce the diameter down to a few 10's of nm in order to obtain extremely low thermal conductivity, which is very challenging to synthesize nanowires of uniform and small diameters.

2.6 Simultaneously measurement of thermoelectric properties of highly doped SiGe nanowires

In the previous section, the thermal conductivity of SiGe alloys was proved significantly decreased due to the phonon scattering by both alloying and surface boundaries. It should be also noted that electron transport may also be sensitive to impurities and defects in crystalline solids,[9] altering electrical conductivity and/or

thermopower. Therefore, it is very important that all three properties, S, σ, and k ($=k_{electron}+k_{phonon}$) are obtained from the same nanowire so as to properly address the influence of various parameters including diameters, impurities, and defects on thermoelectric transport behaviors. Here, we employed Si-Ge alloy as well as nanowire structures to maximize the depletion of heat-carrying phonons. This results in a thermal conductivity as low as ~1.2 W/m-K at 450 K, showing a large thermoelectric figure-of-merit (ZT) of ~0.46 compared with those of SiGe bulks and even ZT over 2 at 800 K theoretically. All thermoelectric properties were 'simultaneously' measured from the same nanowires to facilitate accurate ZT measurement. The surface-boundary scattering is prominent when the nanowire diameter is over ~100 nm, whereas alloying plays a more important role in suppressing phonon transport for smaller ones, which agrees with the computational results.

Table 2. Parameters of simultaneously measured SiGe nanowires.

Sample	Length (μm)	Diameter (nm)	Oxide thickness (nm)	Metal by FIB	Annealing
$Si_{0.94}Ge_{0.06}$	5.7	56	0	-	Vac
$Si_{0.92}Ge_{0.08}$	6.3	97	0	Ni	H_2
$Si_{0.90}Ge_{0.10}$	5.6	45	0	Ni	H_2
$Si_{0.81}Ge_{0.19}$	5.0	62	0	-	Vac
$Si_{0.74}Ge_{0.26}$	11.6	26	0	Ni	H_2
$Si_{0.73}Ge_{0.27}$	5.3	26	2	Ni	H_2
$Si_{0.59}Ge_{0.41}$	5.2	65	2.8	Pt	-
$Si_{0.14}Ge_{0.86}$	6.2	161	0	-	Vac

A list of the SiGe nanowires tested by simultaneous measurement is shown in Table 2. The Si and Ge atomic ratios, lengths, and total diameters including oxide shells, and oxide layer thickness of the SiGe nanowires are presented. The oxide thickness indicates the length of the amorphous oxide layers in the radial direction from the center axis. In order to obtain both good thermal contacts and Ohmic contacts, nickel or platinum layers were deposited by a FIB system on four contacts between nanowires and micro-device membranes. It has been proved that NiSi/Si behaves as Ohmic contacts.[55] Current-voltage sweeping shows linear behaviors, confirming Ohmic characteristics. A post-annealing at 600 ^{o}C in vacuum (better than 10^{-6} Torr) or in an H_2 environment was performed for further improvement of contacts.

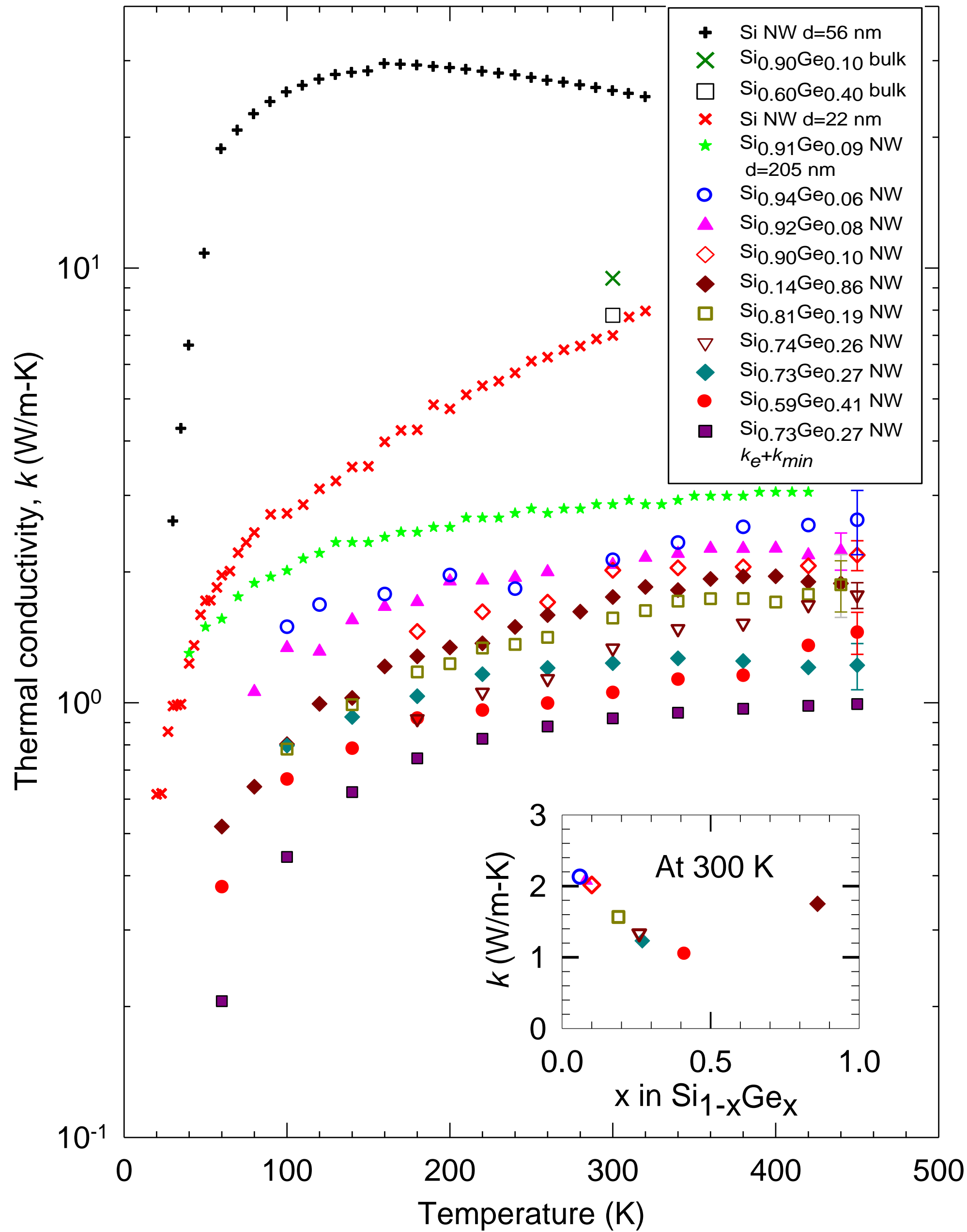

Figure 15. The thermal conductivities of the SiGe nanowires. The thermal conductivities of the SiGe nanowires listed in Table 2 are plotted with those of the previously reported samples including a 56-nm diameter Si nanowire,[11] a $Si_{0.9}Ge_{0.1}$ bulk,[49] a $Si_{0.6}Ge_{0.4}$ bulk,[49] a $Si_{0.91}Ge_{0.09}$ nanowire,[56] and the calculated summation of electronic (k_e) and minimum (k_{min}) thermal conductivities for the $Si_{0.74}Ge_{0.26}$ nanowire. The inset shows the thermal conductivities at 300 K of the SiGe nanowires that were measured in our study.

Figure 15 demonstrates the experimentally measured thermal conductivities of the SiGe alloy nanowires, which rapidly increased at low temperatures and then saturated at 1~2 W/m-K near room temperatures. These values are considerably lower than those of similar-diameter (56 and 22 nm) Si nanowires[11] grown by the VLS method as well as those of three-dimensional $Si_{0.9}Ge_{0.1}$ and $Si_{0.6}Ge_{0.4}$ bulk alloys.[49] Large thermal conductivity reductions up to ~30-fold obtained from the SiGe nanowires compared to the Si nanowire are likely to be derived from the scattering of phonons whose characteristic lengths are smaller than the nanowire diameters. Meanwhile, the low thermal conductivities, 1~2 W/m-K at 300 K, that were obtained for the SiGe 'nanowires' in comparison to 7~8 W/m-K for 'bulk' counterparts indicate that phonons with long characteristic lengths were deterred. These comparisons suggest crucial information: (1) the phonons whose characteristic lengths are smaller than the wire diameter can be further scattered by alloying; (2) a large portion of heat is carried by phonons with long characteristic lengths in alloys. The scattering cross-section is proportional to $(d/\lambda)^4$ like the Rayleigh scattering,[57] where d and λ are respectively the characteristic lengths of impurities and phonons, making phonons with long characteristic lengths in alloys still important in heat transport due to small d/λ in alloys. In fact, calculation results[58] have also suggested that heat transport in bulk SiGe has large contributions from phonons with relatively long (up to micron scale) mean free paths. The boundary confinement effects are conspicuous for nanowires with relatively large diameters (205-nm $Si_{0.91}Ge_{0.09}$[59] and 97-nm $Si_{0.92}Ge_{0.08}$); however, it appears that

smaller diameters (56-nm $Si_{0.94}Ge_{0.06}$ and 45-nm $Si_{0.90}Ge_{0.10}$) do not further influence the thermal conductivity (atomic ratio of Si:Ge ~ 0.9:0.1).

On the other hand, when Ge concentrations were raised from 6 % ($Si_{0.94}Ge_{0.06}$) to 19 % ($Si_{0.81}Ge_{0.19}$) or 41 % ($Si_{0.59}Ge_{0.41}$) with relatively constant diameters (56, 62, and 65 nm, respectively), the thermal conductivities were further suppressed, reaching ~1 W/m-K near room temperature. The thermal conductivities of smaller-diameter (26 nm) but with less Ge samples, $Si_{0.74}Ge_{0.26}$ and $Si_{0.73}Ge_{0.27}$ fit more or less between those of $Si_{0.81}Ge_{0.19}$ and $Si_{0.59}Ge_{0.41}$. The thermal conductivities at 300 K in our experimental results also suggest strong influence of the Ge concentration, as shown in the inset of Figure 15. It is noticeable that the $Si_{0.73}Ge_{0.27}$ nanowire has very low thermal conductivities that are only ~0.2 W/m-K higher than the summation of the electronic thermal conductivity (k_e) and the minimum lattice thermal conductivity (k_{min}). k_e was obtained from the Wiedemann Franz law with a Lorenz number of 2.44×10^{-8} $W\Omega K^{-2}$ and k_{min} was calculated with a constant speed of sound over the temperature range by using the model proposed by Cahill et al.[47]

We intentionally bridged the two wires on microdevices whose gaps between the membranes are different so that the suspended portions are respectively 5.3 and 11.6 µm for $Si_{0.73}Ge_{0.27}$ and $Si_{0.74}Ge_{0.26}$ (samples were simultaneously synthesized). The thermal conductances of $Si_{0.73}Ge_{0.27}$ were approximately twice those of $Si_{0.74}Ge_{0.26}$. Since we measured thermal conductance (G) and then multiplied the geometrical factors to obtain the thermal conductivity ($k = G\times L/A_c$, where A_c and L are the cross-sectional area and length of the wire, respectively), thermal contact resistances between the wires and

membranes are not likely to significantly influence the measurement results. The total thermal resistances from the measurements (across the wire length) are on the order of 10^8 K/W or higher, whereas the contact resistances are estimated to be smaller than $\sim 5\times10^6$ K/W. The contact resistance was obtained by assuming the contact width and thermal conductivity are respectively 10 nm and 0.5~1 W/m-K at 150 K and 300 K.[13] The contact widths were also underestimated because the contact area deposited by focused ion beam is typically greater than $0.5\times1\ \mu m^2$. Furthermore, we tested different approaches to improve the thermal contacts, such as Pt or Ni depositions on four (or two) contacts with/without thermal annealing or only vacuum annealing (no deposition), for similar nanowires, $Si_{0.94}Ge_{0.06}$, $Si_{0.92}Ge_{0.08}$, and $Si_{0.90}Ge_{0.10}$ so as to exclude the possibility of dominant effects from contact resistances. We did not observe any noticeable differences depending on the aforementioned contact treatments.

The electrical properties and *ZT* of the $Si_{0.92}Ge_{0.08}$, $Si_{0.90}Ge_{0.10}$, $Si_{0.74}Ge_{0.26}$, and $Si_{0.73}Ge_{0.27}$ nanowires are plotted in Figure 16 with those of a radioisotope thermoelectric generator (RTG) sample that was typically used for NASA space flight[60] for comparison. Unlike thermal conductivity, the electrical conductivities are less sensitive to diameter and Ge concentration, presumably due to short electron mean free paths. The electrical conductivities of the nanowires are inferior to those of the RTG bulk sample. On the other hand, the absolute thermopower values from $Si_{0.90}Ge_{0.10}$ and $Si_{0.74}Ge_{0.26}$ are larger than those from the RTG, making the power factors from nanowires close to those of the RTG. With much lower thermal conductivities from the nanowires than the bulk, $Si_{0.73}Ge_{0.27}$ shows a large *ZT* improvement of up to ~0.46 at 450

K, which is twice that of the RTG, as shown in Figure 16c. This result is over 50 % higher than that of the p-type nanostructured-bulk SiGe alloy[61] and ~30 % higher than that of the n-type nanostructured-bulk SiGe alloy,[62] respectively. It should be noted that errors associated with geometrical parameters are not involved. These parameters are not necessary to obtain ZT as long as all σ, S, and k are measured from the same sample.

Furthermore, even higher ZT values up to 2.2 at 800 K were estimated from calculated electrical conductivity, thermopower, and lattice thermal conductivity based on the Boltzmann transport equation up to 800 K, as plotted with lines in Figure 16. The electrical properties were calculated by using the model for 'bulk' SiGe proposed by Vining,[63] considering both electrons and holes as well as two major scattering mechanisms due to acoustic phonons and ionized impurities. The electron mean free paths are estimated to be shorter than the wire diameter, which is likely to make the electrical transport properties of bulks similar to those of the nanowires.

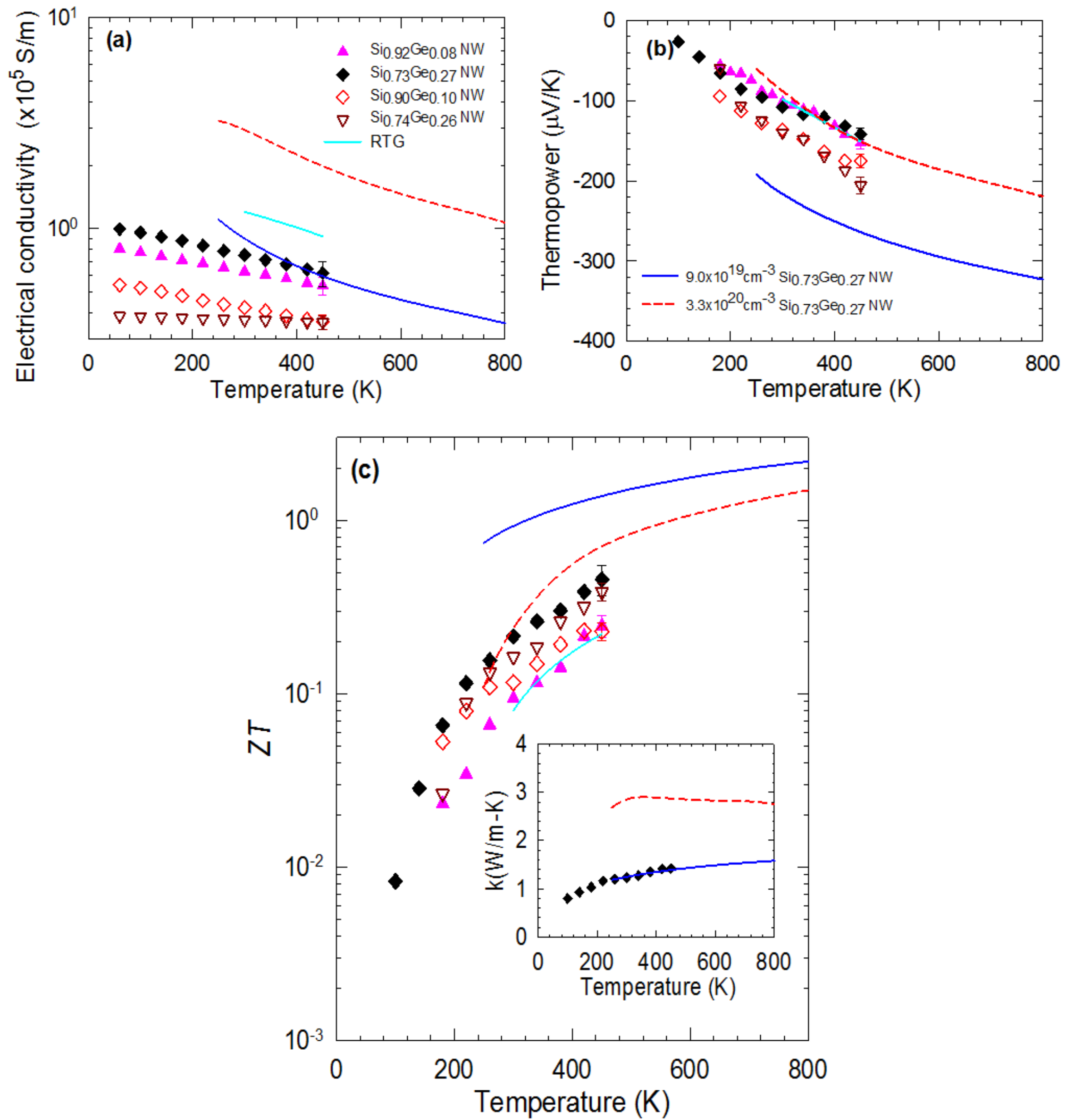

Figure 16. Simultaneously measured (60-450 K) and theoretically calculated (250-800 K) electrical conductivity, thermopower, and the figure-of-merit (ZT) of the SiGe nanowires. (a) Electrical conductivity, (b) thermopower, and (c) ZT values are plotted for $Si_{0.92}Ge_{0.08}$, $Si_{0.90}Ge_{0.10}$, $Si_{0.74}Ge_{0.26}$, and $Si_{0.73}Ge_{0.27}$ with those of a bulk SiGe RTG[14] as reference values. Calculated results were obtained with two different carrier densities, 9.0×10^{19} (blue-solid line) and 3.3×10^{20} cm^{-3} (red-broken line) for $Si_{0.73}Ge_{0.27}$.

In Figure 16a and b, the blue-solid and red-broken lines respectively represent electrical properties of bulk SiGe when either electrical conductivity or thermopower is similar to those of the $Si_{0.73}Ge_{0.27}$ nanowire. Corresponding carrier densities were found to be 9.0×10^{19} and 3.3×10^{20} cm^{-3} for the blue and red lines, respectively. The discrepancies in the experimental values from the nanowires and those from bulk SiGe (calculation) are presumably due to inferior electrical properties of the nanowires compared to those of bulks. The confined structure often makes electron transport very sensitive to impurities, non-uniformly distributed dopants,[64, 65] and/or deactivated dopants.[66] For example, electrical conductivity may significantly drops even with high carrier concentrations when a small cylindrical section in the middle (along the nanowire axial direction) of the nanowire is electrically less conducting.

High-temperature thermal conductivities up to 800 K were obtained by calculating both lattice and electronic thermal conductivities. The lattice and electronic thermal conductivities were calculated with the Callaway model modified by Mingo[67] and Morelli et al.[68] and the Wiedemann Franz law, respectively. The relatively high thermal conductivity with the higher carrier density (3.3×10^{20} cm^{-3}) is due to the electronic contribution to the total thermal conductivity. In order to fit our experimental data, the cut-off frequency was used as an adjustable parameter when normal phonon scattering, phonon-phonon Umklapp scattering, impurity scattering, electron-phonon scattering, and scattering from the wire boundary were considered. The projected *ZT* value at 450 K is 1.4, higher than that of Bi-Te based state-of-the-art alloys, and is even

much higher, 2.2 at 800 K when Si is alloyed with Ge by 27%, under the assumption that the electrical properties of nanowires are similar to those of bulk SiGe.

Upon further optimizing the nanowire synthesis process, it may be possible to obtain electrical properties close to those of bulks with a high concentration of phosphorous doping and followed by thermal annealing. When Si is oxidized due to the presence of oxygen, it has been found that phosphorus can diffuse into Si (i.e., segregates from SiO_2 shells) and Ge as well as accumulate at the interface between Si and SiO_2.[64, 65, 69] As shown in the supplementary information, energy dispersive spectroscopy profiles show the presence of phosphorus in the core region of our samples. Upon optimized synthesis and/or thermal annealing processes, it may be possible that dopants are more uniformly distributed without deactivated dopants, resulting in improved electrical properties.

In conclusion, we report a large improvement in *ZT* values, experimentally ~0.46 at 450 K and computationally 2.2 at 800 K, from SiGe nanowires. The experimental results were obtained by "simultaneously" measuring thermal conductivity, electrical conductivity, and thermopower. It is crucial to obtain all three properties from the same nanowire since their compositions, crystallinity, and thermoelectric properties might vary considerably even for the samples that are grown at the same time. The *ZT* improvement is attributed to remarkable thermal conductivity reductions, which are thought to derive from the effective scattering of a broad range of phonons by alloying Si with Ge as well as by limiting phonon transport within the nanowire diameters. Surface boundary scattering is prominent when the nanowire diameter is ~100 nm or

larger, whereas Ge alloying plays a more important role in suppressing the thermal conductivity of smaller diameter samples. The additional phonon scattering in alloy nanowires might provide opportunities to use relatively large-diameter nanowires for maintaining the structural integrities required for building practical nanowire-based thermoelectric energy conversion devices in the future.

CHAPTER III

SIMULATION OF THERMOELECTRIC PROPERTIES OF SIGE NANOWIRES

In the previous chapter, simultaneously measured thermoelectric properties of SiGe nanowires were reported with ZT values as high as 0.46 at 450 K due to large thermal conductivity reductions from alloying and confined wire structures.[70, 71] Even higher ZT values from SiGe nanowires are expected at higher temperatures with bulk-like electrical properties. In order to better understand thermoelectric properties of heavily doped SiGe nanowires and estimate the highest achievable ZT values at high temperature, it is necessary to have theoretical calculations. In the past, models were developed only for SiGe bulks by Vining,[63] Slack,[68, 72] and Chen.[73] However, these models are not in good agreement with the reported properties of SiGe nanowires.

In this chapter, we proposed models for electrical conductivity, thermopower, and thermal conductivity of heavily doped SiGe nanowires at high temperatures, based on the Boltzmann transport equation with the relaxation-time approximation.

3.1 Electrical conductivity and thermopower modeling

In semiconductors, both electrons and holes exist at the same time. Thus, electrical conductivity was calculated by summing two parts from electrons and holes.[74, 75]

$$\sigma = \sigma_e + \sigma_h \tag{13}$$

Based on the Boltzmann transport equation, the electrical conductivity can be expressed as:[76]

$$\sigma_j = \frac{q^2}{3\pi m_j^*}\int_0^\infty \kappa^3 \tau_j \frac{\partial F_0}{\partial \kappa} d\kappa \tag{14}$$

where, $j = e$ (electrons) or h (holes), κ is the wave vector. $F_\eta(\mu^*)$ is the Fermi integral with η index, which is described as:

$$F_\eta(\mu^*) = \int_0^\infty \frac{(\varepsilon_j^*)^\eta d\varepsilon_j^*}{1+\exp(\varepsilon_j^* - \mu^*)} \tag{15}$$

The reduced chemical potential (μ^*) is relative to conduction band edge, which can be obtained from:

$$N_e = \frac{\sqrt{2}(m_e^* k_B T)^{1.5}}{\pi^2 \hbar^3} F_{1/2}(\mu^*) \tag{16}$$

$$N_h = \frac{\sqrt{2}(m_h^* k_B T)^{1.5}}{\pi^2 \hbar^3} F_{1/2}(-E_g^* - \mu^*) \tag{17}$$

where, N_e and N_h are the concentration of electrons and holes, respectively. E_g^* is the reduced band gap and it can be calculated based on Krishnamurthy theory[77] by:

$$E_g^* = \frac{0.8941 + 0.0421y + 0.1691y^2}{k_B T} \tag{18}$$

where, y stands for Ge concentration ($0<y<1$).

After the wave vector in Eq. (14) was changed as function of energy by applying $\varepsilon = h^2\kappa^2 / (8\pi^2 m)$, Eq. (14) can be rewritten by integrating this expression by parts, as:

$$\sigma_j = \frac{8\pi q^2}{3 m_j^* h^3}(2 m_j^* k_B T)^{1.5}\int_0^\infty \frac{\partial F_0(\mu^*)}{\partial \varepsilon_j^*}(\varepsilon_j^*)^{1.5}\tau_j d\varepsilon_j^* \tag{19}$$

Since $F_o(\mu^*)$ is the Fermi integral with 0 index

$$\sigma_j = \frac{8\pi q^2}{3m_j h^3}(2m_j k_B T)^{1.5} \int_0^{\infty} \frac{\tau_j \varepsilon_j^{1.5} e^{(\varepsilon_j - \mu)}}{\left[1 + e^{(\varepsilon_j - \mu)}\right]} d\varepsilon_j \tag{20}$$

Electrical conductivity depends on absolute temperature and electron/hole relaxation times. Electrons and holes may interact with a great variety of scattering centers, such as ionized and non-ionized impurities, acoustic and optical phonons, and altering the relaxation time. Here we considered the scattering by the impurities (both ionized and non-ionized) and acoustic phonons, which have found to be the most influential.[76, 78] These scatterings often occur simultaneously, which can be combined by applying the Matthiessen's rule.

$$\frac{1}{\tau_j} = \frac{1}{\tau_{jA}} + \frac{1}{\tau_{jI}} + \frac{1}{\tau_{jN}} \tag{21}$$

Carrier scattering by the acoustical vibration of the lattice atoms can be obtained by using the deformation potential method.[79, 80] The relaxation time due to scattering by longitudinal and transverse acoustical phonon can be written as: [75, 80]

$$(\tau_{jA,i})^{-1} = \frac{\sqrt{2}E^2 (m_j^* k_B T)^{1.5}}{\pi \hbar^4 v_i \rho} (\varepsilon_j^*)^{0.5} \tag{22}$$

where, v is the phonons' speed of sound, subscript i stands for either longitudinal (i=L) or transverse (i=T) phonon model, E is the deformation potential and ρ is the mass density and can be expressed as:

$$\rho = M / V \tag{23}$$

where,

$$M = (1 - y)M_{Si} + yM_{Ge} \tag{24}$$

$$V = (1-y)V_{Si} + yV_{Ge} \tag{25}$$

Here, M is the average mass of an atom in the crystal, V is the volume per atom and both were assumed to be linear average between the properties of Si and Ge. Similarly, the speed of sound and effective mass for SiGe alloys can be expressed as:

$$v_i = (1-y)v_{Si,i} + yv_{Ge,i} \tag{26}$$

$$m_j^* = (1-y)m_{Si,j}^* + ym_{Ge,j}^* \tag{27}$$

Ionized and non-ionized impurities also affect the motion of charge carriers. An ionized impurity scatters the carriers by serving as a center of a long range coulomb field. Its potential energy is related to the macroscopic permittivity.[76, 81, 82] The relaxation time by the ionized impurity scattering can be written as:[76, 81, 83]

$$\left(\tau_{jI}\right)^{-1} = \frac{\pi q^4 N_i g}{\sqrt{2m_j^*}\chi^2}(k_B T)^{-1.5}(\varepsilon_j^*)^{-1.5} \tag{28}$$

where,

$$g = \ln\left[1 + \left(\frac{3\chi k_B T}{q^2 N_i^{1/3}}\right)^2\right] \tag{29}$$

N_i is the ionized impurity concentration, which equals the sum of electron concentration (N_e) and hole concentration(N_h),[83] since both electrons and holes will contributed to scatter the carriers as the ionized scattering center under the influence of electric field.

In heavily doped semiconductors, non-ionized impurities can serve as point defects to scatter electrons. The concentration of them may reach very high values, comparable with that of the ionized impurity.[84] Consequently, the role of non-ionized

impurity scattering should not be neglected in electrical properties simulation. The relaxation time by the non-ionized impurity scattering can be given as:[76, 85, 86]

$$\left(\tau_{jN}\right)^{-1} = \frac{20\hbar^3 \chi N_n}{(m_j^*)^2 q^2} \tag{30}$$

Thermopower (S) was calculated by considering both electron and hole parts:[75]

$$S = (S_e\sigma_e + S_h\sigma_h)/\sigma \tag{31}$$

Thermopower of electrons and holes can be derived by using the Boltzmann equation under the condition of only temperature gradient.[76]

$$S_j = -\frac{k_B}{q}\left[\frac{\int_0^\infty \kappa^3 \tau_j \frac{\partial F_0(\mu^*)}{\partial \kappa} \varepsilon d\kappa}{\int_0^\infty \kappa^3 \tau_j \frac{\partial F_0(\mu^*)}{\partial \kappa} d\kappa} - \mu^*\right] \tag{32}$$

Converting the wave vector into the dimensionless energy format, thermopower for electrons is expressed as:

$$S_e = -\frac{k_B}{q}\left[\frac{\int_0^\infty (\varepsilon^*)^{5/2} \tau_e \frac{\partial F_0(\mu^*)}{\partial \varepsilon^*} d\varepsilon^*}{\int_0^\infty (\varepsilon^*)^{3/2} \tau_e \frac{\partial F_0(\mu^*)}{\partial \varepsilon^*} d\varepsilon^*} - \mu^*\right] \tag{33}$$

Thermopower for holes can be obtained by substituting $-E_g^*-\mu^*$ for μ^*

$$S_h = \frac{k_B}{q}\left[\frac{\int_0^\infty (\varepsilon^*)^{5/2} \tau_h \frac{\partial F_0(-E_g^*-\mu^*)}{\partial \varepsilon^*} d\varepsilon^*}{\int_0^\infty (\varepsilon^*)^{3/2} \tau_h \frac{\partial F_0(-E_g^*-\mu^*)}{\partial \varepsilon^*} d\varepsilon^*} + E_g^* + \mu^*\right] \tag{34}$$

3.2 Thermal conductivity modeling

3.2.1 Phonon thermal conductivity

Thermal conductivity was calculated based on the Boltzmann transport equation with an adjusted dispersion model. In the past, Callaway's model,[87, 88] Holland's model[88] and Morelli's model[89] have been proven to be successful in fitting the thermal conductivity of bulk materials. However, these models are based on linear phonon dispersion and experimental data did not agree with the results for small diameter Si nanowires. Mingo *et al*. calculated phonon dispersions for Si nanowires instead of using linear dispersions to estimate the thermal conductivity.[67, 90] However, performing complete phonon dispersion requires construction of dynamical matrix of the system, which is complicated and difficult for SiGe alloy. Here, we further modified Callaway's model for calculating thermal conductivity (k) of nanowires. In our model the lattice thermal conductivity (k_l) was obtained by summing those from one longitudinal (k_L) and two degenerate transverse (k_T) phonon branches:

$$k_l = \frac{1}{3}(k_L + 2k_T) \tag{35}$$

k from the longitudinal and transverse phonons can be expressed as:[87, 89]

$$k_i = \frac{k_B^4 T^3}{2\pi^2 \hbar^3}\left(\frac{1}{v_i}\right)\left(I_{i1} + \frac{{I_{i2}}^2}{I_{i3}}\right) \tag{36}$$

where, $i = L$ (longitudinal mode) or T (transverse mode).

$$I_{i1} = \int_0^{\theta_i/T} \tau_{p,i} \frac{x^4 e^x}{(e^x - 1)^2} dx \tag{37}$$

$$I_{i2} = \int_0^{\theta_i/T} \frac{\tau_{p,i}}{\tau_{pN,i}} \frac{x^4 e^x}{(e^x - 1)^2} dx \tag{38}$$

$$I_{i3} = \int_0^{\theta_i/T} \frac{\tau_{p,i}}{\tau_{pN,i}\tau_{pR,i}} \frac{x^4 e^x}{(e^x - 1)^2} dx \tag{39}$$

where, x is the reduced energy for phonon and θ_i is the Debye temperature.

$$x = \frac{\hbar\omega}{k_B T} \tag{40}$$

In our model, the phonon relaxation time was obtained by considering multiple phonons scatterings including phonon-phonon normal scattering, phonon-phonon Umklapp scattering, phonon-alloy scattering, phonon-boundary scattering, phonon-cluster scattering and phonon-electron scattering. These scattering mechanisms usually act simultaneously and can be added up by applying the Matthiessen's rule.

$$\frac{1}{\tau_{p,i}} = \frac{1}{\tau_{pN,i}} + \frac{1}{\tau_{pR,i}} \tag{41}$$

where

$$\frac{1}{\tau_{pR,i}} = \frac{1}{\tau_{pU,i}} + \frac{1}{\tau_{pA,i}} + \frac{1}{\tau_{pB,i}} + \frac{1}{\tau_{pC,i}} + \frac{1}{\tau_{pE,i}} \tag{42}$$

The relaxation time for the normal scattering can be written as:[89, 91]

$$(\tau_{pN,L})^{-1} = \frac{k_B^5 \gamma_L^2 V}{M v_L^5 \hbar^4} x^2 T^5 \tag{43}$$

$$(\tau_{pN,T})^{-1} = \frac{k_B^5 \gamma_T^2 V}{M v_T^5 \hbar^4} x T^5 \tag{44}$$

The relaxation time for the Umklapp scattering can be expressed as:[89, 92-95]

$$(\tau_{pU,i})^{-1} = \frac{\hbar\gamma_i^2}{Mv_i^2\theta_i}\left(\frac{k_B}{\hbar}\right)^2 x^2T^3e^{-\theta_i/3T} \quad (45)$$

The Grüneisen parameter (γ_i) is a fitting parameter, which is generally in the range of 0.9~1.3 for the longitudinal mode and 0.3~1.0 for the transverse mode.[89] With γ_L = 1.1and γ_T = 0.6, the calculated k of bulk Si and bulk Ge are well matched with experimental results.[89] Here, we used the same Grüneisen parameter values since the Umklapp scattering is less likely to change as a result of the wire morphology in our study.

The impurity scattering can be written as:[89]

$$(\tau_{pA,i})^{-1} = \Gamma\frac{V}{4\pi v_i^3}\left(\frac{k_BT}{\hbar}\right)^4 x^4 \quad (46)$$

where,

$$\Gamma = (1-y)\left(\frac{M_{Si}-M}{M}\right)^2 + y\left(\frac{M_{Ge}-M}{M}\right)^2 \quad (47)$$

The relaxation time due to the phonon scattering by the boundary (surface) of nanowire is a strong function of surface specularity:[96]

$$(\tau_{pB,i})^{-1} = \frac{v_i}{d}\left(\frac{1-\alpha}{1+\alpha}\right) \quad (48)$$

α = 1 indicates specular reflection and α = 0 indicates completely diffusive scattering.

The relaxation time due to non-ionized or Ge clusters can be written as:[97, 98]

$$(\tau_{pC,i})^{-1} = \frac{2\pi v_iD_CR_C^6k_B^4x^4T^4}{k_B^4R_C^4x^4T^4+\hbar^4v_i^4} \quad (49)$$

where, D_C and R_C are the density and radius of the cluster, respectively. Note that the factor of 2 was multiplied to the scattering cross section due to the diffraction near the edge of the cluster.[98, 99] Phonon-electron scattering also gives rise to a relaxation time:[100, 101]

$$(\tau_{pE,i})^{-1} = \frac{E^2 (m^*)^3 v_i}{4\pi\hbar^4 \rho\beta_i} \left\{ x - \ln\left[\frac{1+e^{(\beta_i - \mu^* + x^2/(16\beta_i) + x/2)}}{1+e^{(\beta_i - \mu^* + x^2/(16\beta_i) - x/2)}} \right] \right\} \tag{50}$$

where,

$$\beta_i = \frac{m^* v_i^2}{2k_B T} \tag{51}$$

3.2.2 Electric thermal conductivity

Thermal conductivity (k) has two contributions: lattice thermal conductivity (k_l) and electron thermal conductivity (k_e).

$$k = k_l + k_e \tag{52}$$

The electric thermal conductivity was calculated by using the Wiedemann-Franz Law with the Lorenz number, $L = 2.44\times10^{-8}$ WΩ K^{-2}.

$$k_e = \sigma L T \tag{53}$$

3.3 Results and discussion

Our experimental work[71, 102] reported the electrical conductivity, thermopower, and thermal conductivity of SiGe nanowires, which have been used for finding fitting parameters in our calculations. In the experiment,[71] these thermoelectric properties were

simultaneously measured in order to avoid large measurement uncertainties in case that the properties were measured from different samples. For the electrical property calculation, the most important parameters are the electronic carrier density and relaxation time. Vining proposed a model[75] for heavily doped SiGe bulks by considering only acoustic phonon scattering (Eq. (22)) and ionized impurity scattering (Eq. (28)) to calculate the relaxation time. It should be noted that Eq. (29) is different from the equation in the Vining's model, which is borrowed from the Brooks-Herring's approximation[76, 82] that is applicable for semiconductors of low carrier concentrations at high temperatures.[83] Here we used the Conwell-Weisskopf approximation[76, 81] for our highly-doped SiGe nanowires for Eq. (29).

When only these two scattering mechanisms were considered for SiGe nanowires, electrical conductivity and thermopower obtained by Eq. (20) and Eq. (32) do not agree with the experimental data for $Si_{0.73}Ge_{0.27}$, as shown in Figure 17. While the simulated electrical conductivity of $Si_{0.73}Ge_{0.27}$ well matches the experimental data with a carrier density of 9×10^{19} cm^{-3}, the calculated thermopower (absolute values) with the same carrier density is much larger than the experimental values. Higher carrier densities 3.3×10^{20} cm^{-3} was required to fit the experimental data of thermopower as shown in Figure 17b. Again, this higher carrier density increases the electrical conductivity above the experimental values. With either carrier density, the calculated power factor ($S\sigma^2$) for nanowires is much larger than the experimental data. Therefore, it is necessary and important to have a better model for calculating the electrical properties of heavily doped SiGe nanowires.

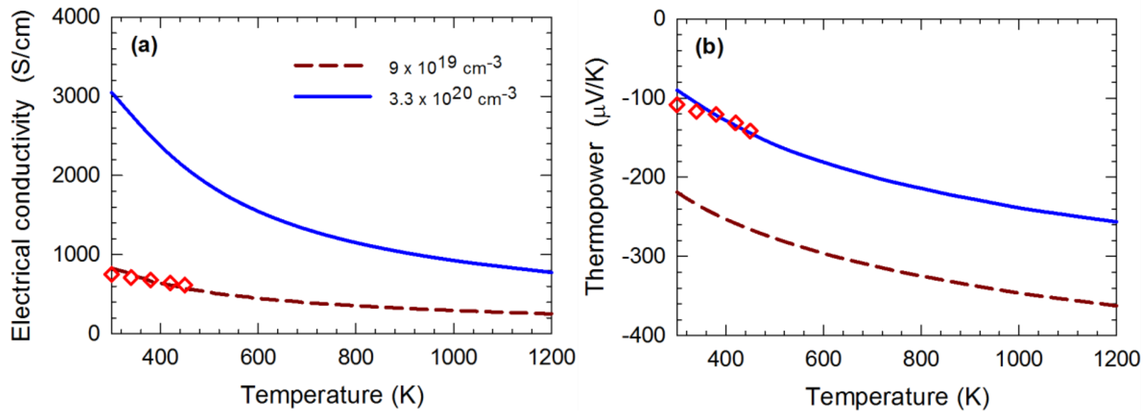

Figure 17. Simulated electrical properties of heavily doped SiGe nanowire without considering non-ionized doped phosphorus.

In heavily doped n-type semiconductors, especially heavily doped with phosphorus, the free carrier density is typically smaller than the dopant density. The density difference increases as the dopant density gets higher.[84, 103, 104] When the dopant density is low or moderate, most of phosphorus atoms are individually separated and randomly distributed in Si or Ge.[105-108] Based on ionization energy model, the extra electron from phosphorus is bound within a certain length, which is on the order of several inter-atomic spacing of the semiconductor crystal. With a high dopant density, the interatomic distance between phosphorus atoms becomes short, and they eventually form into various size dopant clusters.[108-113] When the dopant density reaches over 1×10^{18} cm^{-3}, dopant clusters become more abundant than individually isolated phosphorus atoms.[111] When the dopants are clustered, some of the dopant can captured by vacancy and form vacancy donor pair, so called E-center.[114-116] These E-center act as electron traps and captured electrons cannot move from one center to another. In other

words, these dopant clusters cannot be treated as ionized impurities that contribute to electrical conduction by supplying free electrons. Inversely, these non-ionized dopant clusters suppress electrical conductivity by reducing electron concentration and scattering free carriers. This form of scattering is unimportant when the dopant density is low due to relatively small dopant clusters. For instance, when the impurity density is 10^{18} cm^{-3}, ~77% and ~97% phosphorus in Si are ionized respectively at 300 K and 800 K.[84] However, when the impurity density is higher than 10^{20} cm^{-3}, the non-ionized impurity becomes non-negligible and play important role in electron transport. The phenomenon of localized electrons besides free electrons work together in electron transport was called inhomogeneity model,[117, 118] which has been applied for thermal properties[119-121] simulation for bulk semiconductors in the past.

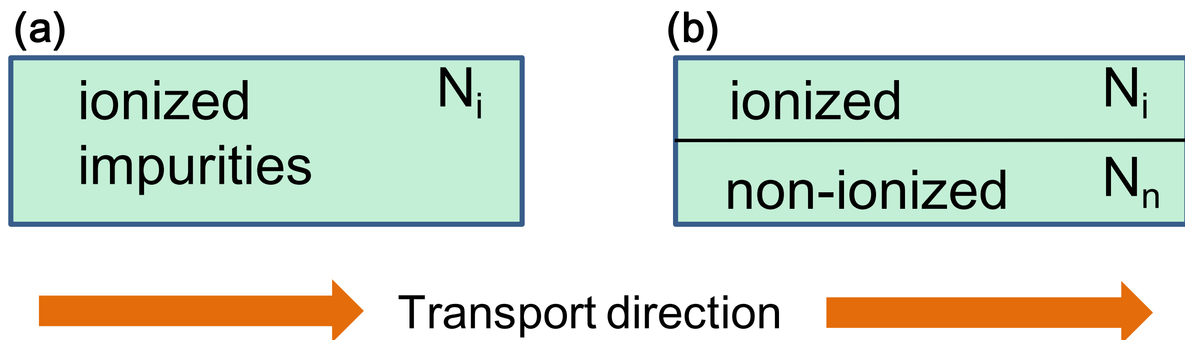

Figure 18. A schematic diagram of two materials with just ionized impurities (a) and both ionized and non-ionized impurities (b).

Table 3. Si/Ge ration, doping condition, diameter, ionized and non-ionized impurity concentration of SiGe nanowires.

Sample	Doping condition	Diameter (nm)	N_i (10^{20} cm^{-3})	N_n (10^{20} cm^{-3})	P cluster radius (nm)
$Si_{0.92}Ge_{0.08}$	Doped	97	2.5	4	0.2
$Si_{0.90}Ge_{0.10}$	Doped	45	1.7	4.2	0.18
$Si_{0.73}Ge_{0.27}$	Doped	26	2.5	3.2	0.22
$Si_{0.63}Ge_{0.37}$	Undoped	44	-	-	-
$Si_{0.51}Ge_{0.49}$	Undoped	51	-	-	-
$Si_{0.80}Ge_{0.20}$ (1834 bulk)	Doped	-	1.4	0.5	0.2
$Si_{0.80}Ge_{0.20}$ (1834 bulk)	Doped	-	1.4	0.5	0.2

In our calculations, the non-ionized impurity scattering has been added to the ionized and acoustic scattering by using the Matthiessen's rule. The sum of ionized carrier density (N_i) and non-ionized impurity concentration (N_n) is the total density of the dopant (phosphorus). The density data obtained from electrical properties of all the samples are listed in Table 3. In heavily phosphorus doped Si bulks, it has been experimentally shown that N_n is larger than N_i, but they are on the same order.[114, 122] The non-ionized impurity has relatively small influence on thermopower, but electrical conductivity may change significantly. This is because electrical conductivity depends on geometrical factors while thermopower doesn't. Let's suppose that there are two different materials, as shown in Figure 18. One of them contains only ionized impurities with a density of N_i (Figure 18a), and the other one has two separate parallel regions

respectively containing ionized impurities with a density of N_i and non-ionized impurities with a density of N_n (Figure 18b). Then, the electrical conductivity of the material 'b' is much smaller than that of material 'a' due to the less electrically conductive (the non-ionized) portion. On the other hand, thermopower values for both 'a' and 'b' are similar since it follows the property of electrically conductive portion.[123, 124] In mathematical equations, any changes in the ionized and non-ionized carrier densities affect the relaxation time (see Eq. (21)). While the relaxation time in the numerator of Eq. (20) strongly influences the electrical conductivity, it appears in both numerator and denominator of Eq. (33) and Eq. (34), suppressing its role in altering thermopower. Therefore, we selected the density of ionized impurities by fitting experimental thermopower data, and then found the density of non-ionized impurities with electrical conductivity data. Then, thermopower was re-calculated with both ionized and non-ionized impurity densities. This iterative step is to confirm thermopower is a weak function of non-ionized impurity density.

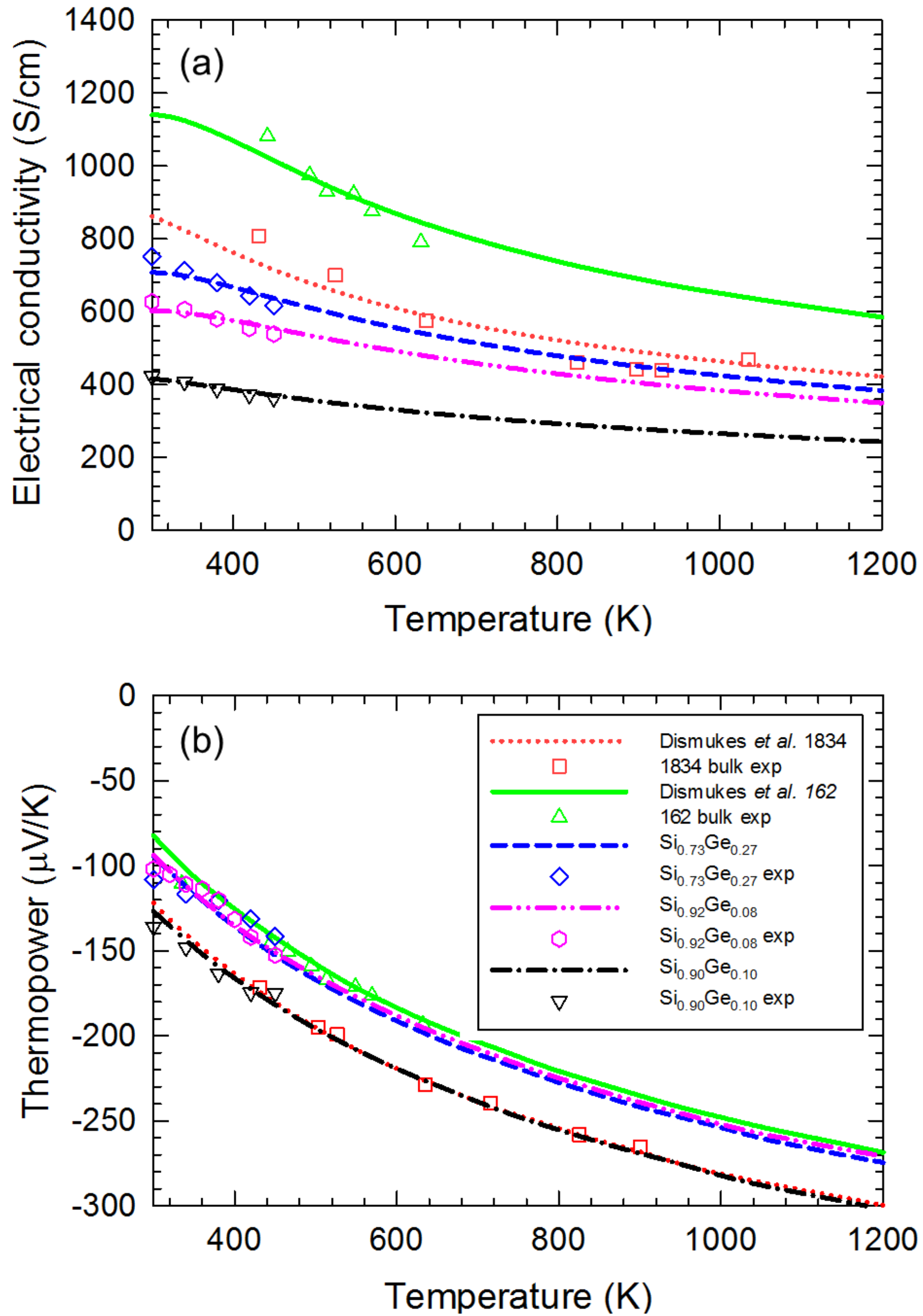

Figure 19. Simulated electrical properties of heavily doped SiGe nanowire with considering non-ionized doped phosphorus.

Figure 19 shows simulation results for bulk materials 1834 and 162 from reference,[125] $Si_{0.92}Ge_{0.08}$, $Si_{0.9}Ge_{0.1}$, and $Si_{0.73}Ge_{0.27}$ nanowires along with experimental data. For both bulk materials and nanowires, our calculated electrical conductivity and thermopower are in good agreement with the experimental data. The ionized and non-ionized impurity densities for nanowire samples are $N_i = 2.5\times10^{20}$ cm^{-3} and $N_n = 4.0\times10^{20}$ cm^{-3} for $Si_{0.92}Ge_{0.08}$; $N_i = 1.7\times10^{20}$ cm^{-3} and $N_n = 4.2\times10^{20}$ cm^{-3} for $Si_{0.9}Ge_{0.1}$; $N_i = 2.5\times10^{20}$ cm^{-3} and $N_n = 3.2\times10^{20}$ cm^{-3} for $Si_{0.73}Ge_{0.27}$. All the ionized and non-ionized dopant densities are on the order of 10^{20} cm^{-3}. While our calculation provides a method of estimating electrical properties of SiGe nanowires, this suggests that the power factor can be further improved by removing non-ionized impurities.

We have also calculated the lattice thermal conductivity of SiGe nanowires with an adjusted cutoff frequency in a modified Callaway model. For heavily doped SiGe bulks, Vining[75] showed experimental data can be calculated by modifying the Callaway model. However, this model is not suitable for calculating nanowire properties since it does not consider the boundary scattering. Moreover, a constant ratio between the normal and Umklapp scattering rate was used. These resulted in much larger thermal conductivities than our experimental data for SiGe nanowires.[126, 127] Morelli *et al.*[89] proposed a modified Callaway model with separate transverse and longitudinal phonon modes with boundary, normal, impurity, and Umklapp scattering mechanisms. This model showed improved estimation results for the lattice thermal conductivity of group IV and group III-V bulk semiconductors. Nevertheless, the Morelli's model could not fit the experimental data of SiGe nanowires properly. Larger discrepancies were observed

for nanowires with smaller diameters (100 nm or smaller for SiGe nanowires). The reason of the mismatch is likely to be from an overestimate of the phonon transmission at high frequencies. Both Vining's and Morelli's model are modified versions of the Callaway model, which uses the linear phonon dispersion (i.e., linear relation between frequency and wavevector) model. Mingo[67] pointed out the linear approximation inadequately overcount the phonon density at high frequencies, compared to that of the real phonon dispersion. In order to obtain good fitting results, Mingo[67] suggested a lower cut-off frequency (ω_C) instead of using the Debye frequency (ω_D) by multiplying an adjusting parameter a (a<1) to ω_D .

$$\omega_C = a\omega_D \tag{54}$$

When a = 0.488 (ω_C = 42THz and ω_D = 86THz), a good agreement for the experimental thermal conductivities of Si nanowires was achieved.

In our model, we separately considered transverse and longitudinal modes (i.e., subscript i).

$$\omega_{C,i} = a\omega_{D,i} \tag{55}$$

Considering of the linear relation between frequency and the speed of sound,

$$\omega_{D,i} = v_i \left(\frac{6\pi^2}{V} \right)^{1/3} \tag{56}$$

where, v_i and V stand for the speed of sound and volume per atom of SiGe. The ratio of the Debye frequency of SiGe ($\omega_{D,i}$) and Si ($\omega_{D,Si,i}$) is expressed as:

$$\frac{\omega_{D,i}}{\omega_{D,Si,i}} = \frac{v_i}{v_{Si,i}} \left(\frac{V_{Si}}{V} \right)^{1/3} \tag{57}$$

Then, we can express the cut off frequency ($\omega_{C,i}$) of SiGe nanowires by using Eq. (57):

$$\omega_{C,i} = a\omega_{D,Si,i} \frac{v_i}{v_{Si,i}} \left(\frac{V_{Si}}{V} \right)^{1/3} \tag{58}$$

Then the adjusted cutoff temperature is described as:

$$\theta_{C,i} = \frac{a\hbar\omega_{D,i}}{k_B} = \frac{a\hbar\omega_{D,Si,i}}{k_B} \frac{v_i}{v_{Si,i}} \left(\frac{V_{Si}}{V} \right)^{1/3} \tag{59}$$

Since the Debye temperature for Si is available, Eq. (59) was re-written as:

$$\theta_{C,i} = a\theta_{D,Si,i} \frac{v_i}{v_{Si,i}} \left(\frac{V_{Si}}{V} \right)^{1/3} \tag{60}$$

$\theta_{C,i}$ is substituted for θ_i in Eq. (37), (38), and (39) to obtain the lattice thermal conductivity.

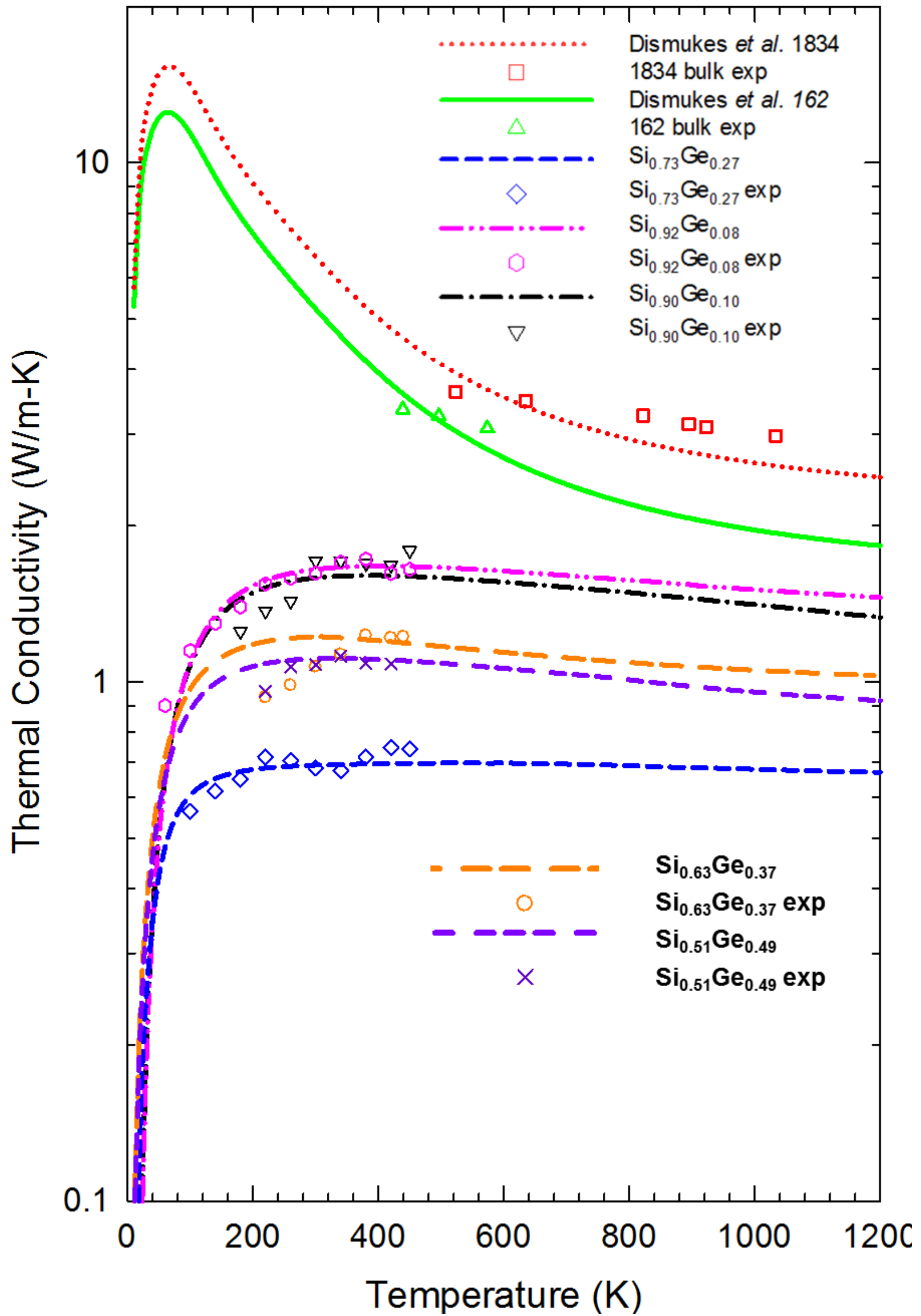

Figure 20. Simulation results of thermal conductivities of SiGe nanowires with different Ge concentration along with two SiGe bulk materials in reference.[49]

With the adjusted Debye temperature, the simulated lattice thermal conductivities of undoped nanowires ($Si_{0.63}Ge_{0.37}$ and $Si_{0.51}Ge_{0.49}$) are plotted in Figure 20 based on our modified model. Multiple phonons scatterings including Phonon-phonon normal scattering (Eq. (43)), phonon-phonon Umklapp scattering (Eq. (45)), phonon-alloy scattering (Eq. (47)) and phonon-boundary scattering (Eq. (49)) are considered for obtaining the phonon relaxation time. Ge concentration and nanowire diameter are only two variables in our model for undoped SiGe nanowires and no fitting parameter is required. The predicted results show a good agreement with the experimental data. It was also noted that even with smaller diameter, thermal conductivity of undoped $Si_{0.63}Ge_{0.37}$ (44 nm) was larger than that of undoped $Si_{0.51}Ge_{0.49}$ (51 nm). It indicates that the alloy scattering became more significant than boundary scattering in small diameter (<100 nm) SiGe nanowires, which was also proved in our previous experimental studies.[71, 102]

For P heavily doped nanowires ($Si_{0.92}Ge_{0.08}$, $Si_{0.90}Ge_{0.10}$ and $Si_{0.73}Ge_{0.27}$), phonon-electron scattering (Eq. (50)) and phosphorus cluster scattering (Eq. (49)) were additionally considered in the simulation, besides of all the phonon scatterings used for undoped nanowires. The density level of dopant P is extremely high in our SiGe nanowires (on the order of 10^{20} cm^{-3}), which makes the influence of P clusters scattering non-negligible for the thermal conductivity simulation. Assuming that the total volume occupied by P is similar regardless of the presence of P clusters, the cluster density and size have the following relation:

$$D_{A,P}V_P = D_{C,P}\frac{4}{3}\pi R_{C,P}^3 \quad (61)$$

where, V_P is the volume per P atom, $R_{C,P}$ is the radius of P cluster, $D_{A,P}$ and $D_{C,P}$ are the number density of P atoms and P cluster, respectively. Note that the clusters were formed into a sphere shape.

The density ($D_{C,P}$) and size ($R_{C,P}$) of phosphorus clusters were determined by fitting the experimental data, but the two parameters are directly connected by Eq.(61) and cannot be arbitrarily selected. For instance, P cluster radius ($R_{C,P}$) cannot be smaller than radius of P atom. On the other hand, the radius cannot be larger than a few nanometers since P clusters were not clearly identified by our previous TEM characterization[71, 102] For phonon scattering, the non-ionized phosphorus was considered as phosphorus-vacancy pair (P^+V^-), also known as E center.[114-116] In this situation, the density of E center should be exactly the same as the density of non-ionized phosphorus (N_n). It was not easy to estimate the size of vacancy, so we assume the E center has the same volume of phosphorus atom. The final density and volume of phosphorus pair in the cluster scattering were considered as non-ionized impurity density (N_n) and volume of single phosphorus atom (V_P), respectively. Since the left part of Eq. (61) ($D_{A,P}V_P$) has certain value, the density ($D_{C,P}$) of cluster can be determined by the cluster radius ($R_{C,P}$).

Table 4. Parameters for the simulation of thermoelectric properties of SiGe nanowires.

Parameters	Values	Reference
$\theta_{Si,L}$	586 K	Ref.30
$\theta_{Si,T}$	240 K	Ref.30
$v_{Si,L}$	8430 m/s	Ref.30
$v_{Si,T}$	5840 m/s	Ref.30
$v_{Ge,L}$	4920 m/s	Ref.30
$v_{Ge,T}$	3540 m/s	Ref.30
$m^*_{Si,e}$	1.08 m_0	Ref.72
$m^*_{Si,h}$	0.56 m_0	Ref.72
$m^*_{Ge,e}$	0.55 m_0	Ref.72
$m^*_{Ge,h}$	0.37 m_0	Ref.72
γ_L	1.1	Ref.30
γ_T	0.6	Ref.30
E	2.94 eV	Ref.14
M_{Si}	4.6637×10^{-26} kg	Ref.14
M_{Ge}	1.206×10^{-25} kg	Ref.14
V_{Si}	2.0024×10^{-29} m^3	Ref.14
V_{Ge}	2.2636×10^{-29} m^3	Ref.14
V_P	2.822×10^{-29} m^3	Ref.14

Finally, the radiuses of the clusters were used as the last fitting parameters to fit the experimental data of heavily doped samples. The details of fitting parameter for the lattice thermal conductivity were shown in Table 4. All the measured thermal conductivities of heavily doped nanowires $Si_{0.92}Ge_{0.08}$, $Si_{0.90}Ge_{0.10}$ and $Si_{0.73}Ge_{0.27}$ can

also be well fitted with reasonable phosphorus cluster sizes at low to medium temperature ranges, as shown in Figure 20. In comparison with $Si_{0.90}Ge_{0.10}$ whose diameter is 45 nm, the thermal conductivity of $Si_{0.92}Ge_{0.08}$ with 97 nm diameter has very similar value, presumably due to the larger concentration density of phosphorus cluster. The thermal conductivity of $Si_{0.73}Ge_{0.27}$ nanowire is much smaller than those of other two heavily doped ones, which is related to strong scattering in all three factors: small diameter, high Ge concentration and dense phosphorus cluster. An estimated result of thermal conductivity at high temperature up to 800 K for each nanowire is also given based on the same model. With the exactly same model, the lattice thermal conductivity of P heavily doped bulk materials 1834 and 162 from the reference[125] are also calculated and have good agreement with experimental data, as shown in Figure 20. The only difference between SiGe bulks and nanowires in our simulation is the diameter limitation of boundary scattering. It clearly indicated that boundary scattering significantly suppress the phonon conduction of SiGe when the diameter limitation becomes nanoscale.

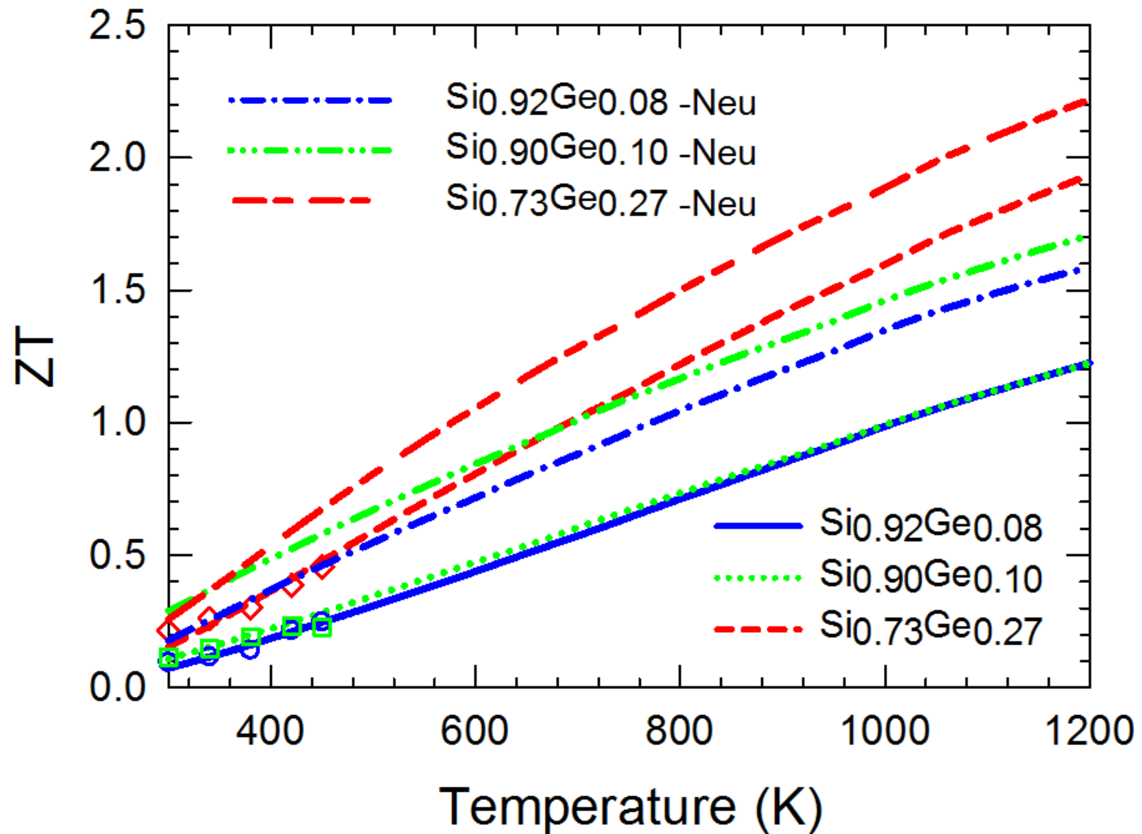

Figure 21. Large improvement of ZT values of SiGe nanowires by removing non-ionized impurities scattering.

Based on all three simulated key thermoelectric properties, a better agreement with the experiment data was finally obtained for *ZT* value, as shown in Figure 21. A high *ZT* value of 1.17 is predicted at 800K for the phosphorus heavily doped n-type $Si_{0.73}Ge_{0.27}$ nanowire, which is about 95% higher than the n-type SiGe bulk used in radioisotope thermoelectric generator (RTG) for NASA space flight mission,[128] and 30% higher than reported *ZT* enhanced nanostructured n-type SiGe bulk alloy.[129] Comparing all three thermoelectric properties of SiGe nanowires with those of SiGe bulk materials,

the power factor of $Si_{0.73}Ge_{0.27}$ nanowire (2.43 $mWm^{-1}K^{-2}$ at 800 K) is even smaller than that of RTG bulk (3.04 $mWm^{-1}K^{-2}$ at 800 K), which implies that the major improvement of *ZT* is contributed from the remarkable reduction of thermal conductivity by enhanced phonon scatterings. If we can synthesize SiGe nanowires with electrical properties similar to those of bulk SiGe, even higher *ZT* values could be reached based on the small thermal conductivity by the boundary limitation. Comparing with RTG SiGe bulk, the impairment in electrical conductivity of our heavily doped SiGe nanowires can be attributed to strong impurity scattering by the non-ionized phosphorus. However, serving as impurity scattering factor for both electron and phonon, the non-ionized phosphorus could reduce the electrical conductivity and thermal conductivity in SiGe nanowire at the same time. It is not clear how the non-ionized phosphorus changes the *ZT* values in Eq. (1) since these two conductivities vary in the same direction. Figure 21 shows the simulated *ZT* values of all three doped SiGe nanowires with and without non-ionized phosphorus impurity scattering. All three samples received large improvement (20–40% at 800 K, 130–220% at 300 K) in *ZT* values when non-ionized impurity scattering was removed. Particularly, an extremely high *ZT* value 1.44 at 800 K could be reached for $Si_{0.73}Ge_{0.27}$ nanowire without non-ionized impurity scattering. This implies that non-ionized phosphorus impurity has more significant influence on electrons than phonons. As a result, the gain on electrical conductivity from removing non-ionized impurity is larger than the jeopardizing on thermal conductivity, which finally leads to an enhanced *ZT* value.

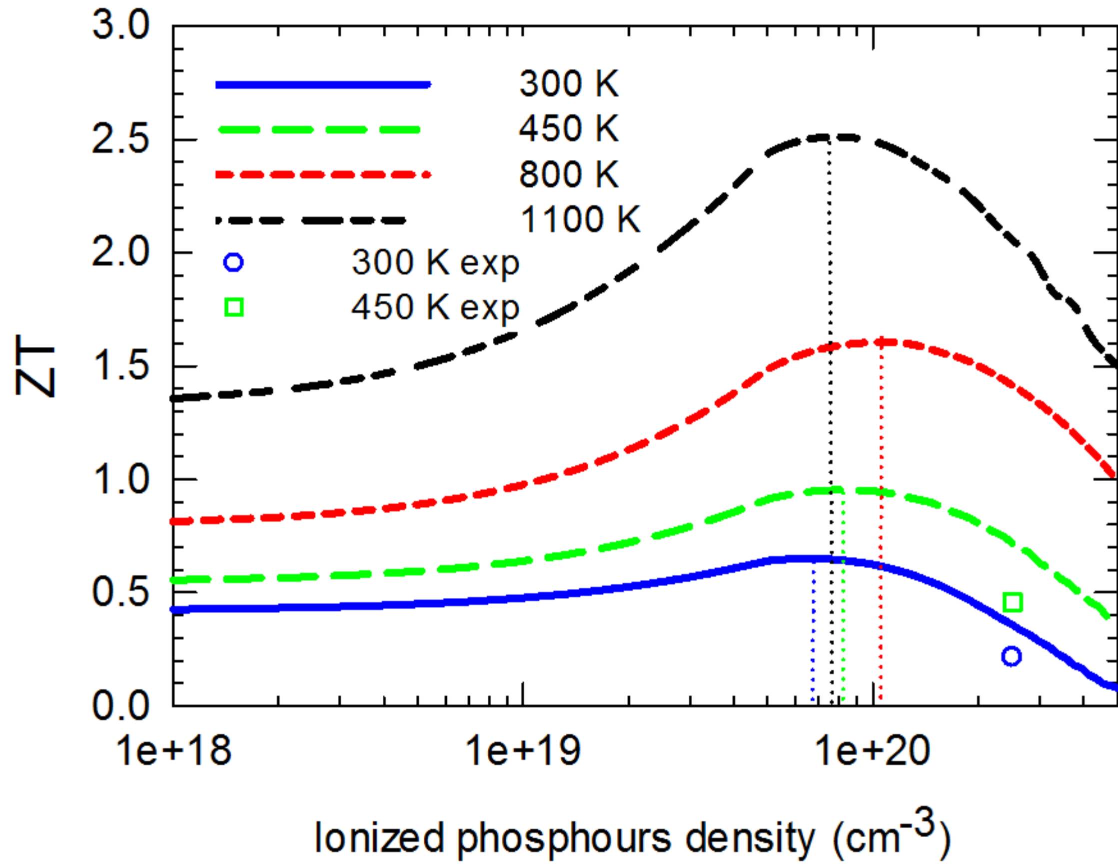

Figure 22. The calculated ZT value of $Si_{0.73}Ge_{0.27}$ nanowire after removing non-ionized impurity as function of ionized donor density. The two points represent the experimental data of $Si_{0.73}Ge_{0.27}$ nanowire with non-ionized phosphorus density of 3.2×10^{20} cm^{-3}.

In the thermoelectric transport study, ionized dopant also plays an important role since it directly affects the electron conductivity, electric thermal conductivity by Wiedemann–Franz Law and also contributes in phonon-electron scattering. In order to reach best thermoelectric efficiency, the dopant concentration of SiGe nanowires should be optimized at different temperature. Figure 22 shows how the calculated *ZT* values of $Si_{0.73}Ge_{0.27}$ nanowire change with ionized phosphorus density at 300 K, 450 K, 800 K

and 1100 K. It should be noted that all the simulation results were calculated without non-ionized phosphorus impurity. At all temperatures, the values of *ZT* keep increasing when dopant concentration density increases from 10^{18} cm^{-3}. After reaching a peak of value, *ZT* values slump quickly at high dopant density (>~10^{20} cm^{-3}). Based on our simulation results, the optimized dopant densities for $Si_{0.73}Ge_{0.27}$ nanowire are around the range of 0.7~1×10^{20} cm^{-3} at 300~1100 K. The optimized ionized donor density slightly increases with temperature, which agrees with the data of SiGe bulk materials.[75] Two experimental *ZT* values of $Si_{0.73}Ge_{0.27}$ nanowire at 300 K and 450 K were also plotted in Figure 22. Comparing with optimized values, there is still plenty of room for thermoelectric efficiency of the SiGe nanowire to improve. 200 % increase of *ZT* value at 300 K and 110 % increase at 450 K from our best experiment values could be expected on $Si_{0.73}Ge_{0.27}$ nanowire with optimized dopant densities. At 800 K, an extremely high *ZT* value ~1.6 is estimated with optimized ionized dopant density 1.06×10^{20} cm^{-3}, which is about 80 % higher than that of reported nanostructured n-type SiGe bulk alloy (~0.9),[129] and 170 % larger than that of the SiGe bulk used in RTG (~0.6).[128] At 1100 K, ZT value of $Si_{0.73}Ge_{0.27}$ nanowire was estimated at ~2.5 with optimized dopant density 7.8×10^{19} cm^{-3}.

CHAPTER IV

OXIDE NANOWIRES FOR THERMOELECTRIC APPLICATION

As thermoelectric materials, oxide nanowires have great advantages comparing to other semiconductors. Oxides are nontoxic, abundantly available, and have high thermal stability and excellent oxidization resistance, making them great candidates for high temperature thermoelectric application. In this chapter, two nanostructured materials, $SrTiO_3$ nanotubes and ZnO nanowires, are successfully synthesized by simple methods. Thermal conductivity of ZnO nanowires with different diameter were characterized from 60 K to 450 K. A significant decrease in thermal conductivity is found from ZnO nanowires of small diameters.

4.1 Synthesis of strontium titanate ($SrTiO_3$) nanotubes

4.1.1 Synthesis of TiO_2 nanotubes

Long aligned arrays of crystalline strontium titanate ($SrTiO_3$) nanotubes were synthesized by using simple low-temperature strontium incorporation process into titanium oxides. The tubular nanostructures are excellent to confine energy carriers that result in extraordinary transport behaviors in strontium titanates so as to develop efficient thermoelectric energy conversion devices. However, synthesizing ternary compounds in the form of one-dimensional nanostructure arrays often involves complicated and/or long reactions that produce disordered cubic-shape particles. Recently, ternary compound nanostructures have been synthesized by using various

methods [130] including a molten-salt or sol-gel method for nanoparticles [131, 132] sol-gel methods for nanorods [133-135], a template method for nanotubes [136], and hydrothermal reactions for several days at relatively high temperatures to obtain nanowires/tubes.[130, 137] These nanostructures may not be suitable for thermoelectric applications due to inappropriate morphology such as cubic-shapes, short wires/tubes (a few hundreds of nanometer long) or/and other byproducts that are difficult to remove from strontium titanates. They are often clumped and dispersed in an arbitrary fashion, which requires a non-trivial assembly process to build practical materials. The synthesis reaction involves a two-step process. First, tube arrays made of amorphous titanium oxides were synthesized by anodizing a titanium foil. Then, the amorphous tubes were converted into crystalline strontium titanates at either 90 or 180 ^{o}C with a beaker or pressure vessel in ambient air environment.

Prior to the anodization, titanium foils (purity 99.5%, ~250 μm thick) were ultrasonically cleaned in ethanol and de-ionized water, respectively. Then, the foil was immersed in a solution that contains 1.8 wt% de-ionized water, 0.3 wt% NH_4F, and 97.9 wt% ethylene glycol for anodization. When DC 60 Volt was applied between a titanium foil (anode) and a stainless steel foil (cathode), an array of nanotubes was formed from outer surface to the center along the foil thickness direction. Typical size of the titanium foil was 20×5 mm^2 and the distance between two foils was ~2 cm. The foils were typically anodized for 24 hours in 100 mL solution, yielding tube arrays with a tube length of 100 μm or longer. Figure 23 shows scanning electron micrographs (SEMs)

and transmission electron micrographs (TEMs) of as-synthesized titanium oxide nanotubes.

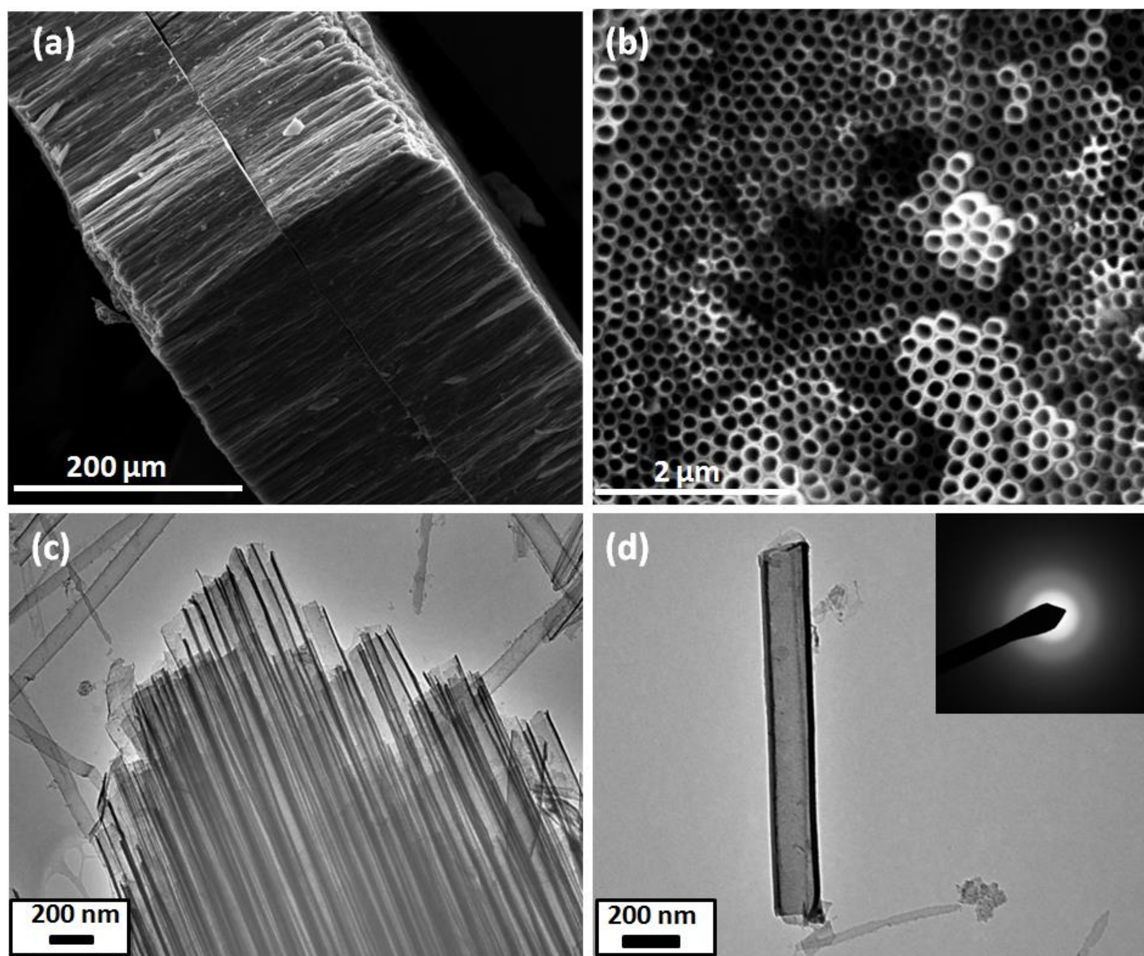

Figure 23. (a) A cross section of a typical titanium oxide nanotube array by anodizing a titanium foil. Titanium oxide tubes were made from the outer surface to the center, creating a barrier layer that makes one of the tube ends closed. (b) An outer surface of the anodized foil shows circular pores from the tube array. Gentle sonication separated the array into (c) a bundle and (d) an individual titanium oxide nanotube. The electron diffraction in the inset shows amorphous structure.

They are well aligned and vertically grown from the foil surface with diameters and length of ~150 nm and ~180 μm (Figure 23a and b). A 0.25-mm thick Ti foil was completely anodized from both surfaces, creating two 180-μm long nanotube layers separated by two thin barrier layers at the center. The volume expansion is due to the introduction of oxygen to titanium, forming amorphous titanium oxides. The diameter and length of the nanotubes can be altered by using different anodization voltage and anodization time.[138, 139] Gentle sonication of samples in an ultrasonic bath separated them into bundles and/or individual tubes for TEM analysis (Figure 23c and d). The inset of Figure 23d indicates the tube has an amorphous structure.

4.1.2 Strontium incorporation processes

The tube array was further processed with various conditions in order to study reactions between strontium and titanium oxide tubes. The key reaction parameters including etching time, pre-treatment of the tubes, reaction temperature, reaction time, and strontium hydroxide ($Sr(OH)_2$) concentration were varied. In typical synthesis, the barrier layer of as-synthesized titanium oxide nanotubes were etched in a mixture of 0.1 M NH_4F and 0.1 M H_2SO_4 in water. Then, the samples were immersed in an ammonia solution (1 M in water) at 90 ^oC for 1 hour. This process is necessary to remove fluorine adsorbed on the surface of the titanium oxide during the anodization and etching process. The nanotubes were annealed in a mixture of 14 mL $Sr(OH)_2$ solution (0.1 M or 0.2 M in water) and 1 mL liquid ammonia (14.8 M in water) at either 90 ^oC in a beaker or 180 ^oC in a pressure vessel for 4 or 12 hours. The pH of the mixture was above 13.

Note that the tube arrays were inserted in a separate bottle in the beaker or pressure vessel so as to avoid direct contact between the array and undissolved $Sr(OH)_2$.

4.1.3 Results and discussion

The amorphous titanium oxides underwent the fluorine desorption and subsequent strontium incorporation processes. Without the fluorine desorbing procedure, water insoluble SrF_2 (solubility: 0.0117g/100mL water at 18 ^oC[140]) was crystallized, as indicated by X-ray diffraction (XRD) in Figure 24a and b from nanotube samples reacted with 0.1 M $Sr(OH)_2$ at 90 or 180 ^oC for 2 hours.

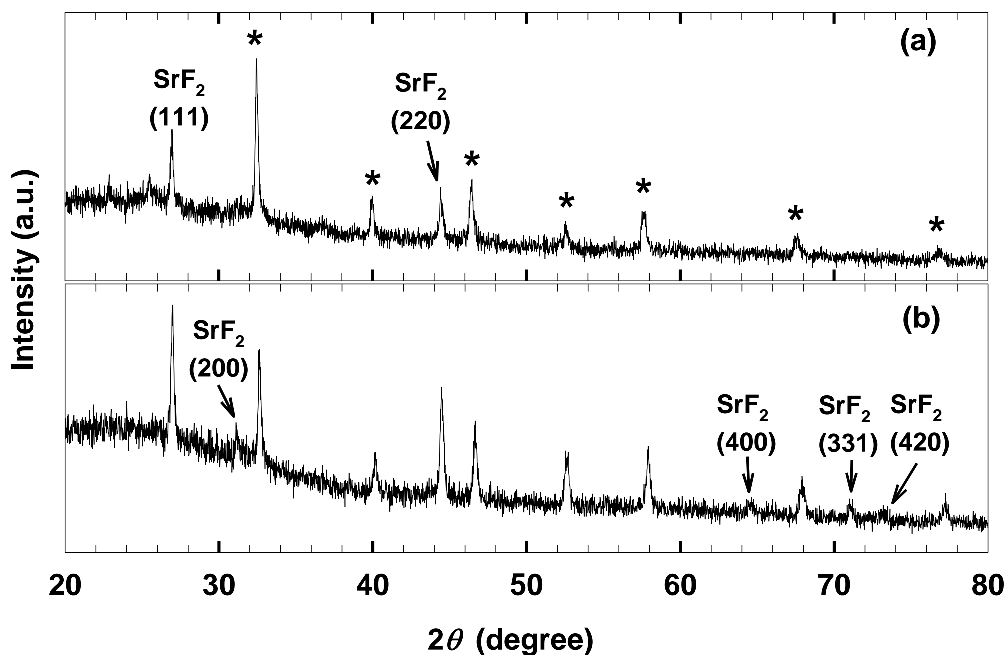

Figure 24. Typical XRD scans of nanotube arrays after a strontium incorporation process with 0.1 M $Sr(OH)_2$ at (a) 90 ^oC and (b) 180 ^oC for 2 hours without a fluorine desorbing process. Fluorine residues on the surface of titanium oxides from the anodization and etching processes are easily crystallized into SrF_2. Peaks indicated by * are from $SrTiO_3$.

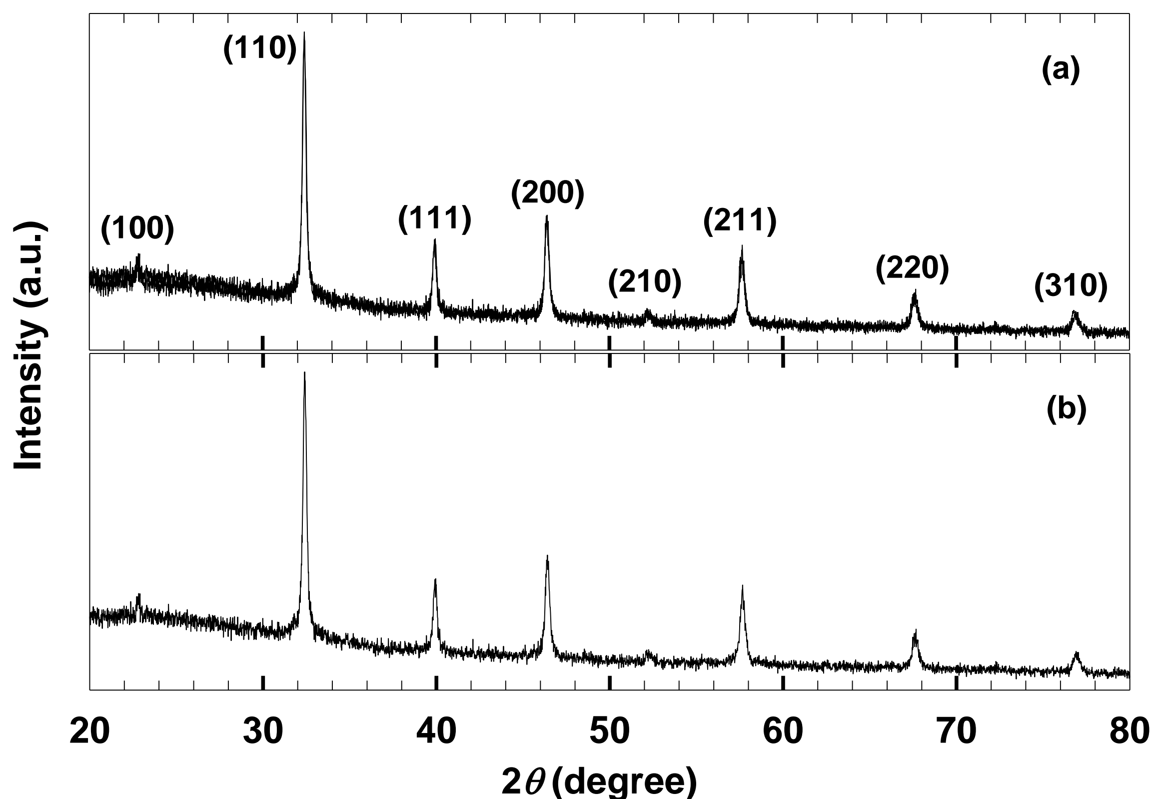

Figure 25. Typical XRD scans of the tube array after a strontium incorporation process with 0.2 M $Sr(OH)_2$ at (a) 90 °C and (b) 180 °C for 4 hours. Crystallographic directions indicate the presence of crystalline $SrTiO_3$.

Conversely, after the fluorine desorbing process, XRD peaks from SrF_2 disappeared, showing the presence of crystalline strontium titanates from both 90 °C (Figure 25a) and 180 °C (Figure 25b) reactions. A typical SEM shown in Figure 26a indicates tube shapes are well maintained after a strontium incorporation process with 0.1 M $Sr(OH)_2$ at 180 °C for 12 hours. It was observed that some portions of the outer surface were covered with a layer of strontium titanates. In order to perform TEM

analysis to identify the structure after reactions, the sample was sonicated in ethanol for a few seconds so as to break it into tiny pieces. In general, the thickness of TEM samples should be ~100 nm or less, which made it impossible to inspect as-synthesized samples without sonication. The ultrasonic power broke the brittle samples into small pieces as shown in Figure 26b.

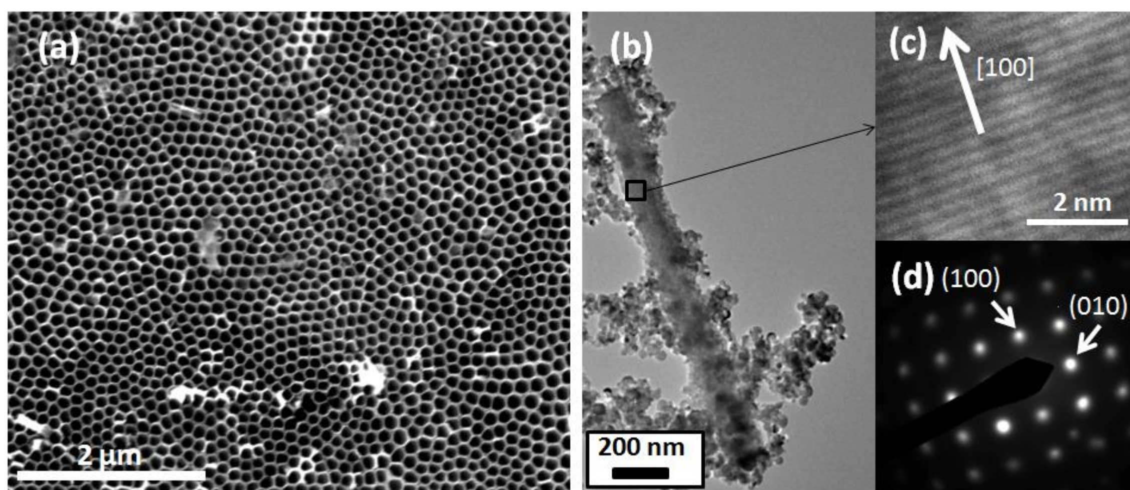

Figure 26. (a) A strontium titanate tube array synthesized with 0.1 M $Sr(OH)_2$ at 180 ^oC for 12 hours. (b) An individual strontium titanate nanostructure synthesized with 0.1 M $Sr(OH)_2$ at 90 ^oC for 4 hours. (c) A high resolution image of a portion (marked with a square in (b)) indicates crystalline strontium titanates with the axis in [100] direction. (d) An electron diffraction image corresponding to the image in (c).

The strontium incorporation increases the density and molar volume of the sample from 2.98 g/cm^3 and 26.80 cm^3/mol (titanium oxide) [141] to 5.13 g/cm^3 and 35.77 cm^3/mol (strontium titanate), respectively[121]. These differences in titanium oxide and strontium titanates may have made wall thickness of the tubes non-uniform after

strontium incorporation. The high resolution TEM image (Figure 26c) and the selected area electron diffraction pattern (Figure 26d) indicate a conversion from amorphous titanium oxides to crystalline strontium titanates with the axis in [100] direction. The spots other than the cubic structure in the SAED are believed to be from the tiny spherical nanoparticles attached to the tube in Figure 26b. The nanoparticles are likely to come from broken pieces after a sonication process.

Table 5. Five different $SrTiO_3$ synthesis conditions to verify strontium incorporation into titanium oxides.

Sample #	Etching time (hr)*	Reaction Temperature (^oC)	Reaction time for Sr incorporation (hr)	$Sr(OH)_2$ concentration
1	-	90	4	0.1 M
2	1.5	90	4	0.1 M
3	3.5	90	4	0.2 M
4	3.5	180	12	0.2 M
5	3.5	180	12	0.2 M

Finally, in order to confirm the conversion into strontium titanates from amorphous titanium oxides, samples were annealed after a strontium incorporation process in an oxygen flow (~20 sccm) at 450 ^oC for 2 hours. Any remaining amorphous oxides will then become anatase TiO_2. This would be due to the barrier layer or/and the deposition of crystallized strontium titanates on the sample surface, which may hinder strontium from being smeared into the pores. For this study, amorphous titanium oxides

were etched in a mixture of 0.1 M NH_4F and 0.1 M H_2SO_4 for 0, 1.5, or 3.5 hours so as to remove the barrier layer prior to a strontium incorporation process, as listed in Table 5.

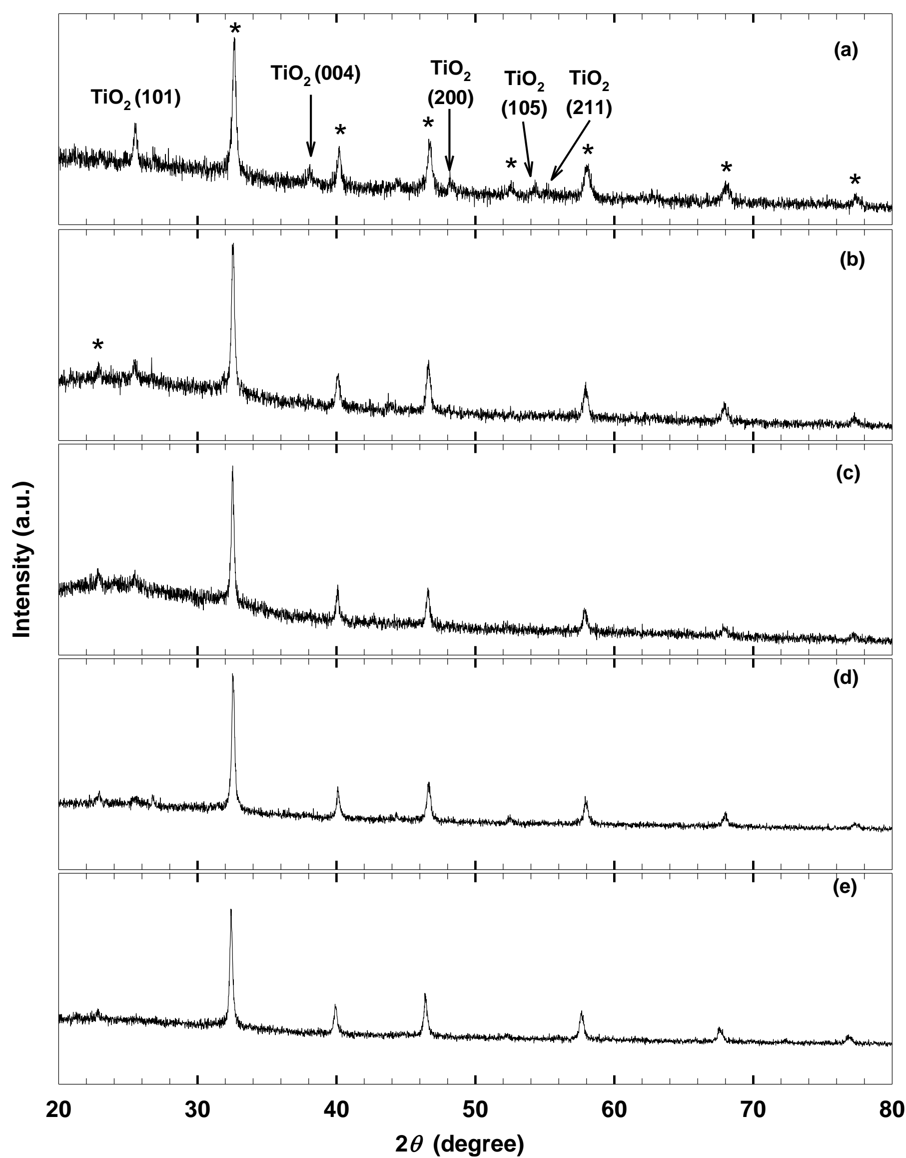

Figure 27. Typical XRD scans of Samples after annealing in an oxygen flow (~20 sccm) at 450 °C for 2 hours. Peaks indicated by * are from $SrTiO_3$.

The etch rate of the sample is estimated to be ~12.5 μm/h. Note that the pore side was etched much faster than the barrier side. Typical barrier layer thickness is several microns and the total thickness of the sample is ~180 μm. When the titanium oxide tubes were reacted with 0.1 M $Sr(OH)_2$ at 90 ^{o}C for 4 hours without etching the barrier layer, the titanium oxide was not fully converted into strontium titanates (Sample 1 in Table 5).

After the oxygen annealing, anatase TiO_2 peaks appeared as shown in Figure 27a. With an etching process for 1.5 hours (Sample 2 in Table 5), XRD peaks corresponding to anatase TiO_2 were suppressed (Figure 27b). On the other hand, an increase of strontium concentration (0.2 M $Sr(OH)_2$) (Sample 3 in Table 5) or a longer reaction (12 hours) with a higher temperature (180 ^{o}C) (Sample 4 in Table 5) did not make significant changes in XRD, leaving tiny anatase TiO_2 peaks (Figure 27c and d). After 3.5 hour etching (Sample 5 in Table 5), anatase peaks were not identified anymore (Figure 27e). This result suggests that amorphous titanates have fully converted into strontium titanates. Note that all samples were crushed into a powder and dispersed on a glass substrate because x-ray scan depths are much shorter than the thickness of the samples.

4.2 Synthesis of zinc oxide (ZnO) nanowires

4.2.1 Synthesis method

One-dimensional (1D) ZnO nanostructures such as nanotubes and nanowires have been synthesized by using several different methods.[31] For example, Zn or ZnO

powders could be evaporated to obtain ZnO nanostructures at relatively high temperature (over ~900 ^{o}C) by using thermal annealing.[142, 143] Aligned ZnO nanowires were grown on sapphire substrate with Au/Sn as a catalyst via a vapor-liquid-solid (VLS) method. [31, 144, 145] A low-temperature hydrothermal method was also used to grow short (2~8 μm) ZnO nanowires.[146] With relatively low synthesis temperatures below ~500 ^{o}C, wire-like structures are typically shorter than several microns or/and require a long reaction time (more than several hours) with a relatively low number density.[147] It is necessary to use high temperatures up to ~1400 ^{o}C[142] to grow long wire-like structures. In addition, tetrapod structures instead of wire shapes were often obtained at temperatures below 1000 ^{o}C. There have been several papers regarding the growth mechanisms of these nanostructures but they do not clearly provide the mechanisms with experimental results.[148-152] We present a simple method that facilitates long and straight single-crystalline ZnO nanowires growths from $ZnCl_2$-coated Zn foils in oxygen environment by using simple thermal annealing processes. With relatively low reaction temperatures (410 and 700 ^{o}C), nanowires whose lengths and diameters are up to ~50 μm and 10~100 nm were obtained. We found that ZnO seeds created from $ZnCl_2$ played an important role in facilitating the ZnO nanowire growth via self-catalytic reactions. Systematic studies by altering critical synthesis factors that determine shape, length, diameter, and density of the nanowires were performed in order to unveil the growth mechanisms. We also compared the nanowires synthesized from Zn foils with tetrapod ZnO nanostructures synthesized from Zn powders at various temperatures.

Before annealing process, Zinc foils (Sigma-Aldrich, purity 99.9 %) were diced into pieces (~1.5 cm×1.5 cm×0.2 mm), and then ultrasonically cleaned in acetone, isopropanol, and deionized (DI) water, respectively. A catalyst solution was prepared by dissolving $ZnCl_2$ (Fisher Scientific, purity 97.8 %) in DI water with a concentration of 5 mM. Then, the solution was spin coated several times at 1500 rpm for 20 s. The spin-coating process uniformly distributes tiny $ZnCl_2$ particles on the foil surface, serving seeds for growing nanowires. In addition, Zn powders (Fisher Scientific, purity 99.3 %) were also used to grow ZnO nanostructures without further treatments.

The samples were placed in a quartz or an alumina boat and inserted at the center of a 22-mm inner diameter quartz tube. Prior to heating a tube furnace (Lindberg/Blue M), ~50 sccm O_2 was flowed for 1 min in order to remove air or any residues that might be present in the tube. Subsequently, the furnace was heated up to the target annealing temperatures (see Table 6) at a rate of ~85 ^{o}C/min with a continuous ~5 sccm O_2 flow throughout the entire synthesis process. The samples grown by using the synthesis condition 8, 9, 10, and 11 were obtained at the same time while other conditions were experimented separately. The synthesis temperatures at different locations of the furnace tube were calibrated by using a K-type thermocouple. The temperature was 850 °C at the heating center (Condition 8) and ~800 °C in the area between 3 and 4 cm away from the center of the heating zone (Condition 9). The temperature dropped to ~700 and ~500 ^{o}C at the locations that are respectively 6 cm (Condition 10) and 10 cm (Condition 11) away from the center of the heating zone. At the end of the annealing, the furnace was

naturally cooled at a rate of approximately 10 ^{o}C/min above ~200 ^{o}C and approximately 1 ^{o}C/min below ~200 ^{o}C.[41, 42]

Table 6. Twelve different synthesis conditions to obtain ZnO nanostructures with Zn foils or Zn powders. $ZnCl_2$ was dissolved in water and spin-coated on the selected foils.

Synthesis condition	Annealing Temperature (^{o}C)	Annealing Time (min)	Zn source	$ZnCl_2$
1	410	120	foil	spin coating
2	410	120	foil	-
3	700	60	foil	spin coating
4	700	60	foil	-
5	850	60	foil	spin coating
6	700	10	foil	spin coating
7	700	30	foil	spin coating
8	850	30	powder	-
9	800	30	powder	-
10	700	30	powder	-
11	500	30	powder	-
12	500	5	-	spin coating

4.2.2 Properties characterization

ZnO nanowires were successfully synthesized at 410 ^oC, 700 ^oC, and 850 ^oC (synthesis condition 1, 3, and 5 in Table 6) on the Zn foils coated with $ZnCl_2$ as respectively shown in Figure 28a, b, and c. Prior to the annealing process, the Zn foils were smooth and flat. After the annealing process, the surface of the Zn foils became rough and white. It was observed that the length and diameter of the synthesized ZnO nanowires were increasing as the reaction temperature was raised. Nanowires synthesized at 410 ^oC are relatively short and small (~5 μm in length (L), ~50 nm in diameter (D)) compared to the nanowires synthesized at 700 ^oC (L~50 μm, D~100 nm) and 850 ^oC (L>100 μm, D~1 μm). The growth rates are high, which are estimated to be ~800 and ~1700 nm/min for 700 and 850 ^oC, respectively. The ZnO nanowires synthesized at 850 ^oC, which is close to the boiling point of Zinc 907 ^oC[153], have rough surfaces as shown in Figure 28c. On the other hand, when Zn foils without the $ZnCl_2$ coating were annealed at 410 ^oC or 700 ^oC, sparse and very short (~1 μm) nanowires (Figure. 28d, 410 ^oC) or thick and short nanorods (Figure. 28e, 700 ^oC) were observed.

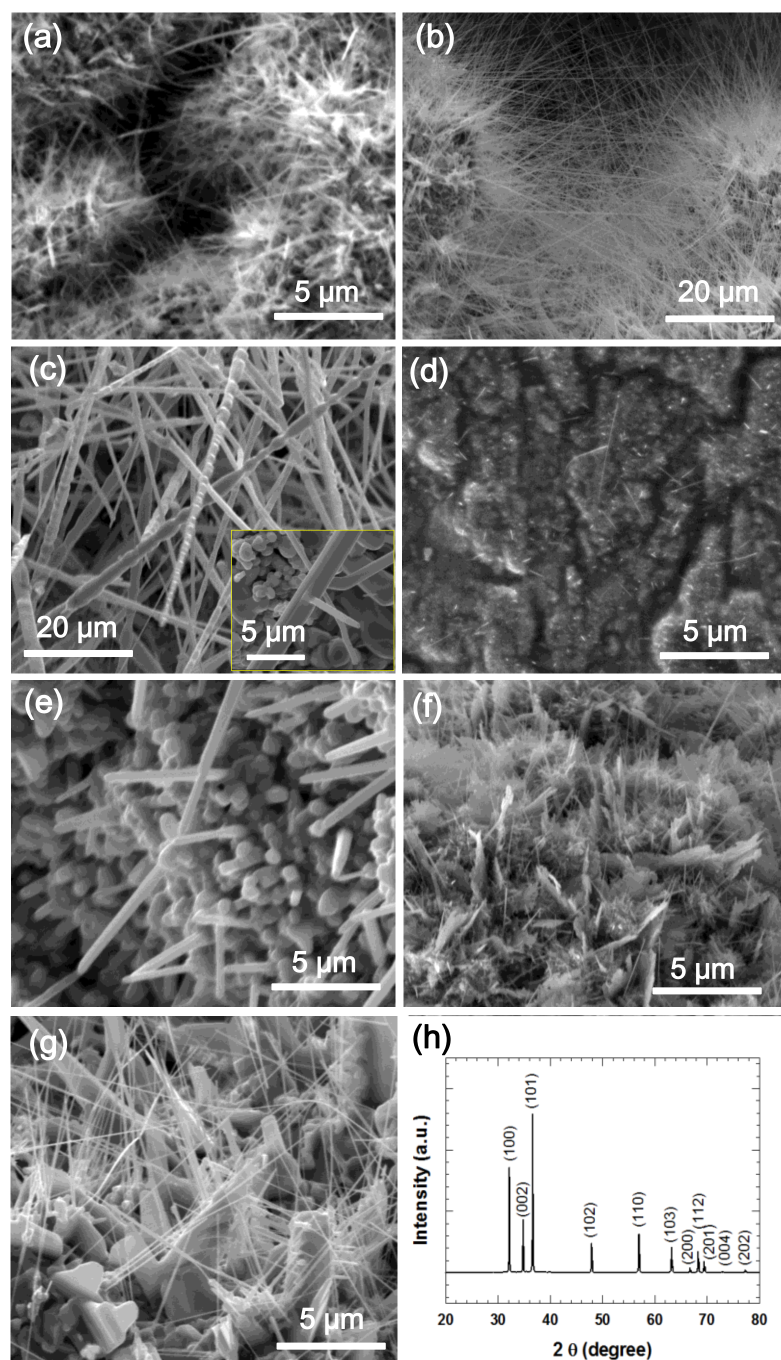

Figure 28. Zn foils with $ZnCl_2$ coating after thermal annealing at 410 ^oC for 120 min (a), 700 ^oC for 60 min (b), 850 ^oC for 30 min (c), 700 ^oC for 10 min (f), and 700 ^oC for 30 min (g). Zn foils without $ZnCl_2$ after thermal annealing at 410 ^oC for 120 min (d) and 700 ^oC for 60 min (e). (h) A typical XRD pattern from the sample synthesized by thermal annealing at 700 ^oC for 60 min (synthesis condition 3 in Table 6).

Without using $ZnCl_2$, dense nanowires with long lengths and small diameters have not been obtained. This indicates that $ZnCl_2$ plays a crucial role in the ZnO nanowire growths. A suggested reaction is described as follows. The spin coating process distributes tiny $ZnCl_2$ particles on the foil surface. Upon heating, $ZnCl_2$ decomposes into ZnO and gas-phase Cl_2 above ~230 ^{o}C.[154]

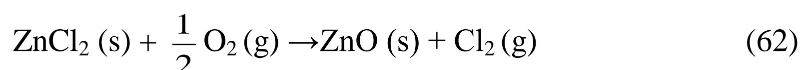

$$ZnCl_2\,(s) + \frac{1}{2}O_2\,(g) \rightarrow ZnO\,(s) + Cl_2\,(g) \qquad (62)$$

The gas-phase Cl_2 is removed by O_2 flow during the reaction process. Then, ZnO particles are deposited on the foil surface, serving seeds to facilitate nanowire growths. The density of the nanowires for $ZnCl_2$-coated samples was high at the edge compared to the center of the foils. This also confirms the role of $ZnCl_2$ since $ZnCl_2$ concentration is relatively higher at the edge due to the centrifugal force and the surface tension of the aqueous $ZnCl_2$ solution.

The influence of the reaction time on the nanowire growth was also studied by varying the reaction time from 60 min (synthesis condition 3) to 10 and 30 min (synthesis condition 6 and 7) at the annealing temperature of 700 ^{o}C. After the 10-min annealing at 700 ^{o}C (Figure 28f), a few micron long leaf-like nanostructures and nanowires were observed. With the longer reaction time, 30 min (Figure 28g), longer nanowires and sheet structures were obtained.

XRD results of nanostructures prepared by using the synthesis condition 1 in Table 6 were shown in Figure 28h, which match the wurtzite structure of ZnO with

lattice constants of a = 0.324 nm and c = 0.519 nm. Any chlorine-containing compounds including $ZnCl_2$, Zn or other impurities were not detected.

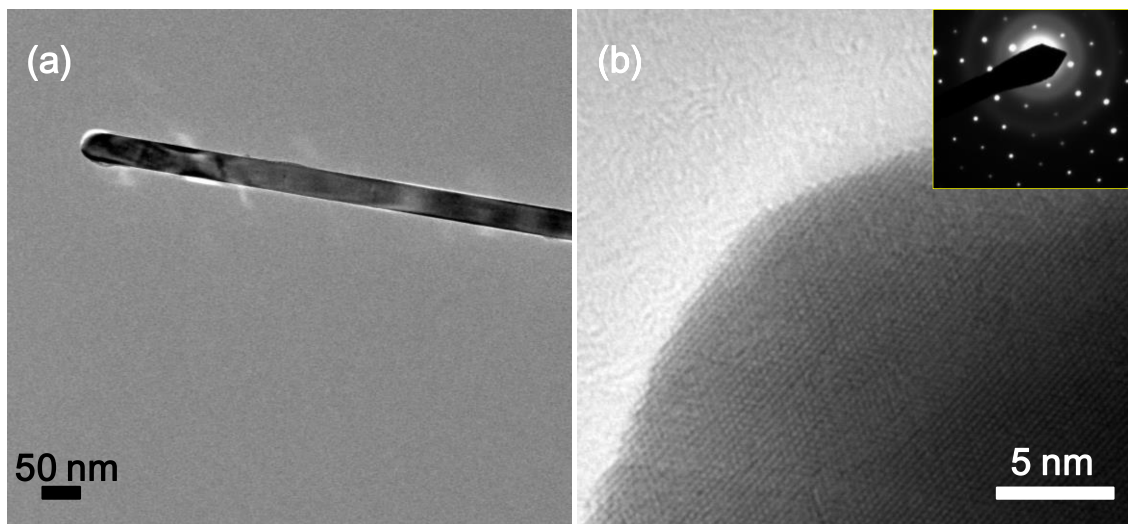

Figure 29. (a) A ZnO nanowire synthesized by thermal annealing at 700 ^{o}C for 60 min (synthesis condition 3 in Table 6). (b) A high resolution TEM image that shows lattice patterns with a SAED in the inset.

Figure 29 shows TEM images with a selected area electron diffraction (SAED) pattern of an individual ZnO nanowire synthesized by using the condition 3 in Table 6. The growth direction of the particular nanowire is [11-20], which is one of common growth directions for wire-shape ZnO nanostructures.[147, 155] It is also possible that we have ZnO nanowires with other growth directions, [0001] and [01-10], which are commonly observed from ZnO nanowires and nanobelts.[31, 156]

4.2.3 Results and discussion

In order to study the nanowire growth mechanism with $ZnCl_2$, SiO_2-grown silicon and amorphous quartz wafer pieces coated with $ZnCl_2$ were annealed for 5 min at 500 ^oC. The short reaction is to identify if the $ZnCl_2$ becomes seeds to facilitate the nanowire growths. We used two different substrates, but the both reactions occurred on SiO_2. This is because the quartz has a severe charging effect in a SEM, as opposed to less charging from the Si substrate. In addition, the atomically flat surface of the Si wafer is ideal for clearly observing the seeds. On the other hand, the quartz do not show XRD peaks whereas the crystalline Si wafer has a very large XRD intensity, which makes a XRD scan with a small amount of powder samples difficult.

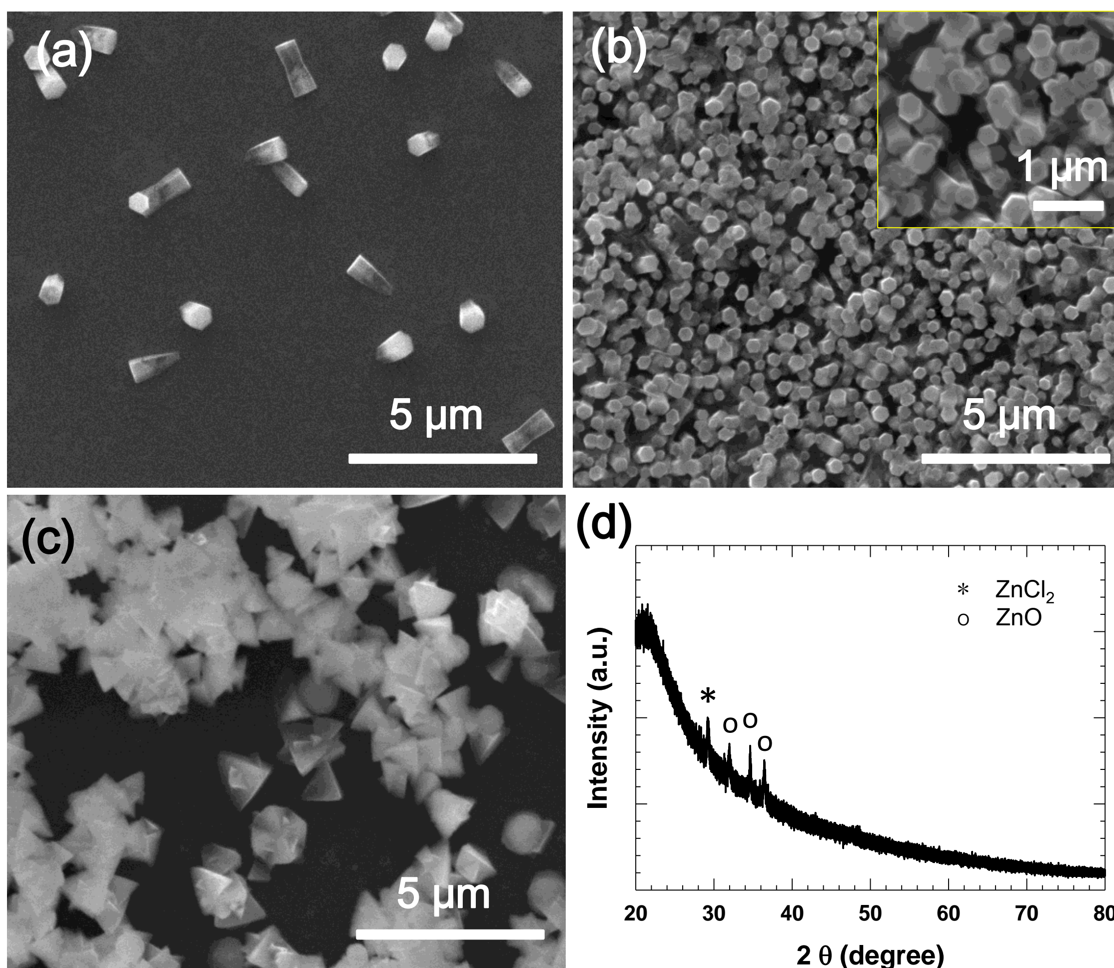

Figure 30. ZnO nanostructures on a Si wafer coated with $ZnCl_2$ after thermal annealing at 500 ^oC for 5 min (a) near the center with low density ZnO and (b) near the edge with high density ZnO. (c) Unreacted $ZnCl_2$ particles showing a tetragonal structure. (d) A typical XRD pattern of $ZnCl_2$ on a quartz wafer after thermal annealing at 500 ^oC for 5 min.

The concentration of the $ZnCl_2$ solution and the coating method are the same as those used on the Zn foil. Figure 30a, b, and c show SEM images of different locations on the Si piece after the annealing. Near the center of the sample (Figure 30a), low density nanorods with hexagonal cross-sections were observed, presumably due to the low density of $ZnCl_2$ near the center after the spin coating process. Near the edge where

the density is high, dense nanorods pushed each other, making them vertically erected (Figure 30b). Additionally, residual tetragonal $ZnCl_2$ particles were also found on the Si piece (Figure 30c), indicating the wires were grown from the particles by the reaction (62). The XRD data of the sample on the quartz wafer (Figure 30d) confirmed the presence of both tetragonal $ZnCl_2$ and hexagonal ZnO.

Zinc powders were also annealed in 5-sccm oxygen flow at four different temperatures with the synthesis conditions 8 (850 ^{o}C– Figure 31a), 9 (800 ^{o}C– Figure 31b), 10 (700 ^{o}C– Figure 31c), and 11 (500 ^{o}C– Figure 31d) in Table 6. With the synthesis temperature, 700 ^{o}C or higher, tetrapod nanostructures were obtained. At 850 ^{o}C growth temperature, a large amount of sheet structures were also observed (Figure 31a). It was reported that the tetrapods have the zinc blend structure for the center and the hexagonal structure for the legs.[157] Nevertheless, the reaction mechanism for creating the morphology is still unclear. The sample annealed at ~800 ^{o}C (Figure 31b) shows tetrapod nanostructures whose legs are tapered while the small tetrapods grown at ~700 ^{o}C (Figure 31c) have legs with dumbbell-like shapes. On the other hand, Figure 31d shows no tetrapod nanostructures but short nanorods grew out of the surface of a spherical Zn powder after the reaction at 500 ^{o}C. After the reaction at 500 ^{o}C, most of the powders remained dark rather than white, which indicates the reaction temperature is too low to have ZnO.

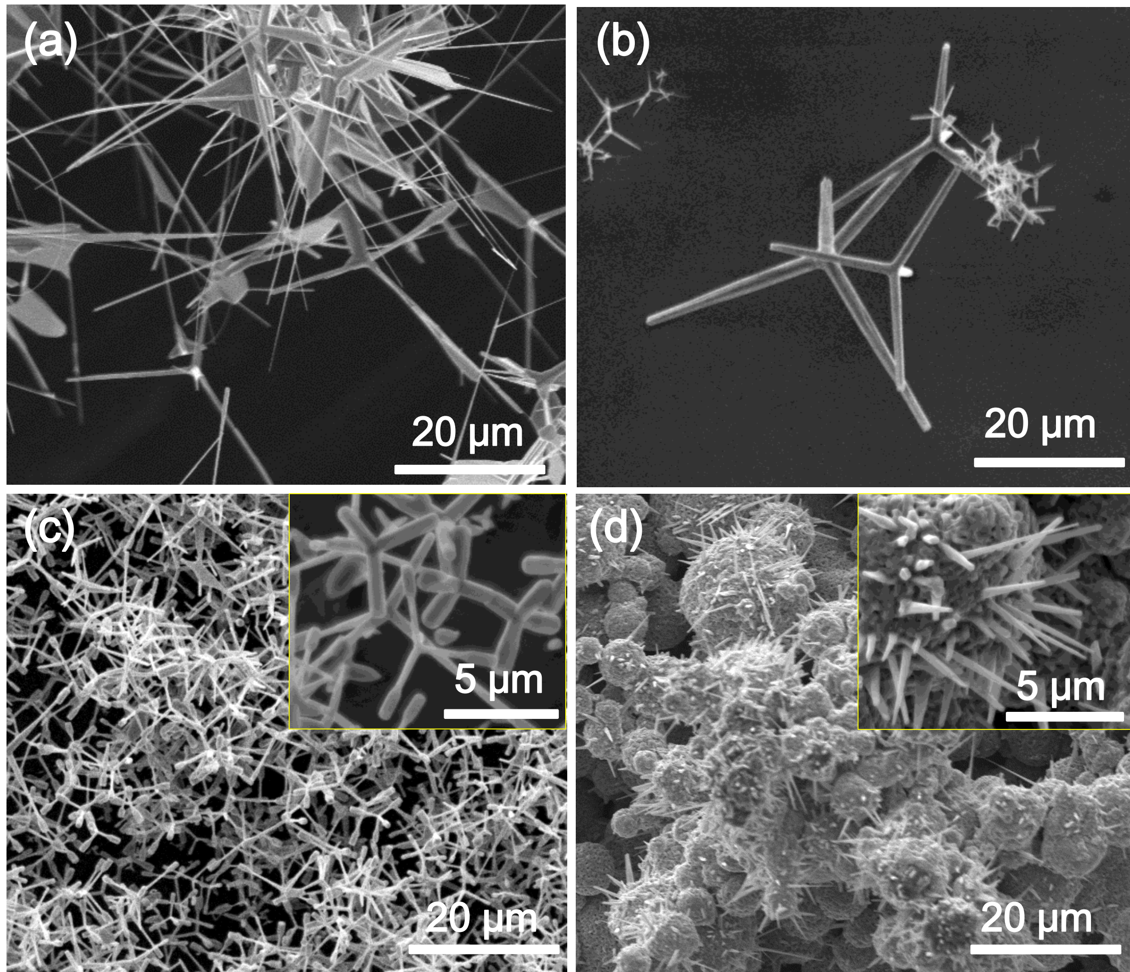

Figure 31. ZnO nanostructures from Zn powders after thermal annealing at (a) 850 ^{o}C, (b) 800 ^{o}C, (c) 700 ^{o}C, and (d) 500 ^{o}C for 30 min.

The experimental results show that the morphology of Zn even with the same thermal annealing method creates different ZnO morphologies – nanowires with foil substrates and tetrapods with powders. Here, we believe different growth mechanisms are responsible for the different morphologies. Our nanowires on the Zn foil with $ZnCl_2$ at 410 ^{o}C (Figure 28a) were grown dominantly by a self-catalytic reaction.[148, 158] Upon heating above the melting point of $ZnCl_2$ (292 ^{o}C[159]), ZnO seeds can be created as a

result of the reaction (1) (e.g., see Figure 30a and b). Subsequently, when the temperature reaches the melting point of Zn (420 ^{o}C[153]), oxygen can be diffused into liquid-phase Zn, forming ZnO at the interface between the liquid Zn and ZnO seeds. Since ZnO grows along the preferentially favorable direction, ZnO becomes a wire shape. The ZnO seeds become self-catalytic to facilitate this reaction. When we used the same reaction temperature and time with only Zn foils (no $ZnCl_2$), the growth rate was substantially suppressed as shown in Figure 28d. We believe that this is due to the lack of the selective localized oxidation sites from which continuous Zn oxidation occurs to form wire shape structures. Without such selective sites, the whole Zn surface is likely to be evenly oxidized, resulting in continuous oxide films.

When the temperature was raised to 700 ^{o}C, long nanowires were synthesized on the $ZnCl_2$-coated foil (Figure 28b) as opposed to short nanorods with larger diameters from the sample without $ZnCl_2$ (Figure 28e). With shorter reaction times (Figure 28f and g), the length of the nanowires became shorter but the diameters were kept to be similar. This indicates the catalytic reaction is dominant since other growth reactions suggested in literatures are likely to make the diameter larger with longer reactions. For instance, a growth by Zn diffusion delivers Zn from the root to the tip of nanowires. Due to the slow diffusion coefficient of Zn in crystalline ZnO (10^{-16} cm^2/s at 700 ^{o}C[160], which provides the diffusion length of 1~10 nm over the 30-min reaction time), it is necessary to have a faster (a few order of magnitude) diffusion through surfaces than that through crystalline ZnO.[161, 162] Grain boundaries and defects could also be passages for a high rate diffusion. If this is the case in our experiment, it is likely that the diameter becomes noticeably

larger since oxygen can be combined with Zn along the stem of the nanowires before diffused Zn reaches the tip.

With the higher temperature reaction at 850 ^{o}C (Figure 28c), large diameters, ~1 μm were obtained. We also noticed irregular wire surfaces and branched wires, indicating Zn was also externally delivered to the reaction sites (called a vapor-solid reaction). Due to the high reaction temperature close to the boiling point of Zn (907 ^{o}C [153]), Zn is vaporized and converted into ZnO on the surface of the nanowires in the oxygen environment. Simultaneous reactions (both self-catalytic and vapor-solid reactions) would have increased the reaction rate, resulting in long (~100 μm) wires.

On the other hand, the same reaction temperature (850 ^{o}C) with Zn powders instead of foils produced tetrapod and sheet structures. Since powders have larger surface area than foils, Zn powders can be easily vaporized at a temperature close to the boiling point. Then, the Zn vapor is likely to condense into ZnO in the oxygen flow (i.e., vapor-solid reaction). Here, the condensed ZnO has the zinc-blend structure from which thermodynamically preferred hexagonal wire-shape structure ZnO were grown, along the four different directions. We believe that the tetrapods shown after 850 and 800 ^{o}C reactions (Figure 31a and b) were not synthesized via liquid-phase Zn diffusion since could not find tetrapods whose centers are bigger than the diameter of the legs. The small and big tetrapods, shown in Fig. 4b, have very similar shapes, indicating that Zn was externally delivered to the reaction sites rather than supplied from the center. When the reaction temperature was lowered to 700 ^{o}C, smaller tetrapods with only a few micron long legs were observed (Figure 31c), presumably due to a reduced amount of

vapor-phase Zn. Further decrease of the reaction temperature to 500 ^{o}C, which is too low to generate vapor-phase Zn, resulted in only rod-shape structures from the powders.

4.3 Thermal conductivity investigation of ZnO nanowire at low temperature range

4.3.1 Sample preparation

As-synthesized ZnO nanowires is dispersed in 200 proof ethanol (Koptec) by ultra-sonication for a few seconds. Then, the nanowire suspension was dropped on a micro-device for measuring thermal conductivity of the nanowires. After ethanol was dried, nanowires were often bridged between two suspended membranes of the micro-device. In order to improve thermal contacts between nanowires and platinum electrodes, nanowires were annealed in vacuum chamber at 600 ^{o}C with ramping rate 2 ^{o}C/min. Right after the temperature reached 600 ^{o}C, the vacuum chamber was naturally cooled down to room temperature. The vacuum pressure was maintained at approximately 10^{-7} torr through a turbo pump in conjunction with a mechanical pump. After the annealing process, the micro-device contains bridged nanowire was attached to chip carrier by using silver paint. Then, the Pt pads of the micro device were wire-bonded to the Au pads on the chip carrier with aluminum wires by wire-bonder (Kulicke & Soffa 4500). Figure 32 shows a SEM images of one ZnO nanowire bridged on suspended membranes of micro-device. The inset show high magnification images for the center of the nanowire.

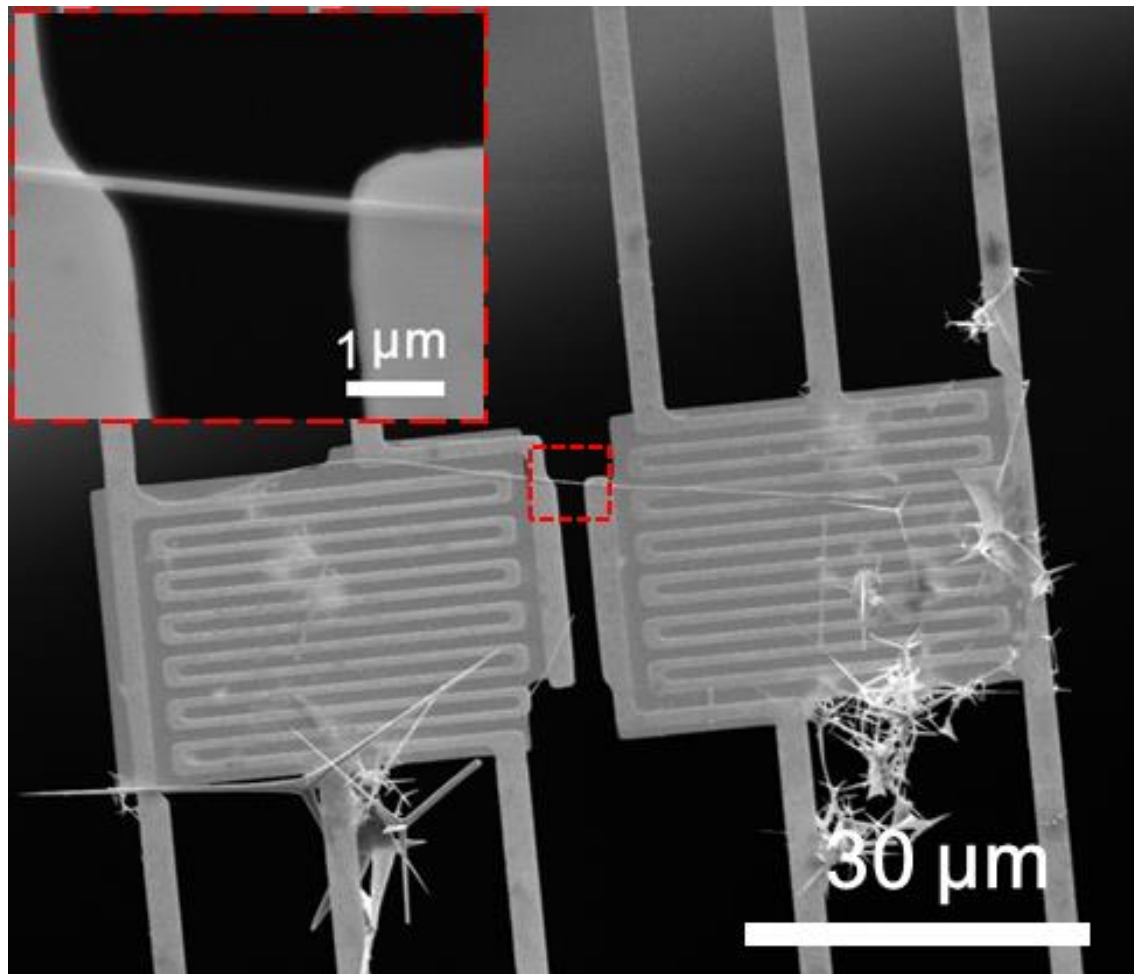

Figure 32. A typical SEM image of ZnO nanowire bridged on platinum electrodes of micro-device; the inset is a high magnification image of the bridged nanowire.

4.3.2 Results and discussion

Thermal conductivities measurement of ZnO nanowire were carried out in the low temperature cryostat at the temperature range of 60 ~ 450 K. The diameters range of measured ZnO nanowires are from 70 nm to over 300 nm. Figure 33 shows the temperature dependence of the thermal conductivity of ZnO nanowires with different diameters along with data of pure ZnO bulk and refined nanostructured ZnO bulk. All

the experimentally measured thermal conductivities of ZnO nanowire keep increasing at all temperature range of 60 K ~ 450 K. It was observed that the thermal conductivity of ZnO nanowire decrease with decreasing nanowire, which agrees with the previous results of SiGe nanowire study. The strong diameter dependence of thermal conductivity suggests that phonon-boundary scattering is dominant in thermal transport in ZnO nanowire. The lowest thermal conductivity of ZnO nanowires was measured to be ~1.4 W/m-K at 300K, which is ~25 times smaller than that of bulk ZnO (~40 W/m-K) and 2~5 times smaller than that of ZnO nanostructured bulk. Hence it could be expected to receive even further reduction on thermal conductivity and higher thermoelectric efficiency due to stronger phonon scatterings from size effect, when smaller one-dimensional nanostructures are employed. Moreover, when Al was doped into ZnO nanowires, impurity-phonon scattering by the aluminum atoms could further reduce the thermal conductivity. A greatly enhanced thermoelectric figure of merit can be expected as a result of the thermal conductivity deduction and the retaining bulk like thermopower and electrical conductivity.

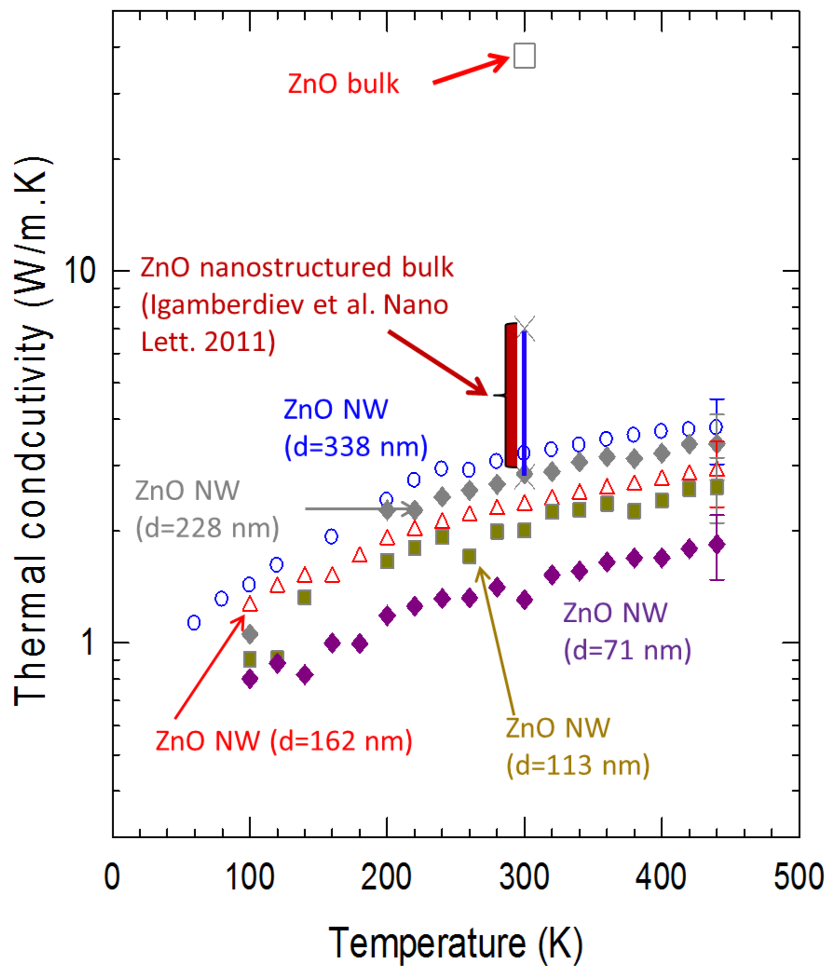

Figure 33. The thermal conductivity of ZnO nanowires with different diameters. The experimentally results are plotted together with previously reported ZnO nanostructured bulk and also ZnO bulk.

CHAPTER V

THERMAL CONDUCTIVITY INVESTIGATION OF NANOWIRE AT HIGH TEMPERATURE RANGE

While high thermoelectric efficiency (ZT value) of SiGe nanowire was expected to be achieved at high temperature based on the simulation results in Chapter 3, ZnO nanowires were also reported as promising high figure of merit candidates at high temperature. Nevertheless, the measurement of thermoelectric properties of nanostructured materials cannot be performed in conventional system, whose highest temperature was typically limited by the cryostat at 300 K or 450 K. In order to test thermoelectric properties at temperature larger than 450 K, a new temperature vacuum system was required. In this chapter, a high temperature vacuum system was designed and built from scratch and some preliminary thermal conductivity results of ZnO nanowires at high temperature were presented and discussed.

5.1 High temperature setup development

5.1.1 Parameters design

The overarching design goal is to create a high temperature vacuum system that could provide stable thermal environment for thermoelectric properties measurement of nanostructured materials at temperature range of 300 K to 800 K. Due to the great differences between low temperature cryostat and high temperature system, all the

parameters of the vacuum system that would satisfy the goal were carefully defined and discussed here.

Vacuum system

The main vacuum chamber was composed of two separate vacuum parts, cycling chamber and sample chamber. The cycling chamber was a customized Janis continuous flow cryostat (DT-3284), which was originally designed for low temperature with helium reservoir. A copper pipe was inserted into the original helium reservoir as the cooling water line. The cycling chamber also contains two military sockets for the connection of electrical signals, powers and thermocouples. The sample chamber was originally a vacuum pipe with inner diameter of 6 inch. One side of the pipe was blocked by welding and another side was designed and modified to be able to attach to the cycling chamber. After the modification, the cycling chamber and sample chamber can be attached together with Buna-N O-ring in-between and provide a perfect whole vacuum chamber. Figure 34 shows the two vacuum chambers connected together after modification. A mechanical pump (Edwards 12) was attached to the vacuum chamber and the pressure within the chamber was maintained at approximately 1×10^{-2} torr during the measurement.

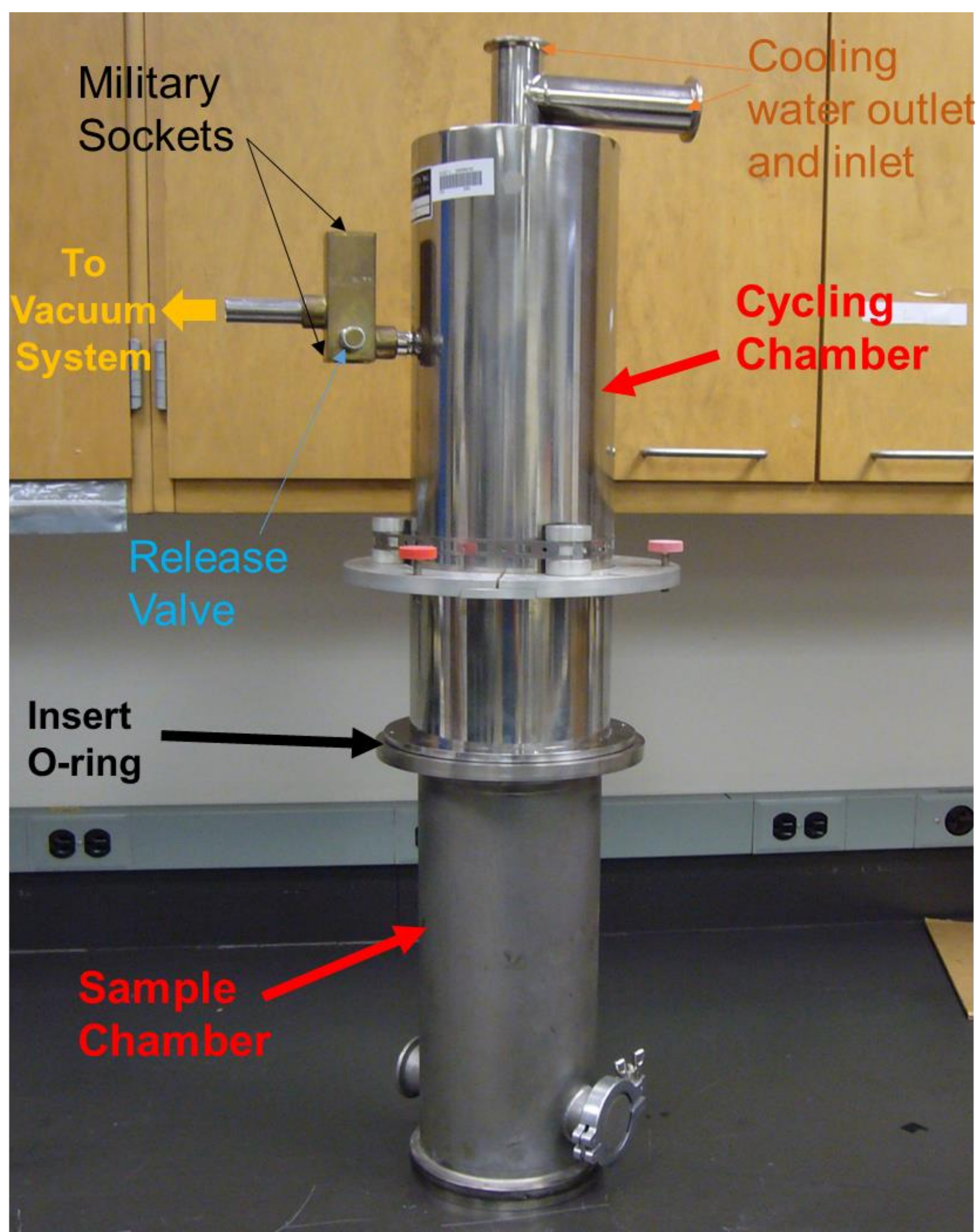

Figure 34. Two major vacuum chambers were connected together after necessary modification.

Cold finger

The sample holder (also called "cold finger") was carefully designed and manufactured based on the structure of cycling chamber and also the heating, cooling power of system. There are four stages in the sample holder: the 1st stage was designed based on the connection shape of the cycling chamber and was made of aluminum to reduce the weight; the 2nd stage was designed as the major conduction part and made of stainless steel due to its lower thermal conductivity; the 3rd stage was heater stage with a 25 ohm cartridge heater inserted inside and was made of copper for high thermal conductivity; the 4th stage was the chip carrier holder and was also made of copper. The original design drawing by SolidWorks and the final real fabricated "cold finger" are shown in Figure 35.

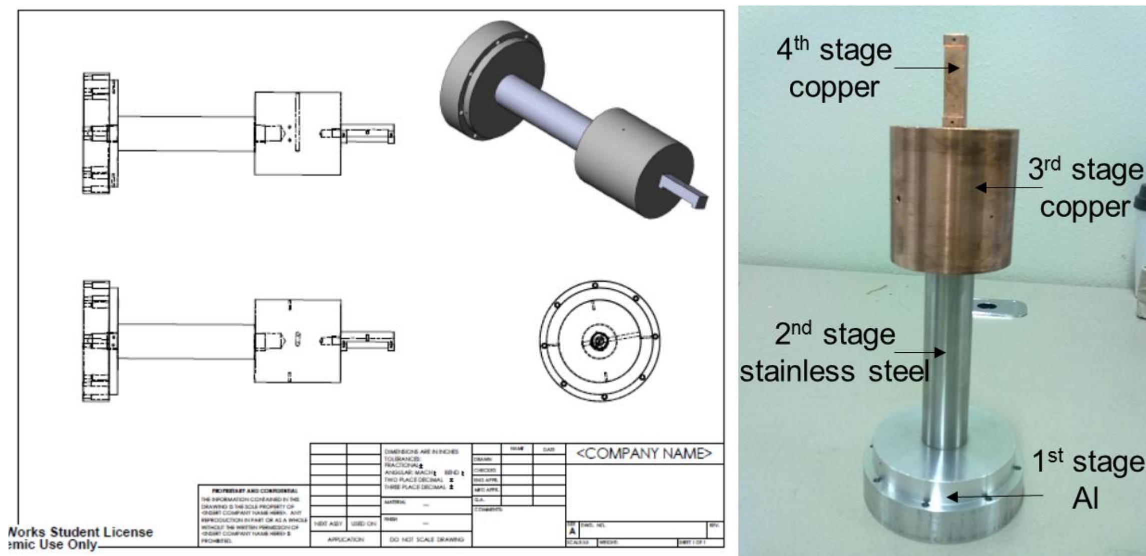

Figure 35. The original design drawing and final product of the cold finger.

Radiation shield

In order to achieve stable environment temperature and better measurement accuracy, the radiation shield was required to reduce the temperature error. In our system, a double-layer stainless steel container was employed to cover the whole chip carrier holder and create good thermal contact with the heating source.

Heating source

In order to reach environment temperature up to 800 K, the selected heater in our system must be able to provide sufficient heating power to warm the system. The temperature controller (Lakeshore 336) can provide up to 100 W of power with 2 A current limit from Output 1 and up to 50 W of power with 1 A current limit from Output 2. Even though the heater outputs are current sources, a compliance voltage 50 V also limited their performance or the maximum power. In our system, a 25 ohm cartridge heater was chose and applied as the heating source with the maximum power of 100 W based on the current and voltage limitations. The cartridge heater was inserted into the bronze cylinder part and then sealed with ceramic compound (Resbond 920), which has high thermal conductivity and electrical resistance and can be used at the temperature up to 1300 ^{o}C.

Cooling source

The cooling cycle system must be able to provide enough cooling power to balance the heating power at different temperatures. In our system, a refrigerated bath/circulator (NESLAB RTE-140) with cooling capacity of 500 W was connected to

the cycling chamber. The enclosed pump delivered cold water at constant temperature of 8 ^{o}C with flow rate of 15 liters/minute through the cycling chamber.

Insulation and connection

The insulation of electrical wires is one major consideration in high temperature system. In fact, wire insulation is one of the major problems preventing the cryostat system for measurement at high temperature. The insulation of wires in low temperature cryostat system is typically polymers, which will not survival at high temperature of 800 K. In order to provide electrical signal or power in the high temperature system, all the electrical wires should be covered by high temperature insulation sleeves. In our system, high temperature fiberglass sleeve (temperature range: -40 ^{o} to 1000 ^{o} F) were applied to provide good insulation to the bare electrical wires.

Due to their low melting temperature (180 ^{o} ~190 ^{o}C), typical solder alloy materials are not suitable in our high temperature system. All the wire connection in the system must be changed to mechanical connection instead of soldering. In our system, surface gold coated connecters were clamped at the end tip of each electrical wires to provide good ohmic contact, meanwhile the other side of connecters can be easily tightly connected to the chip carrier, which provides the sample signals.

Temperature controller

The most advanced and powerful Lakeshore temperature controller model 336 was applied in our high temperature setup to detect the temperature and provide stable temperature. The temperature controller supported temperature sensors, including diode, resistance temperature detectors, and thermocouples. For the best temperature accuracy

in our system, an E-type precision fine wire thermocouple with glass braid insulation was directly attached to the backside of cold finger, which is the closest position to the testing sample. The thermocouple was associated with 100 W heater output which was programmed for closed loop temperature control in proportional – integral – derivative (PID) mode.

Figure 36 shows the structures and details of the high temperature thermal vacuum setup. The whole setup except mechanical pump and bath refrigerator was mounted on top of an optical table to eliminate the vibration.

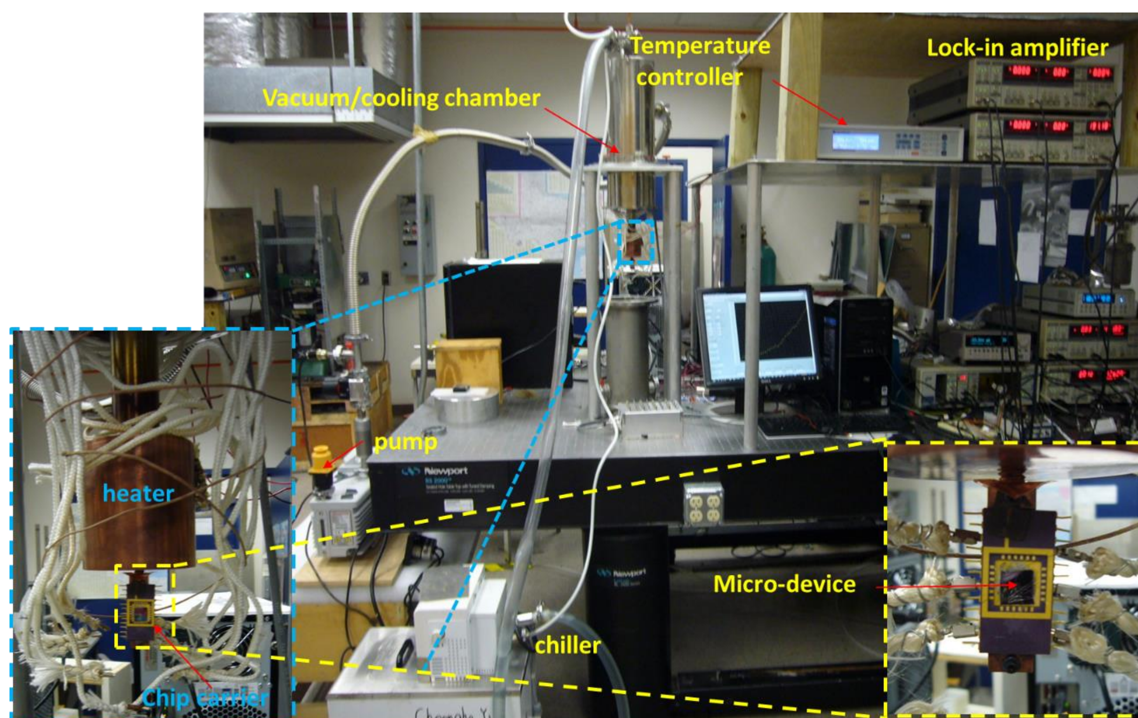

Figure 36. The final assembled high temperature thermal vacuum setup for thermoelectric properties measurement of nanostructured materials.

5.1.2 Temperature controlled by PID algorithm

A stable environment temperature is crucial for the thermoelectric properties measurement at high temperature. The accurate control of temperature was achieved by temperature controller (Lakeshore 336) with PID control algorithm. For closed-loop operation, the control equation for the PID algorithm has three variable terms: proportional (*P*), integral (*I*), and derivative (*D*) and its equation can be expressed as:

$$\text{Heater output} = P\left[e + I\int(e)dt + D\frac{de}{dt}\right] \tag{63}$$

where, *e* is the temperature difference between temperature set point and the feedback reading.

The cartridge heater output was directly connected to the temperature difference between the real temperature and set temperature and the parameters of *P*, *I*, *D*, which provide fine tuning of the control algorithm. At different temperature, the *P*, *I*, *D* may have different value to provide a stable temperature. Figure 37 shows the temperature of the vacuum system as function of time at different set point and different *P*, *I*, *D* parameters. It has been demonstrated that all the temperatures between 450 K and 800 K could be controlled within ±0.05 degrees with a little different PID setting. All the tuning parameters *P*, *I*, and *D* was listed in the Table 7 at different temperatures.

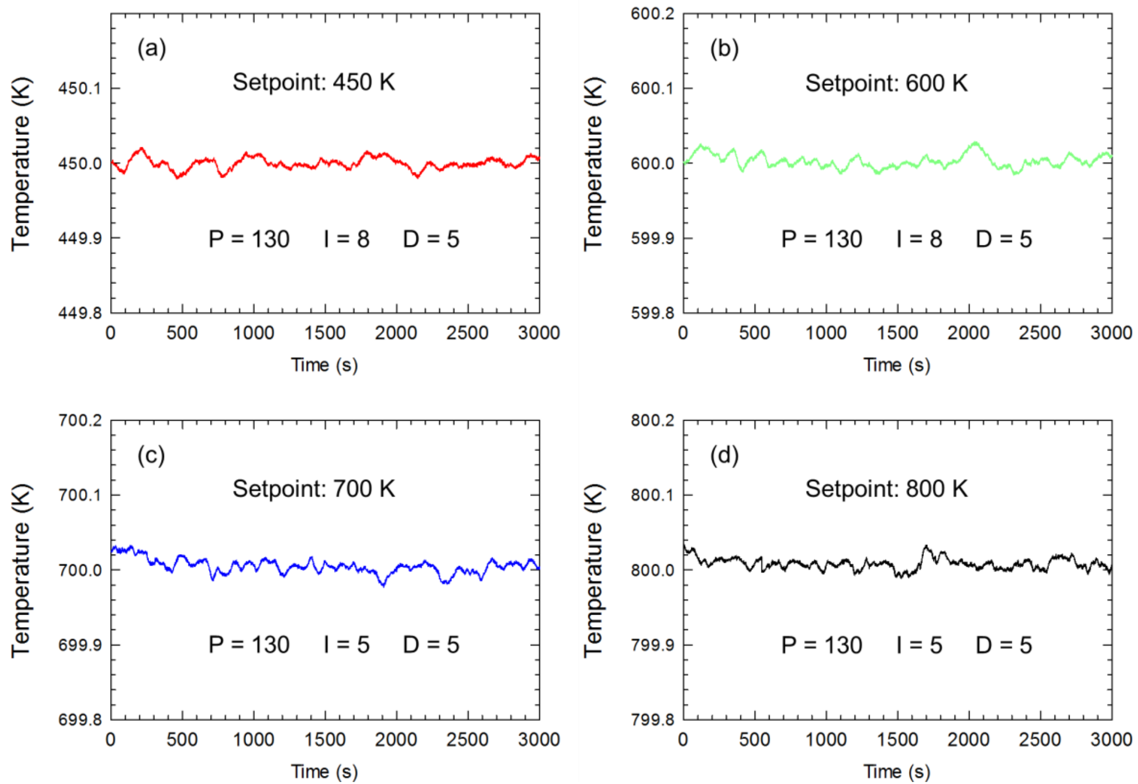

Figure 37. The stability of temperature near the micro-device controlled by PID algorithm at 450 K, 600 K, 700 K and 800 K.

Table 7. The parameters of P, I, and D for temperature controller Lakershore 336 from 300 K to 800 K.

Temperature (K)	P	I	D
300	100	5	5
350	100	5	5
400	130	8	5
450	130	8	5
500	130	8	5
550	130	8	5
600	130	8	5
650	130	8	5
700	130	5	5
750	130	5	5
800	130	5	5

5.2 Sample preparation

The ZnO nanowires measured in high temperature setup are the same samples tested in the low temperature cryostat in chapter 4. Originally, as-synthesized ZnO nanowires are dispersed in 200 proof ethanol (Koptec) by ultra-sonication for a few seconds. Then, the nanowire suspension was dropped on a micro-device for measuring thermal conductivity of the nanowires. After ethanol was dried, nanowires were often bridged between two suspended membranes of the micro-device. In order to improve

thermal contacts between nanowires and platinum electrodes, nanowires were annealed in vacuum chamber at 600 ^oC with ramping rate 2 $^oC/min$. Right after the temperature reached 600 ^oC, the vacuum chamber was naturally cooled down to room temperature. The vacuum pressure was maintained at approximately 10^{-7} torr through a turbo pump in conjunction with a mechanical pump. After the annealing process, the micro-device contains bridged nanowire was attached to chip carrier by using silver paint. Then, the Pt pads of the micro device were wire-bonded to the Au pads on the chip carrier with aluminum wires by wire-bonder (Kulicke & Soffa 4500).

5.3 Thermal conductivity measurement of ZnO nanowires at high temperatures

The new experimental thermal vacuum set-up was able to provide stable environment temperature, making it possible to measure the thermal conductivities of ZnO nanowires at high temperature range. The experimentally measured thermal conductivity of ZnO nanowires with different diameters from 300 K to 800 K are shown in the Figure 38 along with the results of those nanowires measured in the low temperature cryostat from 60 K to 450 K. The thermal conductivity measured by two different setup at the temperature range of 300 K ~ 450 K shows similar values with less than 15% error. The thermal conductivity of ZnO nanowire at high temperature range decrease with decreasing nanowire, which agrees with the previous results of ZnO nanowire study at low temperature range. The strong diameter dependence of thermal conductivity suggests that phonon-boundary scattering is still dominant in thermal transport in ZnO nanowire at high temperature range.

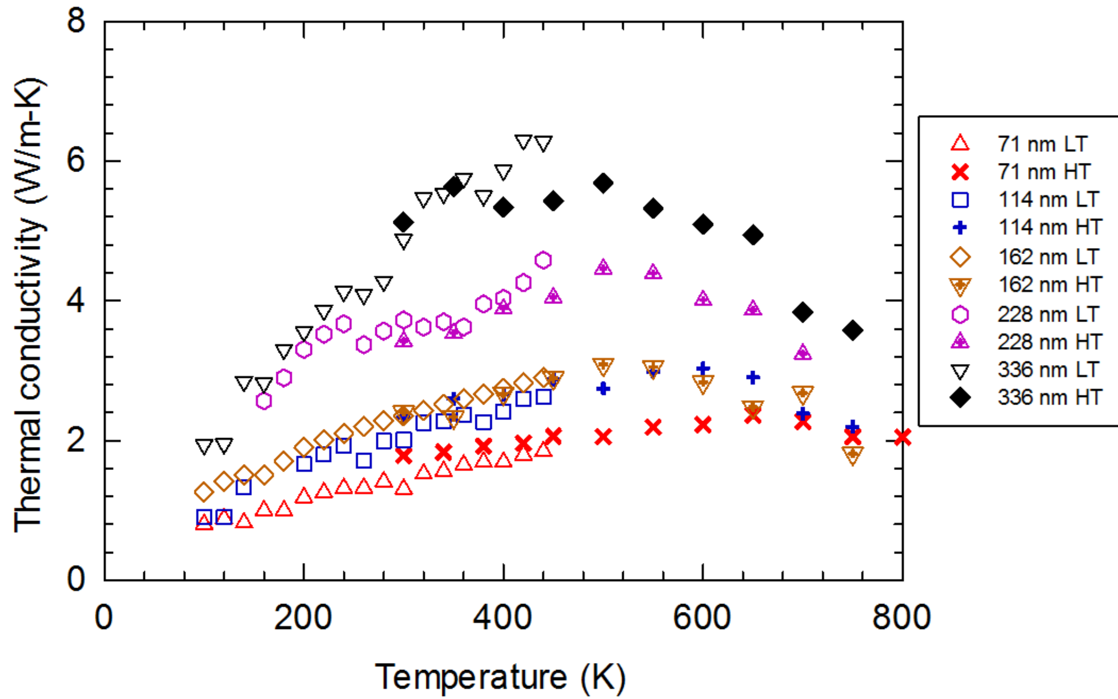

Figure 38. The thermal conductivity of ZnO nanowires with different diameter from 60 K to 800 K. The thermal conductivity data were obtained from two different thermal vacuum system with the temperature range of 60 K ~ 450 K, and 300 K ~ 800 K, respectively.

While the temperature increases to high temperature range, the thermal conductivity of ZnO nanowires first increases and then declines. At the temperature range of 700K ~800 K, all the thermal conductivity rapidly decrease and then converge around 2 W/m-K at 800 K, which is similar with the thermal conductivity of nanostructured ZnO bulk refined by microwave. Considering that the thermal conductivity of 71 nm ZnO nanowire was almost 50% of nanostructured ZnO bulk, the reduction in thermal conductivity at high temperature is not as significant as low temperature. This is because the Umklapp phonon-phonon scattering becomes more

dominant than boundary scattering at high temperature. The thermal conductivity of ZnO nanowires at all temperature range are still much lower than that of ZnO bulk. It was also noticed that the peak of thermal conductivity of ZnO nanowire with smaller diameter is shifted to a much higher temperature than that of ZnO nanowire with larger diameter. The thermal conductivity of ZnO nanowire with diameter of 336 nm has the largest value ~6 W/m-K at the temperature of 500 K, while the peak of thermal conductivity of ZnO nanowire with diameter of 71nm shows up at around 700 K. Both peak temperatures are significantly higher than that of ZnO bulk, which peaks at around 100 K. This shift suggests that the phonon mean free path is limited by boundary scattering as opposed to intrinsic Umklapp scattering at lower temperature, while the Umklapp scattering dominate thermal transport at the high temperature range.

CHAPTER VI

CONCLUSION

This dissertation describes experimental measurements and computational investigations of thermoelectric transport behaviors in one-dimensional nanostructures in a large temperature range. Three one-dimensional nanostructured thermoelectric candidates - SiGe nanowires, $SrTiO_3$ nanowires, and ZnO nanowires – were presented and discussed. A suspended micro-device was used to obtain all three major thermoelectric properties, thermal conductivity, electrical conductivity, and Seebeck coefficient simultaneously. It is crucial to obtain all three properties from the same nanowire since their compositions, crystallinity, and thermoelectric properties might vary considerably even for the samples that are grown at the same time. The measurements were carried out in cryostat system within a temperature range of 60 K ~ 450 K. For minimizing the thermal and electrical resistance at junction of nanowire and platinum contact pad, Focus Ion Beam was employed to deposit a platinum or nickel at the junction.

SiGe were successfully synthesized into nanowire structure along the [111] direction by VLS growth method. The measured thermal conductivity results of SiGe nanowires with different diameter, length, Ge concentration, oxide thickness, and doping concentration were presented. It was found that thermal conductivity of SiGe alloys was significantly decreased when the alloy was formed into nanowires with Si:Ge atomic ratios close to unity. The large reduction in thermal conductivity is from phonon

scattering due to both alloying and surface boundaries. Surface boundary scattering is prominent when the nanowire diameter is ~100 nm or larger, whereas Ge alloying plays a more important role in suppressing the thermal conductivity of smaller diameter samples. The measured values approached to the minimum thermal conductivity by confining and scattering phonon transport within approximately 40-50 nm (diameter) and 40-50 at% Ge in Si (alloying). Since the electronic contribution to the thermal conductivity is negligible, this may suggest they are the smallest achievable thermal conductivity with SiGe. When the nanowire diameter is close to or less than ~60 nm, it is more effective to use a higher Ge concentration to further suppress thermal conductivity rather than use nanowires with smaller diameters.

For P highly doped SiGe nanowires, a large improvement in *ZT* values, experimentally ~0.46 at 450 K, was reported. The *ZT* improvement is attributed to remarkable thermal conductivity reductions, which are thought to derive from the effective scattering of a broad range of phonons by alloying Si with Ge as well as by limiting phonon transport within the nanowire diameters. The additional phonon scattering in alloy nanowires might provide opportunities to use relatively large-diameter nanowires for maintaining the structural integrities required for building practical nanowire-based thermoelectric energy conversion devices in the future.

Thermoelectric properties of phosphorus heavily doped SiGe nanowires were calculated from 300 to 1100 K by using an improved model based on Boltzmann transport equation with relaxation time approximation. All the electron and phonon scatterings were comprehensively discussed and utilized to develop the new model for

estimating electrical conductivity, thermopower, and thermal conductivity of SiGe nanowires. It has been found that non-ionized dopant impurity was non-negligible and has great influences on electron and phonon transport. Moreover, cluster scatterings including Ge cluster and phosphorus cluster could efficiently suppress thermal conductivity of SiGe nanowires. Based on the simulation results of Si nanowires, a new cut off frequency for phonon transport was also applied to adjust the linear overestimation at high frequency. The simulation results based on the new model have excellent agreement with experimental data at low to medium temperature range. At high temperature, an enhanced thermoelectric figure of merit, *ZT* (~1.2) could be achieved for SiGe nanowires, which can be attributed to significant reduction of thermal conductivity. This value can be further increased by using an optimum carrier concentration and removing non-ionized impurities. A maximum projected *ZT* value of $Si_{0.73}Ge_{0.27}$ nanowire at 1100 K was found to be ~2.5 with optimized carrier density 7.8 $\times 10^{19}$ cm^{-3}, which exhibit a strong potential to further improve thermoelectric efficiency of SiGe nanowires. The optimized dopant density results provide opportunities as a guide to synthesize high *ZT* value nanowires in the future.

Strontium titanate nanowire and ZnO nanowire has been successfully synthesized by hydrothermal and thermal annealing method. The thermal conductivity of ZnO nanowires with different diameters were presented. It was observed that their diameters strongly affect the thermal conductivity. The thermal conductivity was measured to be ~2.4 W/m-K at 300K, which is ~17 times smaller than that of bulk ZnO (~40 W/m-K).

A significant increase in thermoelectric efficiency is expected from ZnO nanowires of small diameters.

Moreover, a new vacuum setup was designed and developed to measure the thermal conductivity of ZnO nanowires at high temperature range up to 800 K. The thermal conductivity measured at the temperature range of 300 K ~ 450 K by new setup agrees with previous data with less than 15% error. While the temperature increases to high temperature range, the thermal conductivity of ZnO nanowires first increases and then declines because of the domination of Umklapp phonon-phonon scattering at high temperature. The peak of thermal conductivity of smaller diameter nanowires is shifted to much higher temperature than that of bulk materials. This setup offers great opportunities for investigation of the thermoelectric properties at high temperature and building practical nanowire-based energy harvest devices in the future.

REFERENCES

[1] R. R. Heikes and R. W. Ure, *Thermoelectricity: Science and Engineering* (Interscience, New York, 1961).

[2] F. D. Rosi, Solid State Electron. **11**, 833 (1968).

[3] G. J. Snyder and E. S. Toberer, Nature Mater. **7**, 105 (2008).

[4] A. Majumdar, Science **303**, 777 (2004).

[5] B. Poudel, Science **320**, 634 (2008).

[6] W. Kim and A. Majumdar, J. Appl. Phys. **99**, 084306 (2006).

[7] K. F. Hsu, S. Loo, F. Guo, W. Chen, J. S. Dyck, C. Uher, T. Hogan, E. K. Polychroniadis, and M. G. Kanatzidis, Science **303**, 818 (2004).

[8] R. S. Wagner and W. C. Ellis, Appl. Phys. Lett. **4**, 89 (1964).

[9] J. E. Fischer, H. Dai, A. Thess, R. Lee, N. M. Hanjani, D. L. Dehaas, and R. E. Smalley, Phys. Rev. B **55**, R4921 (1997).

[10] W. Kim, J. Zide, A. Gossard, D. Klenov, S. Stemmer, A. Shakouri, and A. Majumdar, Phys. Rev. Lett. **96**, 045901 (2006).

[11] D. Li, Y. Wu, P. Kim, L. Shi, P. Yang, and A. Majumdar, Appl. Phys. Lett. **83**, 2934 (2003).

[12] A. I. Hochbaum, R. Chen, R. D. Delgado, W. Liang, E. C. Garnett, M. Najarian, A. Majumdar, and P. Yang, Nature **451**, 163 (2008).

[13] G. Joshi, Nano Lett. **8**, 4670 (2008).

[14] X. W. Wang, Appl. Phys. Lett. **93**, 193121 (2008).

[15] K. Tajima, F. Qiu, W. Shin, N. Sawaguchi, N. Izu, K. Tajima, and N. Murayama, Jpn. J. Appl. Phys. **43**, 5978 (2004).

[16] F. Qiu, M. Matsumiya, W. Shin, N. Izu, and N. Murayama, Sensor. Actuat. B-Chem. **94**, 152 (2003).

[17] C. Bajgar, R. Masters, N. Scoville, and J. Vandersande, AIP Conference Proceedings **217**, 440 (1991).

[18] C. Yu, M. L. Scullin, M. Huijben, R. Ramesh, and A. Majumdar, Appl. Phys. Lett. **92**, 191911 (2008).

[19] C. Yu, M. L. Scullin, M. Huijben, R. Ramesh, and A. Majumdar, Appl. Phys. Lett. **92**, 092118 (2008).

[20] M. L. Scullin, C. Yu, M. Huijben, S. Mukerjee, J. Seidel, Q. Zhan, J. Moore, A. Majumdar, and R. Ramesh, Appl. Phys. Lett. **92**, 202113 (2008).

[21] H. Ohta, Nature Mater. **6**, 129 (2007).

[22] A. Ohtomo, D. A. Muller, J. L. Grazul, and H. Y. Hwang, Nature **419**, 378 (2002).

[23] M. Huijben, G. Rijnders, D. H. A. Blank, S. Bals, S. Van Aert, J. Verbeeck, G. Van Tendeloo, A. Brinkman, and H. Hilgenkamp, Nature Mater. **5**, 556 (2006).

[24] S. Thiel, G. Hammerl, A. Schmehl, C. W. Schneider, and J. Mannhart, Science **313**, 1942 (2006).

[25] W. Siemons, G. Koster, H. Yamamoto, W. A. Harrison, G. Lucovsky, T. H. Geballe, D. H. A. Blank, and M. R. Beasley, Phys. Rev. Lett. **98**, 196802 (2007).

[26] A. Brinkman, Nature Mater. **6**, 493 (2007).

[27] A. Kalabukhov, R. Gunnarsson, J. Borjesson, E. Olsson, T. Claeson, and D. Winkler, Phys. Rev. B **75**, 121404 (2007).

[28] G. Herranz, Phys. Rev. Lett. **98**, 216803 (2007).

[29] D. A. Muller, N. Nakagawa, A. Ohtomo, J. L. Grazul, and H. Y. Hwang, Nature **430**, 657 (2004).

[30] Z. Y. Fan and J. G. Lu, J. Nanosci. Nanotechnol. **5**, 1561 (2005).

[31] Z. L. Wang, Mater. Sci. Eng. R-Rep. **64**, 33 (2009).

[32] Y. Q. Chang, Appl. Phys. Lett. **83**, 4020 (2003).

[33] P. Jood, R. J. Mehta, Y. Zhang, G. Peleckis, X. Wang, R. W. Siegel, T. Borca-Tasciuc, S. X. Dou, and G. Ramanath, Nano Lett. **11**, 4337 (2011).

[34] A. Jorio, G. Dresselhaus, and M. S. Dresselhaus, *Carbon Nanotubes: Advanced Topics in the Synthesis, Structure, Properties and Applications* (Springer-Verlag, Berlin, 2008).

[35] C. H. Jin, K. Suenaga, and S. Iijima, Nat. Nanotechnol. **3**, 17 (2008).

[36] W. Park, C. Yu, J. Heat Transf. **134**, 041302 (2012).

[37] D. Nika, A. Cocemasov, D. Crismari, and A. Balandin, Appl. Phys. Lett. **102**, 213109 (2013).

[38] J. Lee, G. Galli, and J. Grossman, Nano Lett. **8**, 3750 (2008).

[39] T. Borca-Tasciuc, A. R. Kumar, and G. Chen, Rev. Sci. Instr. **72**, 2139 (2001).

[40] T. Yamane, N. Nagai, S.-i. Katayama, and M. Todoki, J. Appl. Phys. **91**, 9772 (2002).

[41] J. Park, Y. Ryu, H. Kim, and C. Yu, Nanotechnology **20**, 8 (2009).

[42] C. Yu and J. Park, J. Solid State Chem. **183**, 2268 (2010).

[43] L. Yin and C. Yu, J. Solid State Chem. **187**, 58 (2012).

[44] R. Hull, *Properties of Crystalline Silicon* (INSPEC, The Institution of Electrical Engineers, 1999).

[45] R. Dalven, Infrared Phys. **6**, 129 (1966).

[46] O. V. Mazurin, M. V. Streltsina, and T. P. Shvaiko-Shvaikovskaya, *Handbook of Glass Data: Silica Glass and Binary Silicate Glasses* (Elsevier, Amsterdam, 1983).

[47] D. G. Cahill, S. K. Watson, and R. O. Pohl, Phys. Rev. B **46**, 6131 (1992).

[48] R. Chen, A. I. Hochbaum, P. Murphy, J. Moore, P. Yang, and A. Majumdar, Phys. Rev. Lett. **101**, 105501 (2008).

[49] J. P. Dismukes, L. Ekstrom, E. F. Steigmeier, I. Kudman, and D. S. Beers, J. Appl. Phys. **35**, 2899 (1964).

[50] E. K. Lee, L. Yin, C. Yu, Nano Lett. **12**, 2918 (2012).

[51] C. Guthy, C.Y. Nam, and J. E. Fischer, J. Appl. Phys. **103**, 064319 (2008).

[52] H. Stohr and Z. W. Klemm, Anorg. Allgem. Chem. **241**, 305 (1954).

[53] H. Kim, I. Kim, H. J. Choi, and W. Kim, Appl. Phys. Lett. **96**, 233106 (2010).

[54] G. H. Zhu, Phys. Rev. Lett. **102**, 196803 (2009).

55 Y. Wu, J. Xiang, C. Yang, W. Lu, and C. M. Lieber, Nature **430**, 61 (2004).

56 J. Matinez and B. Swartzentruber, J. Appl. Phys. **110**, 074317 (2011).

57 C. Tien, A. Majumdar, and F. M. Gerner, *Microscale Energy Transport* (Taylor & Francis, Washington DC, 1998).

58 C. Dames and G. Chen, in *Thermoelectrics Handbook: Macro to Nano* edited by D.Rowe (Taylor & Francis Group, Wales, UK, 2005).

59 Z. Wang, Appl. Phys. Lett. **97** 101903 (2010).

60 R. D. Abelson, in *CRC handbook of thermoelectrics*, edited by D. M. Rowe (CRC, Boca Raton, 1995).

61 J. Feser, E. Chan, A. Majumdar, and J. Urban, Nano Lett. **13**, 2122 (2013).

62 L. Shi, Appl. Phys. Lett. **96**, 173108 (2010).

63 C. B. Vining, J. Appl. Phys. **69**, 331 (1991).

64 D. E. Perea, E. R. Hemesath, E. J. Schwalbach, J. L. Lensch-Falk, P. W. Voorhees, and L. J. Lauhon, Nat. Nano **4**, 315 (2009).

65 E. Koren, N. Berkovitch, and Y. Rosenwaks, Nano Lett. **10**, 1163 (2010).

66 R. B. Fair and J. C. C. Tsai, J. Electrochem. Soc. **124**, 1107 (1977).

67 N. Mingo, Phys. Rev. B **68**, 113308 (2003).

68 D. T. Morelli, J. P. Heremans, and G. A. Slack, Phys. Rev. B **66**, 195304 (2002).

69 N. Fukata, S. Ishida, S. Yokono, R. Takiguchi, J. Chen, T. Sekiguchi, and K. Murakami, Nano Lett. **11**, 651 (2011).

70 L. Yin, E. K. Lee, J. W. Lee, D. Whang, B. L. Choi, and C. Yu, Appl. Phys. Lett. **101**, 043114 (2012).

71 C. Yu and K. Choi, ACS Nano **5**, 7885 (2011).

72 C. J. Glassbrenner and G. A. Slack, Phys. Rev. **134**, A1058 (1964).

73 A. J. Minnich, H. Lee, X. W. Wang, G. Joshi, M. S. Dresselhaus, Z. F. Ren, G. Chen, and D. Vashaee, Phys. Rev. B **80**, 155327 (2009).

74 B. V. Zeghbroeck, *Semiconductor Fundamentals* (ECEE, Denver, 2011).

[75] C. B. Vining, Nature Mater. **8**, 83 (2009).

[76] V. I. Fistul', *Heavily doped semiconductors* (Plenum Press, New York, 1969).

[77] S. Krishnamurthy, A. Sher, and A. B. Chen, Phys. Rev. B **33**, 1026 (1986).

[78] H. Jones, Phys. Rev. **81**, 149 (1951).

[79] F. Seitz, Phys. Rev. **73**, 549 (1948).

[80] W. Shockley and J. Bardeen, Phys. Rev. **77**, 407 (1950).

[81] E. Conwell and V. F. Weisskopf, Phys. Rev. **77**, 388 (1950).

[82] H. Brooks, Phys. Rev. **83**, 879 (1951).

[83] D. Chattopadhyay and H. J. Queisser, Rev. Mod. Phys. **53**, 745 (1981).

[84] G. Xiao, J. Lee, J. J. Liou, and A. Ortiz-Conde, Microelectron. Reliab. **39**, 1299 (1999).

[85] G. L. Pearson and J. Bardeen, Phys. Rev. **75**, 865 (1949).

[86] C. Erginsoy, Phys. Rev. **79**, 1013 (1950).

[87] J. Callaway, Phys. Rev. **113**, 1046 (1959).

[88] M. G. Holland, Phys. Rev. **132**, 2461 (1963).

[89] G. A. Slack, *Thermoelectric Materials-New Directions and Approaches* (Materials Research Society, Pittsburgh, 1997).

[90] N. Mingo, L. Yang, D. Li, and A. Majumdar, Nano Lett. **3**, 1713 (2003).

[91] M. Asen-Palmer, Phys. Rev. B **56**, 9431 (1997).

[92] G. A. Slack and S. Galginaitis, Phys. Rev. **133**, A253 (1964).

[93] R. O. Pohl, Phys. Rev. **118**, 1499 (1960).

[94] B. K. Agrawal and G. S. Verma, Phys. Rev. **128**, 603 (1962).

[95] B. Abeles, Phys. Rev. **131**, 1906 (1963).

[96] H. B. G. Casimir, Physica **5**, 495 (1938).

[97] A. Majumdar, J. Heat Transf. **115**, 7 (1993).

[98] J. Randrianalisoa, J. Appl. Phys. **103**, 053502 (2006).

[99] N. Mingo, D. Hauser, N. P. Kobayashi, M. Plissonnier, and A. Shakouri, Nano Lett. **9**, 711 (2009).

[100] J. M. Ziman, Philos. Mag. **1**, 191 (1956).

[101] E. F. Steigmeier and B. Abeles, Phys. Rev. **136**, A1149 (1964).

[102] L. Yin and C. Yu, J. Mater. Sci. **46**, 6385 (2012).

[103] H. Watanabe and S.-i. Takagi, J. Appl. Phys. **90**, 1600 (2001).

[104] Y. Yue and J. J. Liou, Solid State Electron. **39**, 318 (1996).

[105] A. L. Efros, Sov. Phys. Uspekhi **16**, 789 (1974).

[106] L. V. Keldysh and G. P. Proshko, Sov. Phys.-Solid State **5**, 2481 (1964).

[107] E. O. Kane, Solid State Electron. **28**, 3 (1985).

[108] P. P. Altermatt, A. Schenk, and G. Heiser, J. Appl. Phys. **100**, 113714 (2006).

[109] G. A. Thomas, M. Capizzi, F. Derosa, R. N. Bhatt, and T. M. Rice, Phys. Rev. B **23**, 5472 (1981).

[110] D. F. Holcomb and J. J. Rehr, Jr., Phys. Rev. **183**, 773 (1969).

[111] R. Riklund and K. A. Chao, Phys. Rev. B **26**, 2168 (1982).

[112] D. New and T. G. Castner, Phys. Rev. B **29**, 2077 (1984).

[113] D. New, Phys. Rev. B **32**, 2419 (1985).

[114] D. Nobili, A. Armigliato, M. Finnetti, and S. Solmi, J. Appl. Phys. **53**, 1484 (1982).

[115] H. Wang, C. Yu, Polymer **54**, 1136 (2013).

[116] J. Makinen, P. Hautojarvi, and C. Corbel, J. Phys.: Condens. Matter **4**, 5137 (1992).

[117] J. D. Quirt and J. R. Marko, Phys. Rev. B **7**, 3842 (1973).

[118] H. Ue and S. Maekawa, Phys. Rev. B **3**, 4232 (1971).

[119] N. Mikoshiba, Rev. Mod. Phys. **40**, 833 (1968).

[120] J. R. Marko, J. P. Harrison, and J. D. Quirt, Phys. Rev. B **10**, 2448 (1974).

[121] V. Radhakrishnan, P. C. Sharma, and M. Singh, Z. Phys. B **39**, 15 (1980).

[122] R. B. Fair, J. Mater. Res. **1**, 705 (2007).

[123] K. Choi, C. Yu, PLos One, **7**, 44977 (2012).

[124] Y. Ryu, D. Freeman, and C. Yu, Carbon **49**, 4745 (2011).

[125] J. P. Dismukes, J. W. Johnson, and J. M. Millar, Chem. Mater. **9**, 699 (1997).

[126] D. Freeman, C. Yu, PLos One **7**, 47822 (2012).

[127] C. Yu, and Y. Ryu, Energy Env. Sci. **5**, 9481 (2012).

[128] D. M. Rowe, *CRC Handbook of Thermoelectrics* (Taylor & Francis, 1995).

[129] C. Bera, J. Appl. Phys. **108**, 124306 (2010).

[130] Y. Mao, T. J. Park, F. Zhang, H. Zhou, and S. S. Wong, Small **3**, 1122 (2007).

[131] Y. B. Mao, S. Banerjee, and S. S. Wong, J. Am. Chem. Soc. **125**, 15718 (2003).

[132] S. O'Brien, L. Brus, and C. B. Murray, J. Am. Chem. Soc. **123**, 12085 (2001).

[133] J. J. Urban, W. S. Yun, Q. Gu, and H. Park, J. Am. Chem. Soc. **124**, 1186 (2002).

[134] W. D. Yang, J. Electron. Mater. **28**, 986 (1999).

[135] W. Jiang, X. Gong, Z. Chen, Y. Hu, X. Zhang, and X. Gong, Ultrason. Sonochem. **14**, 208 (2007).

[136] Y. Luo, I. Szafraniak, V. Nagarajan, R. B. Wehrspohn, M. Steinhart, J. H. Wendorff, N. D. Zakharov, R. Ramesh, and M. Alexe, Integr. Ferroelectr. **59**, 1513 (2003).

[137] U. A. Joshi and J. S. Lee, Small **1**, 1172 (2005).

[138] M. Paulose, H. E. Prakasam, O. K. Varghese, L. Peng, K. C. Popat, G. K. Mor, T. A. Desai, and C. A. Grimes, J. Phys. Chem. C **111**, 14992 (2007).

[139] H. E. Prakasam, K. Shankar, M. Paulose, O. K. Varghese, and C. A. Grimes, J. Phys. Chem. C **111**, 7235 (2007).

[140] A. I. Boukai, Y. Bunimovich, J. Tahir-Kheli, J. K. Yu, W. A. Goddard, and J. R. Heath, Nature **451**, 168 (2008).

[141] V. Y. Gavrilov, G. A. Zenkovets, and G. N. Kryukova, *Preparation of Catalysts Vii*, (Elsevier, Amsterdam, 1998).

[142] Z. W. Pan, Z. R. Dai, and Z. L. Wang, Science **291**, 1947 (2001).

[143] Z. L. Wang, R. P. Gao, Z. W. Pan, and Z. R. Dai, Adv. Eng. Mater. **3**, 657 (2001).

[144] X. D. Wang, J. H. Song, C. J. Summers, J. H. Ryou, P. Li, R. D. Dupuis, and Z. L. Wang, J. Phys. Chem. B **110**, 7720 (2006).

[145] D. Banerjee, S. H. Jo, and Z. F. Ren, Adv. Mater. **16**, 2028 (2004).

[146] H. W. Kang, J. Phys. Chem. C **115**, 11435 (2011).

[147] H. Srivastava, Semicond. Sci. Tech. **26**, 085030 (2011).

[148] Y. Liu, Z. H. Chen, Z. H. Kang, I. Bello, X. Fan, I. Shafiq, W. J. Zhang, and S. T. Lee, J. Phys. Chem. C **112**, 9214 (2008).

[149] C. Ronning, N. G. Shang, I. Gerhards, H. Hofsass, and M. Seibt, J. Appl. Phys. **98**, 5 (2005).

[150] H. Iwanaga, M. Fujii, and S. Takeuchi, J. Cryst. Growth **134**, 275 (1993).

[151] M. Shiojiri and C. Kaito, J. Cryst. Growth **52**, 173 (1981).

[152] K. Nishio, T. Isshiki, M. Kitano, and M. Shiojiri, Philos. Mag. A-Phys. Condens. Matter Struct. Defect Mech. Prop. **76**, 889 (1997).

[153] http://en.wikipedia.org/wiki/Zinc.

[154] E. Wiberg, N. Wiberg, and A. F. Holleman, *Inorganic chemistry* (Academic Press ; De Gruyter, San Diego; Berlin; New York, 2001).

[155] H. J. Fan, R. Scholz, F. M. Kolb, and M. Zacharias, Appl. Phys. Lett. **85**, 4142 (2004).

[156] Z. L. Wang, J. Phys.-Condes. Matter **16**, R829 (2004).

[157] Y. Ding, Z. L. Wang, T. J. Sun, and J. S. Qiu, Appl. Phys. Lett. **90**, 153510 (2007).

[158] H. Y. Dang, J. Wang, and S. S. Fan, Nanotechnology **14**, 738 (2003).

[159] http://en.wikipedia.org/wiki/Zinc chloride.

[160] P. Erhart and K. Albe, Appl. Phys. Lett. **88**, 201918 (2006).

[161] S. Rackauskas, Nanotechnology **20**, 165603 (2009).

[162] D. A. Voss, E. P. Butler, and T. E. Mitchell, Metall. Trans. A **13**, 929 (1982).